Black holes with electroweak hair: The detailed derivation

Romain Gervalle[1,*] and Mikhail S. Volkov[1,2,†]

[1]*Institut Denis Poisson, UMR-CNRS 7013, Université de Tours, Parc de Grandmont, 37200 Tours, France*
[2]*CERN, Theoretical Physics Department, CH-1211 Geneva 23, Switzerland*

(Received 6 June 2025; accepted 29 July 2025; published 9 September 2025)

We present a very detailed derivation of solutions describing hairy black holes within the gravity-coupled Weinberg-Salam theory, which were previously reported in Gervalle and Volkov [Black holes with electroweak hair, Phys. Rev. Lett. **133**, 171402 (2024)]. These black holes support a strong magnetic field that polarizes the electroweak vacuum and creates a condensate of massive fields carrying superconducting currents along the black hole horizon. The currents, in turn, generate a "corona" of magnetic vortex segments attached to the horizon at both ends. The condensate and corona together constitute the black hole hair. The extremal solutions approach, in the far field, the magnetic Reissner-Nordström configuration, with a total mass that is *lower* than the total charge, $M < |Q|$, due to the negative Zeeman energy of the condensate. This makes the removal of the hair energetically unfavorable. The maximally hairy black holes exhibit masses comparable to terrestrial values, with approximately 11% of their total mass stored in the hair. Given that these solutions arise within a well-tested theoretical framework, they are likely to have physical relevance.

DOI: 10.1103/gzhg-62fz

I. INTRODUCTION

In 1971, Ruffini and Wheeler formulated the no-hair conjecture according to which the only parameters of an isolated black hole should be its mass, angular momentum, and electric/magnetic charge [1]. This conjecture was supported by the uniqueness theorems showing that all *electrovacuum* black holes are described by the Kerr-Newman metrics [2–4] (see Ref. [5] for a review). Besides, the conjecture was confirmed by the no-hair theorems proven for a number of field theory models containing other (scalar, vector, etc.) physical fields [6–13].

The first broadly recognized counterexample to the conjecture was found in 1989 [14]: black holes supporting, outside the horizon, a nontrivial Yang-Mills field not characterized by any charge, hence "a hair" (see Ref. [15] for details). This finding was confirmed [16,17] and then generalized in many ways, leading to a plethora of black holes supporting a Skyrme hair [18,19], a Higgs hair [20,21], various types of stringy hair [22–25], hairy black holes without spherical symmetry [26,27], and many others (see Ref. [28] for a review).

More recent findings include black holes with scalar hair obtained by adjusting the scalar potential [29–31] or by considering nonminimally coupled scalars [32–35]. Besides, there exist interesting solutions describing black holes supporting "spinning clouds" made of ultralight bosons [36–38], "spontaneously scalarized" black holes [39], black holes with a massive graviton hair [40,41], etc.

Nowadays, solutions describing hairy black holes have become so numerous that even a brief review of this subject would be difficult. This naturally raises the question of the relevance of these solutions for describing something that may really exist in nature. Unfortunately, it seems one cannot be too optimistic in this respect. All known solutions describing hairy black holes were obtained either within overly simplified models, or within exotic models relying on the existence of yet undiscovered particles and fields, or within alternative theories of gravity whose applicability remains to be confirmed.

It is not completely excluded that gravitons may have a nonzero mass or that there exists a dilaton field. It is equally possible that the dark matter contains ultralight bosons or that the dark energy can be described by a scalar-tensor theory. However, none of these possibilities have been confirmed yet. Therefore, the physical relevance of solutions describing hairy black holes with massive gravitons, or with a dilaton field, etc., is not immediately obvious. The same can be said about most of the other known solutions.

Some physical relevance may perhaps be attributed to the black holes supporting a pure Yang-Mills field, because the latter arises in QCD. In that case, however, quantum

*Contact author: romain.gervalle@univ-tours.fr
†Contact author: mvolkov@univ-tours.fr

Published by the American Physical Society under the terms of the Creative Commons Attribution 4.0 International license. Further distribution of this work must maintain attribution to the author(s) and the published article's title, journal citation, and DOI. Funded by SCOAP³.

corrections are large and should totally destroy the classical contribution. Therefore, it does not make much sense to describe hairy black holes by classical solutions in this case, although such solutions may probably be used for some effective description [42].

What could be physically relevant solutions describing hairy black holes? To address this question, we explore in this work the coupling between two well-tested physical theories: the Standard Model of fundamental interactions and general relativity. The former contains the QCD sector, where quantum effects are dominant, but in the electroweak sector, the quantum corrections are not too large. Therefore, it makes sense to study extended classical configurations in the Einstein-Weinberg-Salam (EWS) theory. This theory contains the electrovacuum sector with the Kerr-Newman black holes, but does it allow for some other black holes as well?

In fact, allowing for a net magnetic charge, more general black hole solutions do exist in the EWS theory. However, as we shall see, magnetically charged hairy electroweak black holes are in general not spherically symmetric; hence they are difficult to construct. Spherical symmetry is possible in the unphysical limit of the theory when the weak mixing angle vanishes and the U(1) hypercharge field decouples. The corresponding hairy solutions were constructed long ago [21]. For the physical choice of the weak mixing angle, $\sin^2\theta_{\rm W}\approx 0.22$, spherical symmetry is possible only if the black hole magnetic charge is $P=\pm 1/e$, where e is the electron charge. The corresponding solutions were obtained only recently in Ref. [43] (they will be reviewed below), but these black holes are too close to the Planck scale, which again raises the issue of applicability of the classical description. The latter applies if $|P|\gg 1$, but spherical symmetry is then lost.

An important contribution to the analysis of nonspherical black holes was made in Refs. [44,45] by considering perturbations around a magnetically charged Reissner-Nordström (RN) black hole. For simplicity, the analysis was performed not within the full electroweak theory but within its truncated version, not containing the Z and Higgs bosons. However, the remaining field content of the model was sufficient to show that the perturbative black hole hair has a shape similar to a Platonic solid with only discrete symmetries [45]. We were able to carry out a similar analysis within the full electroweak theory and obtained similar results that will be presented below.

A qualitative description of magnetically charged black holes with electroweak hair was given by Maldacena [46]. These black holes become hairy and lose spherical symmetry because of electroweak condensation—a change in the vacuum structure induced by very strong magnetic fields [47–50]. The EWS theory admits the magnetically charged RN solution supporting a Coulombian magnetic field $\mathcal{B}=P/r^2$, with the massive Z, W, and Higgs fields being in the vacuum. If the horizon radius r_h is large, then $|\mathcal{B}(r_h)|=|P|/r_h^2$ is small, and the configuration is stable. If r_h is small and $|\mathcal{B}(r_h)|>m_{\rm W}^2/e$, where $m_{\rm W}$ is the W boson mass, then the configuration no longer minimizes the energy. The latter can be lowered by developing a condensate of the massive fields around the horizon.

The condensate carries superconducting currents, which form loops along the horizon and produce segments of magnetic vortices orthogonal to the horizon. Owing to their mutual repulsion, these vortices are expected to be maximally separated from each other, forming a "corona" around the black hole horizon. This breaks the rotational symmetry.

If $|\mathcal{B}(r_h)|>m_{\rm H}^2/e$, where $m_{\rm H}$ is the Higgs-boson mass, then, in addition to the massive condensate, the horizon should be surrounded by a region where the Higgs field approaches zero, and the full electroweak symmetry is restored. In the far field, all massive fields approach their vacuum values, and the magnetic field becomes spherically symmetric.

Following this scenario, various aspects of magnetic black holes have been discussed, but always at a phenomenological level [51–56]. Explicit solutions describing nonspherically symmetric hairy black holes have not been studied, as this would require 3D numerical simulations—a challenging task. However, our analysis of perturbations of the RN background suggests a simpler option.

Although the absolute minimum of the condensate energy corresponds to a configuration without continuous symmetries, the energy has another critical point describing an axially symmetric state. In this state, the corona degenerates into two oppositely directed multivortices, which is possible for any value of the magnetic charge. The individual vortices within the multivortex configuration repel each other, making the axially symmetric state unstable with respect to spreading into a fully fledged corona. However, this state is a stationary point of the energy and corresponds to an axially symmetric solution of the equations, whose construction requires only 2D simulations.

As we shall see below, the mass of the extremal and near-extremal axially symmetric hairy black holes is *smaller* than their charge. Therefore, they cannot shed their hair and transition into RN black holes, as the mass of the latter exceeds the charge. However, they can further lower their energy when the two multivortices split into elementary vortices, forming a fully spread corona. In this state, they appear to approach an absolute energy minimum and become stable.

Thus, axially symmetric hairy black holes are close to the stable hairy configuration and can evolve toward it when perturbed.

Following the above scenario, we will explicitly construct axially symmetric hairy black holes, and the main steps of our analysis are as follows. After introducing the EWS theory in Sec. II, we describe its simplest solutions,

including the RN and RN-de Sitter black holes, in Sec. III. In Sec. IV, we study linear perturbations around the RN background and identify the threshold values of the event horizon radius at which electroweak condensation begins. The condensate remains spherically symmetric only when the magnetic charge is $P = \pm 1/e$, and in Sec. V, we review the corresponding nonperturbative hairy black hole solutions, originally obtained in Ref. [43]. The structure of the nonspherically symmetric condensate for $|P| > 1/e$ is analyzed in Sec. VI by minimizing the energy of the *nonlinear* perturbations around the RN background.

Restricting to the axially symmetric sector, we present in Sec. VII the ansatz for the gravitational and electroweak fields, along with the essential details: the integral formula for the mass, the removal of the Dirac string singularity, gauge fixing, boundary conditions, the numerical procedure, and the virial relations used to monitor numerical accuracy.

The profiles of the axially symmetric solutions for $P = \pm 2/e$ are illustrated in Sec. VIII, while the general properties of nonextremal axially symmetric hairy black holes are discussed in Sec. IX. Section X is pivotal to our discussion: there, we present the extremal hairy solutions, explain the vortex structure forming the corona, and describe the phase transition when the horizon symmetry changes from spherical to oblate. We also discuss the "weakness of gravity" leading to the relation $M < |Q|$, provide estimates for the mass, radius, and magnetic field of the "maximally hairy" black hole, and include many other important details.

Finally, Sec. XI contains a brief summary of results, a discussion of possible formation mechanisms for hairy electroweak black holes in the early Universe, and potential methods for their detection. Many technical subtleties are addressed in the six Appendixes. Among them, Appendix C, which presents models of electroweak antiscreening, and Appendix F, which discusses electroweak vortices, contain new results that are of interest in their own right, independently of their relevance to the main discussion.

We try to be as explicit as possible and present all the essential aspects of our analysis, aiming at a reader who may not necessarily be an expert both in general relativity and electroweak theory. We explain how to introduce dimensionless variables, define the black hole mass, charge, currents, and quadrupole moments, and handle the constraints. We also describe how to switch to the regular gauge, fix the residual gauge freedom, establish the virial relations, and compute the condensate energy, among other key steps. Although our text is long, we believe it is worth keeping everything in one place rather than splitting it into separate parts, as this would not necessarily improve readability.

A short and highly condensed version of this text can be found in [57]. The results presented below generalize the previous analysis of electroweak monopoles in flat space [58,59], where the electroweak condensate is generated by the magnetic field of a pointlike hypercharge. Electroweak monopoles closely resemble extremal hairy black holes, but their mass is infinite because the energy of the pointlike magnetic charge diverges. Gravity provides a natural cutoff by creating an event horizon, which regularizes the charge's energy and renders the total mass finite.

II. EINSTEIN-WEINBERG-SALAM THEORY

Denoting dimensionful quantities by boldfaced letters and dimensionless ones by ordinary letters, the action of the bosonic part of the standard electroweak theory minimally coupled to the Einstein gravity is

$$\mathcal{S} = \frac{1}{c}\int\left(\frac{c^4}{16\pi G}R + L_{\rm WS}\right)\sqrt{-g}\,d^4x. \tag{2.1}$$

Here, c is the speed of light, G is Newton's constant, and R is the Ricci scalar. The electroweak Lagrangian is

$$L_{\rm WS} = -\frac{1}{4}W^a_{\mu\nu}W^{a\mu\nu} - \frac{1}{4}B_{\mu\nu}B^{\mu\nu} - (D_\mu\Phi)^\dagger D^\mu\Phi - \lambda(\Phi^\dagger\Phi - \Phi_0^2)^2. \tag{2.2}$$

Here, the SU(2) and U(1) field strengths are, respectively,

$$W^a_{\mu\nu} = \partial_\mu W^a_\nu - \partial_\nu W^a_\mu + g\epsilon_{abc}W^b_\mu W^c_\nu, \quad B_{\mu\nu} = \partial_\mu B_\nu - \partial_\nu B_\mu, \tag{2.3}$$

with $\partial_\mu = \partial/\partial x^\mu$. The complex doublet scalar Higgs field and its covariant derivative are

$$\Phi = \begin{pmatrix}\phi_1\\ \phi_2\end{pmatrix}, \qquad D_\mu\Phi = \left(\partial_\mu - \frac{ig'}{2}B_\mu - \frac{ig}{2}\tau_a W^a_\mu\right)\Phi, \tag{2.4}$$

where τ_a are the Pauli matrices. Here, g and g' are the gauge couplings, λ is the Higgs self-coupling, and Φ_0 is the Higgs field vacuum expectation value. Their values are known from experiments [60].

Denoting $g_0 = \sqrt{g^2 + g'^2}$, one can introduce dimensionless quantities:

$$W^a_\mu = \frac{g}{\Phi_0}W^a_\mu, \quad B_\mu = \frac{g'}{\Phi_0}B_\mu, \quad \Phi = \frac{\Phi}{\Phi_0}, \quad \beta = \frac{8\lambda}{g_0^2}, \quad g = \frac{g}{g_0}, \quad g' = \frac{g'}{g_0}, \quad x^\mu = \frac{x^\mu}{l_0}. \tag{2.5}$$

Here, the length scale and the corresponding mass scale are

$$l_0 = \frac{1}{g_0\Phi_0} = 1.53\times 10^{-16}\ \text{cm}, \qquad m_0c^2 = \frac{\hbar c}{l_0} = \hbar c g_0\Phi_0 = 128.9\ \text{GeV}. \tag{2.6}$$

The rescaled gauge couplings are expressed in terms of the Weinberg weak mixing angle:

$$g' \equiv \sin\theta_{\rm W} \approx \sqrt{0.223}, \qquad g \equiv \cos\theta_{\rm W}. \tag{2.7}$$

The rescaled Higgs self-coupling is given by

$$\beta \approx 1.88. \tag{2.8}$$

The absolute value of the electron charge and fine structure constant are

$$\begin{aligned} &\boldsymbol{e} = \hbar\boldsymbol{c}\boldsymbol{g}_0 \times e, \qquad e \equiv gg' = \sin\theta_{\rm W}\cos\theta_{\rm W} \approx 0.416, \\ &\alpha = \frac{\boldsymbol{e}^2}{4\pi\hbar\boldsymbol{c}} = \frac{e^2}{4\pi}\hbar\boldsymbol{c}\boldsymbol{g}_0^2 \approx \frac{1}{137}. \end{aligned} \tag{2.9}$$

Therefore,

$$\frac{1}{\boldsymbol{c}\boldsymbol{g}_0^2} = \frac{e^2}{4\pi\alpha}\hbar = 1.89\hbar, \qquad \frac{1}{\boldsymbol{g}_0} = \frac{\hbar\boldsymbol{c}}{\boldsymbol{e}}e = \frac{e}{4\pi\alpha}\boldsymbol{e}. \tag{2.10}$$

The relation to the Planck mass $\mathbf{M}_{\rm Pl}$ and Planck length $\mathbf{L}_{\rm Pl}$ is

$$\begin{aligned} &\boldsymbol{m}_0 = \sqrt{\frac{\alpha\kappa}{2e^2}}\mathbf{M}_{\rm Pl} = 1.05\times 10^{-17}\times \mathbf{M}_{\rm Pl}, \\ &\boldsymbol{l}_0 = \sqrt{\frac{2e^2}{\alpha\kappa}}\mathbf{L}_{\rm Pl} = 9.46\times 10^{16}\times \mathbf{L}_{\rm Pl}. \end{aligned} \tag{2.11}$$

One defines the dimensionless gravitational coupling,

$$\kappa = \frac{8\pi\mathbf{G}\boldsymbol{\Phi}_0^2}{\boldsymbol{c}^4} = \frac{4e^2}{\alpha}\left(\frac{\boldsymbol{m}_{\rm Z}}{\mathbf{M}_{\rm Pl}}\right)^2 = 5.30\times 10^{-33}, \tag{2.12}$$

where $\boldsymbol{m}_{\rm Z}$ is the Z boson mass.

Substituting everything into (2.1), the action becomes $\boldsymbol{\mathcal{S}} = \hbar\times\mathcal{S}$ with

$$\begin{aligned} \mathcal{S} &= \frac{e^2}{4\pi\alpha}\int\left(\frac{1}{2\kappa}R + \mathcal{L}_{\rm WS}\right)\sqrt{-\mathrm{g}}d^4x, \\ \mathcal{L}_{\rm WS} &= -\frac{1}{4g^2}\mathrm{W}^a_{\mu\nu}\mathrm{W}^{a\mu\nu} - \frac{1}{4g'^2}B_{\mu\nu}B^{\mu\nu} \\ &\quad - (D_\mu\Phi)^\dagger D^\mu\Phi - \frac{\beta}{8}(\Phi^\dagger\Phi - 1)^2, \end{aligned} \tag{2.13}$$

where $B_{\mu\nu} = \partial_\mu B_\nu - \partial_\nu B_\mu$ and

$$\begin{aligned} \mathrm{W}^a_{\mu\nu} &= \partial_\mu \mathrm{W}^a_\nu - \partial_\nu \mathrm{W}^a_\mu + \epsilon_{abc}\mathrm{W}^b_\mu\mathrm{W}^c_\nu, \\ D_\mu\Phi &= \left(\partial_\mu - \frac{i}{2}B_\mu - \frac{i}{2}\tau_a\mathrm{W}^a_\mu\right)\Phi. \end{aligned} \tag{2.14}$$

This is the theory of the interacting gravitational field $\mathrm{g}_{\mu\nu}$, the complex valued Higgs field $\Phi = (\phi_1, \phi_2)^{\rm T}$, the U(1) hypercharge field $B = B_\mu dx^\mu$, and the SU(2) field $\mathrm{W} = \mathrm{T}_a\mathrm{W}^a_\mu dx^\mu$, where $\mathrm{T}_a = \tau_a/2$ are the SU(2) generators.

The action (2.13) is invariant under spacetime diffeomorphisms and also under $\mathrm{SU}(2)\times\mathrm{U}(1)$ gauge transformations,

$$\Phi \to \mathfrak{V}\Phi, \qquad \mathcal{V} \to \mathfrak{V}\mathcal{V}\mathfrak{V}^{-1} + 2i\mathfrak{V}\partial_\mu\mathfrak{V}^{-1}dx^\mu, \tag{2.15}$$

where

$$\mathcal{V} = (B_\mu + \tau_a\mathrm{W}^a_\mu)dx^\mu, \quad \mathfrak{V} = \exp\left(\frac{i}{2}\upsilon + \frac{i}{2}\theta^a\tau_a\right), \tag{2.16}$$

with υ and θ^a being functions of x^μ.

A. Field equations

Varying the action (2.13) with respect to B_μ, W^a_μ, and Φ yields the electroweak (EW) equations:

$$\begin{aligned} &\nabla^\mu B_{\mu\nu} = g'^2\frac{i}{2}(\Phi^\dagger D_\nu\Phi - (D_\nu\Phi)^\dagger\Phi), \\ &\mathcal{D}^\mu\mathrm{W}^a_{\mu\nu} = g^2\frac{i}{2}(\Phi^\dagger\tau^a D_\nu\Phi - (D_\nu\Phi)^\dagger\tau^a\Phi), \\ &D_\mu D^\mu\Phi - \frac{\beta}{4}(\Phi^\dagger\Phi - 1)\Phi = 0, \end{aligned} \tag{2.17}$$

where

$$\mathcal{D}_\mu\mathrm{W}^a_{\alpha\beta} = \nabla_\mu\mathrm{W}^a_{\alpha\beta} + \epsilon_{abc}\mathrm{W}^b_\mu\mathrm{W}^c_{\alpha\beta}, \tag{2.18}$$

with ∇_μ being the geometrical covariant derivative with respect to the spacetime metric $\mathrm{g}_{\mu\nu}$. Varying the action with respect to the latter yields the Einstein equations:

$$G_{\mu\nu} = \kappa T_{\mu\nu}, \tag{2.19}$$

where $G_{\mu\nu} = R_{\mu\nu} - (R/2)\mathrm{g}_{\mu\nu}$ is the Einstein tensor, and the energy-momentum tensor is given by

$$\begin{aligned} T_{\mu\nu} &= \frac{1}{g^2}\mathrm{W}^a{}_{\mu\sigma}\mathrm{W}^a{}_\nu{}^\sigma + \frac{1}{g'^2}B_{\mu\sigma}B_\nu{}^\sigma + (D_\mu\Phi)^\dagger D_\nu\Phi \\ &\quad + (D_\nu\Phi)^\dagger D_\mu\Phi + \mathrm{g}_{\mu\nu}\mathcal{L}_{\rm WS}. \end{aligned} \tag{2.20}$$

The vacuum is defined as the configuration with $T_{\mu\nu} = 0$. Modulo gauge transformations, it can be chosen as

$$\mathrm{W}^a_\mu = B_\mu = 0, \qquad \Phi = \begin{pmatrix} 0 \\ 1 \end{pmatrix}, \qquad \mathrm{g}_{\mu\nu} = \eta_{\mu\nu}, \tag{2.21}$$

where $\eta_{\mu\nu} = \mathrm{diag}[-1, 1, 1, 1]$ is the Minkowski metric.

Allowing for small fluctuations around the vacuum and linearizing the field equations with respect to these fluctuations yield the perturbative mass spectrum of the theory. The spectrum includes the massless photon and graviton, as

well as the massive Z, W, and Higgs bosons with masses

$$m_{\rm Z} = \frac{1}{\sqrt{2}}, \qquad m_{\rm W} = g m_{\rm Z}, \qquad m_{\rm H} = \sqrt{\beta} m_{\rm Z}, \quad (2.22)$$

in units of the mass scale $\boldsymbol{m}_0$.

B. Arnowitt-Deser-Misner (ADM) mass

We shall solve the field equations to obtain asymptotically flat solutions with a finite ADM mass. The metric $g_{\mu\nu}$ then approaches the Minkowski metric $\eta_{\mu\nu}$ at spatial infinity. Introducing the Schwarzschild radial coordinate r, the mass is determined from the asymptotic form of the g_{00} metric coefficient as $r \to \infty$,

$$-g_{00} = 1 - \frac{2M}{r} + \ldots = 1 - \frac{2\mathbf{G}\boldsymbol{M}}{\boldsymbol{c}^2 \boldsymbol{r}} + \ldots, \quad (2.23)$$

where $\boldsymbol{r} = \boldsymbol{l}_0 r$, and the dots denote subleading terms. Therefore,

$$\frac{\mathbf{M}}{\boldsymbol{m}_0} = \frac{\boldsymbol{c}^2 \boldsymbol{l}_0}{\mathbf{G}\boldsymbol{m}_0} M = \frac{8\pi}{\kappa} \times \frac{M}{\hbar \boldsymbol{c} \boldsymbol{g}_0^2} = \frac{e^2}{4\pi\alpha} \times \mathcal{M} \approx 1.89 \mathcal{M}, \quad (2.24)$$

where we have used (2.10), and where the rescaled dimensionless mass is

$$\mathcal{M} = \frac{8\pi}{\kappa} M. \quad (2.25)$$

C. Electromagnetic and Z fields, currents, and magnetic charge

There is no unique way to define electromagnetic and Z fields away from the Higgs vacuum, but two special definitions are often considered in the literature.

1. Nambu definition

According to Nambu, the electromagnetic and Z fields can be defined as [61]

$$\mathcal{F}_{\mu\nu} = \frac{g}{g'} B_{\mu\nu} - \frac{g'}{g} n^a \mathrm{W}^a_{\mu\nu}, \quad \mathcal{Z}_{\mu\nu} = B_{\mu\nu} + n^a \mathrm{W}^a_{\mu\nu}, \quad (2.26)$$

where

$$n^a = \frac{(\Phi^\dagger \tau^a \Phi)}{(\Phi^\dagger \Phi)}, \qquad n^a n^a = 1. \quad (2.27)$$

The Higgs vacuum can be defined as a state where, modulo gauge transformations, one has

$$\mathrm{W}^1_\mu = \mathrm{W}^2_\mu = 0, \qquad \Phi = \begin{pmatrix} 0 \\ 1 \end{pmatrix}. \quad (2.28)$$

This choice is compatible with the equations for W^1_μ, W^2_μ, and Φ contained in Eq. (2.17). The field strengths in this state can be represented as

$$\mathcal{F}_{\mu\nu} = \partial_\mu \mathcal{A}_\nu - \partial_\nu \mathcal{A}_\mu, \qquad \mathcal{Z}_{\mu\nu} = \partial_\mu \mathcal{Z}_\nu - \partial_\nu \mathcal{Z}_\mu, \quad (2.29)$$

where the potentials are given by

$$\mathcal{A}_\mu = \frac{g}{g'} B_\mu + \frac{g'}{g} \mathrm{W}^3_\mu, \qquad \mathcal{Z}_\mu = B_\mu - \mathrm{W}^3_\mu. \quad (2.30)$$

The remaining nontrivial field equations in (2.17) then reduce to

$$\nabla^\mu \mathcal{F}_{\nu\mu} = 0, \qquad \nabla^\mu \mathcal{Z}_{\nu\mu} + m_{\rm Z}^2 \mathcal{Z}_\nu = 0. \quad (2.31)$$

Therefore, $\mathcal{F}_{\mu\nu}$ satisfies the source-free Maxwell equations. The two forms

$$\mathcal{F} = \frac{1}{2} \mathcal{F}_{\mu\nu} dx^\mu \wedge dx^\nu, \qquad \mathcal{Z} = \frac{1}{2} \mathcal{Z}_{\mu\nu} dx^\mu \wedge dx^\nu \quad (2.32)$$

are closed in the Higgs vacuum, satisfying

$$d\mathcal{F} = 0, \qquad d\mathcal{Z} = 0. \quad (2.33)$$

Away from the Higgs vacuum, however, the form $\mathcal{F}$ is not necessarily closed, i.e., $d\mathcal{F} \neq 0$ (similarly for $\mathcal{Z}$), since there is no fundamental reason for the Maxwell equations to hold in this regime. This is actually useful for our purposes, as it allows us to introduce a smooth magnetic charge density.

2. 't Hooft definition

The electromagnetic and Z fields can be defined as closed forms even away from the Higgs vacuum by using the prescription of 't Hooft [62]. The key observation is the identity

$$n^a \mathrm{W}^a_{\mu\nu} + g^2 \psi_{\mu\nu} = \partial_\mu \mathcal{W}_\nu - \partial_\nu \mathcal{W}_\mu, \quad (2.34)$$

where

$$g^2 \psi_{\mu\nu} = -\epsilon_{abc} n^a \mathcal{D}_\mu n^b \mathcal{D}_\nu n^c,$$
$$\mathcal{W}_\mu = n^a W^a_\mu + i \frac{(\Phi^\dagger \partial_\mu \Phi - \partial_\mu \Phi^\dagger \Phi)}{(\Phi^\dagger \Phi)}, \quad (2.35)$$

with $\mathcal{D}_\mu n^a \equiv \partial_\mu n^a + \epsilon_{abc} \mathrm{W}^b_\mu n^c$. It is worth noting that the Φ contribution to $\mathcal{W}_\mu$ vanishes if Φ is real valued. The tensor $\psi_{\mu\nu}$ is gauge invariant, while $\mathcal{W}_\mu$ changes under generic gauge transformations (2.15) and (2.16) as

$$\mathcal{W}_\mu \to \mathcal{W}_\mu - \partial_\mu \upsilon, \quad (2.36)$$

so that it is affected only by the U(1) part of the transformation and remains invariant under the SU(2) transformations.

This allows one to introduce the closed two forms,

$$F_{\mu\nu} = \mathcal{F}_{\mu\nu} - e\psi_{\mu\nu} = \partial_\mu A_\nu - \partial_\nu A_\mu,$$
$$Z_{\mu\nu} = \mathcal{Z}_{\mu\nu} + g^2\psi_{\mu\nu} = \partial_\mu Z_\nu - \partial_\nu Z_\mu, \tag{2.37}$$

where the corresponding potentials are given by

$$A_\mu = \frac{g}{g'}B_\mu - \frac{g'}{g}\mathcal{W}_\mu, \qquad Z_\mu = B_\mu + \mathcal{W}_\mu. \tag{2.38}$$

The effect of the gauge transformations (2.15) and (2.16) is

$$A_\mu \to A_\mu + \frac{1}{e}\partial_\mu \upsilon, \qquad Z_\mu \to Z_\mu. \tag{2.39}$$

In the unitary gauge, where $\Phi = (0, \phi)^{\mathrm{T}}$ with real valued ϕ, one has $n^a = -\delta^a_3$ and $\mathcal{W}_\mu = n^a W^a_\mu$, therefore,

$$g^2\psi_{\mu\nu} = \mathrm{W}^1_\mu \mathrm{W}^2_\nu - \mathrm{W}^1_\nu \mathrm{W}^2_\mu,$$
$$A_\mu = \frac{g}{g'}B_\mu + \frac{g'}{g}\mathrm{W}^3_\mu, \qquad Z_\mu = B_\mu - \mathrm{W}^3_\mu. \tag{2.40}$$

This equation is often used in the literature as the definition of the field potentials. However, the unitary gauge is not always suitable when the Higgs field approaches zero. For this reason, it is preferable to use the more general definition (2.38), which does not require imposing the unitary gauge.

Since $\psi_{\mu\nu}$ in (2.40) is constructed from the massive W field, it vanishes exponentially fast in the far field zone. Consequently, both $\mathcal{F}_{\mu\nu}$ and $F_{\mu\nu}$ reduce to the same Maxwell tensor at large distances. This implies that the global quantities expressed as surface integrals at spatial infinity remain identical in both the Nambu and 't Hooft descriptions. However, at short distances, the two frameworks provide different interpretations, which, in a certain sense, are dual to each other.

3. Current densities and magnetic fields

The approach of 't Hooft is more commonly used in the literature since A_μ and Z_μ can serve as fundamental variables, allowing the entire set of electroweak equations to be formulated in terms of these fields [see Eq. (6.8) below]. The same is not possible with the Nambu fields as they do not admit potentials, making 't Hooft's formulation more fundamental in this regard.

However, a key advantage of the Nambu approach is that the two form $\mathcal{F}_{\mu\nu}$ is not closed and allows for the definition of a smooth magnetic charge density, which can sometimes offer valuable insights. In 't Hooft's approach, the magnetic charge is always pointlike; nevertheless, we shall see that it can effectively "mimic" a smooth charge distribution.

Therefore, in what follows, we will consider both $\mathcal{F}_{\mu\nu}$ and $F_{\mu\nu}$, along with their associated currents,

$$4\pi\mathcal{J}^\mu = \frac{1}{\sqrt{-\mathrm{g}}}\partial_\nu(\sqrt{-\mathrm{g}}\mathcal{F}^{\mu\nu}), \quad 4\pi J^\mu = \frac{1}{\sqrt{-\mathrm{g}}}\partial_\nu(\sqrt{-\mathrm{g}}F^{\mu\nu}). \tag{2.41}$$

The rescaled $(-g/g')J^\mu$ is sometimes referred to as neutral current because it sources the Z field [see Eq. (6.8b)]. Introducing the dual tensors,

$$\tilde{\mathcal{F}}^{\mu\nu} = \frac{1}{2\sqrt{-\mathrm{g}}}\epsilon^{\mu\nu\alpha\beta}\mathcal{F}_{\alpha\beta}, \quad \tilde{F}^{\mu\nu} = \frac{1}{2\sqrt{-\mathrm{g}}}\epsilon^{\mu\nu\alpha\beta}F_{\alpha\beta}, \tag{2.42}$$

the Nambu definition allows us to define the magnetic current,

$$4\pi\tilde{\mathcal{J}}^\mu = \frac{1}{\sqrt{-\mathrm{g}}}\partial_\nu(\sqrt{-\mathrm{g}}\tilde{\mathcal{F}}^{\mu\nu}), \tag{2.43}$$

which can be nontrivial. In contrast, within the 't Hooft definition, the corresponding magnetic current is locally zero.

We will focus on static and purely magnetic systems. Denoting $\mathcal{N} = \sqrt{|\mathrm{g}_{00}|}$ and $\mathrm{h} = \sqrt{\det(\mathrm{g}_{ik})}$, the magnetic field is defined as

$$\mathcal{B}^i = \tilde{\mathcal{F}}^{0i} = \frac{1}{\mathcal{N}}\frac{1}{2\mathrm{h}}\epsilon^{ijk}\mathcal{F}_{jk}$$
$$\Rightarrow \mathcal{B}_i = \frac{1}{\mathcal{N}}\frac{\mathrm{h}}{2}\epsilon_{ijk}\mathcal{F}^{jk} \Rightarrow \mathcal{F}^{ik} = \frac{\mathcal{N}}{\mathrm{h}}\epsilon^{ikm}\mathcal{B}_m. \tag{2.44}$$

The magnetic field in the 't Hooft definition will be also denoted by $\mathcal{B}^i = \tilde{F}^{0i}$, with no ambiguity, as it will always be clear from the context which definition is being used. Similarly, we define the massive magnetic fields,

$$\mathcal{B}^i_Z = \tilde{Z}^{0i}, \qquad \mathcal{B}^i_{\mathcal{Z}} = \tilde{\mathcal{Z}}^{0i}, \tag{2.45}$$

but we introduce a different symbol for the hypermagnetic field:

$$\mathrm{B}^i = \tilde{B}^{0i}. \tag{2.46}$$

4. Integrated currents

Injecting (2.44) into (2.41) yields the following relations:

$$4\pi\sqrt{-\mathrm{g}}\mathcal{J}^i = \epsilon^{ikm}\partial_k(\mathcal{N}^2\mathcal{B}_m)$$
$$\Rightarrow 4\pi\sqrt{-\mathrm{g}}\epsilon_{kmi}\mathcal{J}^i = \partial_k(\mathcal{N}^2\mathcal{B}_m) - \partial_m(\mathcal{N}^2\mathcal{B}_k). \tag{2.47}$$

Hence, introducing one forms $\mathcal{B} = \mathcal{B}_k dx^k$ and $\mathcal{J} = \mathcal{J}_k dx^k$, we obtain

$$4\pi\mathcal{N} * \mathcal{J} = d(\mathcal{N}^2\mathcal{B}) = d(\mathcal{N} * \mathcal{F}), \tag{2.48}$$

where the star $*$ denotes the Hodge duality operator on the spacelike three surface. Both sides of these relations are two forms. Integrating over a two surface Σ and applying Green's theorem yield the total current through Σ,

$$\begin{aligned} 4\pi\mathcal{I} &\equiv 4\pi\int_\Sigma \mathcal{N} * \mathcal{J} = \oint_{\partial\Sigma} \mathcal{N}^2\mathcal{B}_m dx^m \\ &= \frac{1}{2}\oint_{\partial\Sigma} \sqrt{-\mathrm{g}}\mathcal{F}^{ik}\epsilon_{ikm}dx^m. \end{aligned} \tag{2.49}$$

This is Ampère's law relating the electric current to the circulation of the magnetic field. Replacing everywhere $\mathcal{F}_{ik} \to F_{ik}$ yields similarly the 't Hooft current I. The dimensionful currents expressed in amperes are

$$\boldsymbol{\mathcal{I}} = \boldsymbol{c\Phi}_0\mathcal{I} = \frac{e}{4\pi\alpha}\frac{\boldsymbol{e}}{\boldsymbol{t}_0}\mathcal{I} = \mathcal{I}\times 1.42\times 10^8\ \mathrm{A}, \quad \boldsymbol{I} = \boldsymbol{c\Phi}_0 I, \tag{2.50}$$

where $\boldsymbol{t}_0 = \boldsymbol{l}_0/\boldsymbol{c} = 5.1\times 10^{-27}$ sec.

5. Magnetic charge

The magnetic charge density in the Nambu definition is given by

$$4\pi\tilde{\mathcal{J}}^0 = \frac{1}{\sqrt{-\mathrm{g}}}\partial_\nu(\sqrt{-\mathrm{g}}\tilde{\mathcal{F}}^{0\nu}) = \nabla_k\mathcal{B}^k = \frac{e}{2}\frac{1}{\sqrt{-\mathrm{g}}}\epsilon^{ijk}\partial_i\psi_{jk}, \tag{2.51}$$

whereas in the 't Hooft definition, it is locally zero. However, the total magnetic charge, defined via the flux through a closed two surface at spatial infinity, is the same in both descriptions:

$$P = \frac{1}{4\pi}\oint_{\partial\mathbb{R}^3}\mathcal{F} = \frac{1}{4\pi}\oint_{\partial\mathbb{R}^3} F, \tag{2.52}$$

because at infinity one has $\mathcal{F} = F$.

Since F is closed, the second integral in (2.52) is determined solely by the topology of F and remains unchanged as the integration surface shrinks. Consequently, within the 't Hooft definition, the magnetic charge is always pointlike, akin to the Dirac monopole. Its density can only have a distributional support, in which case one can introduce a potential such that, locally, $F = dA$.

At the same time, since we are working within the non-Abelian theory, it is meaningful to consider a scenario where the magnetic charge is smoothly distributed in space, as described by the density in Eq. (2.51). To achieve this, we use the Nambu field $\mathcal{F}$, which lacks potential but allows for a well-defined magnetic charge within a finite volume V:

$$P(V) = \frac{1}{4\pi}\oint_{\partial V}\mathcal{F} = \frac{1}{4\pi}\oint_{\partial V}(F + e\psi) = P + \frac{e}{4\pi}\oint_{\partial V}\psi. \tag{2.53}$$

Since ψ is exponentially suppressed at infinity, its flux vanishes in the asymptotic limit, ensuring that $P(V)$ approaches P as $V \to \infty$.

III. ABELIAN SOLUTIONS

We begin our analysis with the simplest case: spherically symmetric solutions. The assumption of spherical symmetry is quite restrictive, allowing either solutions with known metrics or, for a specific value of the magnetic charge $|P| = 1/e$, simple hairy solutions. However, it is natural to start with the simplest cases. Moreover, studying perturbations around the Reissner-Nordström background provides valuable insight into more general solutions. For these reasons, we shall focus on the spherically symmetric sector for now.

The static and spherically symmetric metric can be parametrized as

$$ds^2 = -\sigma^2(r)N(r)dt^2 + \frac{dr^2}{N(r)} + r^2(d\vartheta^2 + \sin^2\vartheta d\varphi^2). \tag{3.1}$$

The static, spherically symmetric, and purely magnetic electroweak fields can be expressed as [see Ref. [58] for details]

$$\begin{aligned} \mathrm{W} &= f(r)[\mathrm{T}_2 d\vartheta - \nu T_1\sin\vartheta d\varphi] + \mathrm{T}_3\nu\cos\vartheta d\varphi, \\ B &= \nu\cos\vartheta d\varphi, \qquad \Phi = \begin{pmatrix} 0 \\ \phi(r) \end{pmatrix}. \end{aligned} \tag{3.2}$$

The gauge fields exhibit a Dirac string singularity at $\vartheta = 0, \pi$ due to their nonvanishing azimuthal components. However, as will be explicitly shown below in the more general axially symmetric case, this singularity can be gauged away if the constant ν is given by

$$\nu = -\frac{n}{2}, \qquad n \in \mathbb{Z}. \tag{3.3}$$

Substituting (3.1) and (3.2) into the Einstein-Weinberg-Salam equations (2.17) and (2.19), the angular variables separate, yielding the following system of ordinary differential equations:

$$(N\sigma f')' = \sigma\left(\frac{f^2-1}{r^2} + \frac{g^2}{2}\phi^2\right)f, \tag{3.4a}$$

$$(r^2N\sigma\phi')' = \sigma\left(\frac{\beta r^2}{4}(\phi^2-1) + \frac{1}{2}f^2\right)\phi, \tag{3.4b}$$

$$m' = \frac{\kappa}{2}\left(N\mathcal{U}_1 + \mathcal{U}_0 + \frac{\nu^2}{2g^2r^2}\right) \equiv \frac{\kappa}{2} r^2 T_{\hat{0}\hat{0}}, \tag{3.4c}$$

$$\frac{\sigma'}{\sigma} = \frac{\kappa}{r}\mathcal{U}_1, \tag{3.4d}$$

$$(\nu^2-1)f' = (\nu^2-1)f\phi = 0, \tag{3.4e}$$

where

$$\mathcal{U}_1 = \frac{1}{g^2}f'^2 + r^2\phi'^2,$$
$$\mathcal{U}_0 = \nu^2\frac{(f^2-1)^2}{2g^2r^2} + \frac{1}{2}f^2\phi^2 + \frac{\beta r^2}{8}(\phi^2-1)^2. \tag{3.5}$$

We have introduced the mass function $m(r)$, with $N(r) = 1–2m(r)/r$, and denote $T_{\hat{0}\hat{0}} = -T^0{}_0$ the projection of $T_{\mu\nu}$ onto the timelike vector of the orthonormal tetrad.

These equations admit simple analytical solutions describing *Abelian* configurations, for which the nonlinear part of the SU(2) field strength vanishes.

A. Reissner-Nordström solution

The simplest solution to Eq. (3.4) is given by

$$f = 0, \quad \phi = 1, \quad \sigma = 1, \quad N(r) = 1 - \frac{2M}{r} + \frac{Q^2}{r^2}$$
$$\text{with} \quad Q^2 = \frac{\kappa}{2}P^2, \quad P = \frac{n}{2e}, \tag{3.6}$$

where M is an integration constant. This describes the magnetic RN black hole,

$$ds^2 = -N(r)dt^2 + \frac{dr^2}{N(r)} + r^2(d\vartheta^2 + \sin^2\vartheta d\varphi^2),$$
$$B = -(n/2)\cos\vartheta d\varphi, \quad \mathrm{W} = \mathrm{T}_3 B, \quad \Phi = \begin{pmatrix}0\\1\end{pmatrix}. \tag{3.7}$$

The event horizon is located at $r_h = M + \sqrt{M^2 - Q^2}$. The gauge fields exhibit a Dirac string singularity at $\vartheta = 0, \pi$, which can be removed by gauge transformations (2.15) with

$$\mathfrak{V}_\pm = \exp\left(\pm i\nu\varphi(1+\tau_3)/2\right), \tag{3.8}$$

whose effect is

$$B \to B_\pm = B \pm \nu d\varphi, \qquad \mathrm{W} \to \mathrm{W}_\pm = \mathrm{T}_3 B_\pm. \tag{3.9}$$

The fields W_-, B_- and W_+, B_+ should be used, respectively, in the northern and southern hemispheres, where they remain regular at the axis. These two locally regular gauges are related to each other in the equatorial region by the gauge transformation

$$\mathfrak{V} = \exp\left(i\nu\varphi(1+\tau_3)\right), \tag{3.10}$$

which is regular, because $2\nu = -n \in \mathbb{Z}$ [59]. However, for notational simplicity, we shall continue using the singular gauge as in (3.7).

We have

$$dB = \frac{n}{2}\sin\vartheta d\vartheta \wedge d\varphi, \tag{3.11}$$

while the electromagnetic Nambu tensor $\mathcal{F}$ from (2.26) and the 't Hooft tensor F from (2.37) are given by

$$\mathcal{F} = F = \frac{1}{e}dB = dA \quad \text{with} \quad A = \frac{1}{e}B, \tag{3.12}$$

while $\mathcal{Z} = Z = 0$. This describes the radial hypermagnetic field and radial magnetic field,

$$\mathrm{B} \equiv \mathrm{B}^r = \frac{n}{2r^2}, \qquad \mathcal{B} \equiv \mathcal{B}^r = \frac{\mathrm{B}}{e} = \frac{P}{r^2}. \tag{3.13}$$

The magnetic field is identical to that of a Dirac monopole with magnetic charge

$$P = \frac{n}{2e}, \qquad n \in \mathbb{Z}, \tag{3.14}$$

in agreement with Dirac's quantization condition [63].

The RN solution (3.7) can thus be interpreted as the gravitational extension of the flat space Dirac monopole, to which it reduces in the $\kappa \to 0$ limit, where one can set $N(r) = 1$.

In what follows, we shall use the term "magnetic charge" to refer not only to P but also to Q defined in (3.6), as well as to the integer n.

The mass of the RN black hole is bounded below,

$$M \geq |Q|, \tag{3.15}$$

where the bound is saturated in the extremal limit, where $r_h = M = |Q|$. In this limit, the function $N(r) = (1 - r_h/r)^2$ develops a double zero at the horizon, making it degenerate and causing the surface gravity to vanish.

The hairy black holes studied below approach the RN solution (3.7) in the far-field region. Remarkably, the inequality (3.15) is violated for the extremal and near-extremal hairy black holes; we shall see later that their mass M is smaller than their charge $|Q|$.

1. Bertotti-Robinson solution

The metric of the extremal RN solution, where $N = (1 - r_h/r)^2$, can be rewritten in terms of a new radial coordinate $\eta \in (-\infty, \infty)$ defined by

$$d\eta = \frac{dr}{r\sqrt{N}} \Rightarrow r = (1+e^{\eta})r_h. \tag{3.16}$$

Rescaling the time coordinate by a constant factor, the line element takes the form

$$ds^2 = r_h^2\Big\{-\frac{e^{2\eta}}{(1+e^{\eta})^2}dt^2 + (1+e^{\eta})^2(d\eta^2+d\vartheta^2+\sin^2\vartheta d\varphi^2)\Big\}. \tag{3.17}$$

The horizon is at $\eta \to -\infty$, where the line element reduces to

$$ds^2 = r_h^2\{-e^{2\eta}dt^2 + d\eta^2 + d\vartheta^2 + \sin^2\vartheta d\varphi^2\}. \tag{3.18}$$

This is the Bertotti-Robinson metric [64,65], a solution valid for all $\eta \in (-\infty,\infty)$, describing the direct product geometry $AdS_2 \times S^2$. The B, W, Φ fields remain as in (3.7), while the radial magnetic and hypermagnetic fields are given by (3.13) with $r = r_h = |Q|$.

B. Reissner-Nordström-de Sitter solution

Another simple solution of (3.4) and (3.5) arises when the Higgs field vanishes:

$$f=1, \quad \phi=0, \quad \sigma=1, \quad N=1-\frac{2M}{r}+\frac{g^2Q^2}{r^2}-\frac{\Lambda}{3}r^2, \tag{3.19}$$

with the same Q as in (3.6) and

$$\Lambda = \frac{\kappa\beta}{8}. \tag{3.20}$$

Here, the Higgs field remains in the false vacuum, where $\Phi = 0$, and its potential acts as an effective cosmological constant, making the spacetime geometry RN-de Sitter (RNdS). The B field remains identical to that of the RN solution, while the W field is pure gauge. By performing a gauge transformation [Eq. (7.29) below], one can set $\mathrm{W} = 0$, making the full electroweak symmetry manifest.

Since $\mathrm{W}^a_{\mu\nu} = 0$, Eq. (2.26) gives

$$\mathcal{F}_{\mu\nu} = \frac{g}{g'}B_{\mu\nu} = \frac{g^2}{e}B_{\mu\nu}. \tag{3.21}$$

This corresponds to the radial hypermagnetic and magnetic fields:

$$\mathrm{B} = \frac{n}{2r^2}, \qquad \mathcal{B} = \frac{g^2\mathrm{B}}{e} = \frac{g^2P}{r^2}. \tag{3.22}$$

Thus, the magnetic charge is now $g^2P = g^2n/(2e) = gn/(2g')$, which does not satisfy the standard Dirac quantization condition. This is expected, as the system is not in the Higgs vacuum and standard electrodynamics does not apply.

However, the hypercharge field B can still be made regular via removing the string singularity by using the same gauge transformations as in the RN case. Notably, while the magnetic charge transforms as $P \to g^2P$ compared to the RN case, in (3.19) we have $Q^2 \to g^2Q^2$, not $Q^2 \to g^4Q^2$.

1. Extremal limit

The function $N(r)$ in (3.19) has three positive roots, corresponding to the inner black hole horizon, the outer black hole horizon r_h, and the cosmological horizon r_c. The value of r_h is bounded below as

$$r_h \geq r_{\mathrm{ex}} = \sqrt{\frac{1-\sqrt{1-4g^2\Lambda Q^2}}{2\Lambda}} = g|Q|\left(1+\frac{g^2Q^2\Lambda}{2}+\ldots\right) = g|Q| + \mathcal{O}(n^3\kappa^{5/2}). \tag{3.23}$$

Furthermore, we have

$$1-2\Lambda r_{\mathrm{ex}}^2 = \sqrt{1-\frac{Q^2}{Q_{\mathrm{m}}^2}} \equiv \lambda^2 \quad \text{with} \quad Q_{\mathrm{m}} = \frac{1}{2g\sqrt{\Lambda}} \approx \frac{1.17}{\sqrt{\kappa}}. \tag{3.24}$$

The lower bound $r_h = r_{\mathrm{ex}}$ corresponds to the extremal limit, where the two black hole horizons merge, forming a degenerate horizon. In this case, the function $N(r)$ factorizes as

$$N(r) = k^2(r)\left(1-\frac{r_{\mathrm{ex}}}{r}\right)^2, \qquad k^2(r) = 1-\frac{\Lambda}{3}[r^2+2r_{\mathrm{ex}}r+3(r_{\mathrm{ex}})^2]. \tag{3.25}$$

After a coordinate transformation similar to (3.16), the horizon limit $r \to r_{\mathrm{ex}}$ leads to an independent solution of the Einstein equations with an $AdS_2 \times S^2$ geometry, similar to (3.18):

$$ds^2 = r_{\mathrm{ex}}^2\{-e^{2\lambda\eta}dt^2 + d\eta^2 + d\vartheta^2 + \sin^2\vartheta d\varphi^2\}, \qquad B = -\frac{n}{2}\cos\vartheta d\varphi, \qquad \mathrm{W} = \Phi = 0, \tag{3.26}$$

with $\eta \in (-\infty,\infty)$ and λ defined in (3.24). A more detailed discussion of this will be provided in Appendix E.

The positive root of $k^2(r)$ determines the position of the cosmological horizon r_c, which is typically much larger than the black hole horizon $r_{\rm ex}$ due to the smallness of κ:

$$r_c = \sqrt{\frac{3}{\Lambda} - 2r_{\rm ex}^2} - r_{\rm ex} = \sqrt{\frac{24}{\beta\kappa}} + \mathcal{O}(n\sqrt{\kappa}) \gg r_{\rm ex}$$
$$= \frac{\sqrt{\kappa}|n|}{2\sqrt{2}g'} + \mathcal{O}(n^3\kappa^{5/2}). \tag{3.27}$$

However, as the magnetic charge increases and $Q = \sqrt{\kappa/2}P$ approaches $Q_{\rm m}$, the horizons r_c and $r_{\rm ex}$ approach each other. In the $Q \to Q_{\rm m}$ limit, $N(r)$ develops a triple zero, and one obtains

$$P = \frac{n}{2e} = \sqrt{\frac{2}{\kappa}}Q_{\rm m} \Rightarrow |n| = \frac{4g'}{\sqrt{\beta\kappa}} = 2.60 \times 10^{32},$$
$$r_{\rm c} = r_{\rm ex} = \frac{1}{\sqrt{2\Lambda}} = \frac{2}{\sqrt{\beta\kappa}}, \tag{3.28}$$

which corresponds to the dimensionful radius $\boldsymbol{r}_c = r_c \boldsymbol{l}_0 = 3$ cm.

Further increasing the magnetic charge would lead to the appearance of a naked singularity. Therefore, the extremal RNdS black holes exist only for $|Q| \leq Q_{\rm m}$.

Although the extremal [and nonextremal] RNdS solution is not asymptotically flat, we will see in the following that its horizon limit is the same as that of the asymptotically flat extremal hairy black holes.

IV. PERTURBATIONS AROUND THE RN BLACK HOLE

The RN solution (3.7) encapsulates an important feature: when its magnetic field becomes sufficiently large at the horizon, this should trigger the electroweak condensation [47,48], leading to an instability. As the condensate just begins to form, it can be described perturbatively and viewed as the "hair" that appears around the black hole.

Therefore, we now consider small perturbations around the RN solution (3.7):

$$\mathrm{g}_{\mu\nu} \to \mathrm{g}_{\mu\nu} + \delta\mathrm{g}_{\mu\nu}, \qquad \mathrm{W}^a_\mu \to \mathrm{W}^a_\mu + \delta\mathrm{W}^a_\mu,$$
$$B_\mu \to B_\mu + \delta B_\mu, \qquad \Phi \to \Phi + \delta\Phi. \tag{4.1}$$

Assuming the unitary gauge, where $\Phi = (0, \phi_2)^{\rm T}$ with real valued ϕ_2, and linearizing the field equations with respect to the perturbations, the equation for

$$w_\mu = \frac{1}{g}(\delta\mathrm{W}^1_\mu + i\delta\mathrm{W}^2_\mu) \tag{4.2}$$

decouples from the rest and reduces to the complex Proca equation:

TABLE I. Values of r_h^k for which Eq. (4.7) with $|n| = 2$ admits a k-node zero mode.

k	r_h^k
0	0.8942
1	4.306×10^{-2}
2	1.1723×10^{-3}
3	3.1180×10^{-5}
4	8.2879×10^{-7}
5	2.2029×10^{-8}
6	5.8553×10^{-10}
7	1.5563×10^{-11}
8	4.1367×10^{-13}
9	1.0997×10^{-14}
10	3.3758×10^{-16}
11	1.2763×10^{-16}
12	1.2379×10^{-16}
13	1.2369×10^{-16}
14	1.23688×10^{-16}

$$\mathcal{D}^\mu w_{\mu\nu} + ieF_{\nu\sigma}w^\sigma = m_{\rm w}^2 w_\nu. \tag{4.3}$$

Here $w_{\mu\nu} = \mathcal{D}_\mu w_\nu - \mathcal{D}_\nu w_\mu$, with $\mathcal{D}_\mu = \nabla_\mu + ieA_\mu$, and $A_\mu = B_\mu/e$ is the background field. One has $F_{\mu\nu} = \partial_\mu A_\nu - \partial_\nu A_\mu$. We recall that $B_\mu dx^\mu = -(n/2)\cos\vartheta d\varphi$, where $n \in \mathbb{Z}$.

To separate the angular variables in (4.3), we set

$$w_\mu dx^\mu = w_{\rm m} \ \text{ if } n > 0, \ \text{ and } \ w_\mu dx^\mu = \bar{w}_{\rm m} \ \text{ if } \ n < 0, \tag{4.4}$$

where the bar denotes complex conjugation, and

$$w_{\rm m}(t, r, \vartheta, \varphi) = e^{i\omega t - i{\rm m}\varphi}\psi(r)(\sin\vartheta)^j \left(\tan\frac{\vartheta}{2}\right)^{\rm m}$$
$$\times (d\vartheta - i\sin\vartheta d\varphi). \tag{4.5}$$

Here, the orbital angular momentum is

$$j = \left|\frac{n}{2}\right| - 1 \equiv j(n), \qquad |n| \geq 2, \tag{4.6}$$

and ${\rm m} \in [-j, j]$ is the azimuthal number. The values $n = \pm 1$ are excluded because $w_{\rm m}$ is then unbounded at $\vartheta = 0, \pi$, and the perturbation theory does not apply.

Injecting (4.5) into (4.3), the problem reduces to a Schrödinger-type equation,

$$\left(-\frac{d^2}{dr_\star^2} + N(r)\left[m_{\rm w}^2 - \frac{|n|}{2r^2}\right]\right)\psi(r) = \omega^2\psi(r). \tag{4.7}$$

Here, $N(r)$ is the metric coefficient in the RN solution (3.6), and the tortoise radial coordinate $r_\star$ is defined by $dr_\star = dr/N(r)$. If this equation admits negative modes, that is, bounded solutions with $\omega^2 < 0$, then perturbations grow in time, and the background is unstable.

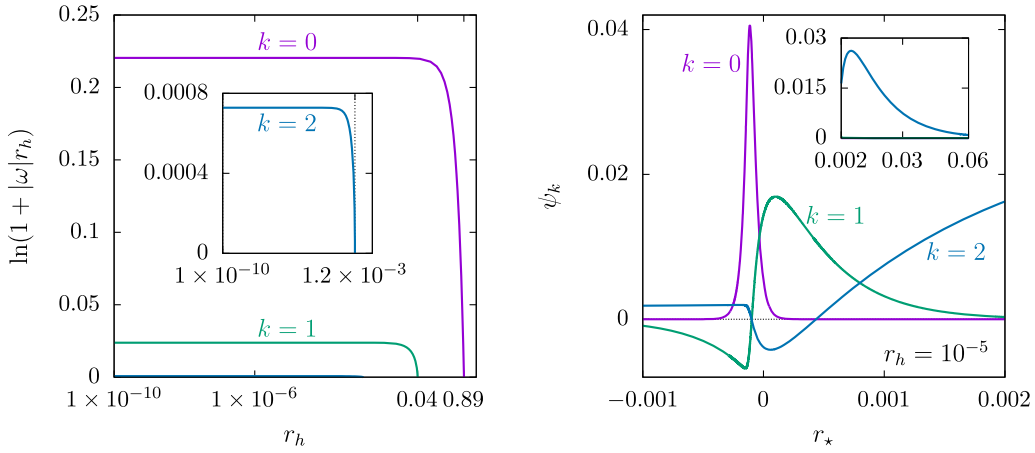


FIG. 1. Left: the rescaled eigenvalue $|\omega|\times r_h$ against r_h for the bound state solutions of (4.7) with $k=0,1,2$ nodes. Right: the profiles of the bound state eigenfunctions $\psi_k(r_*)$ with $k=0$, 1, 2 nodes against the radial tortoise coordinate $r_\star$ for $r_h=10^{-5}$.

In the flat space limit, where $N(r)=1$ and the RN solution reduces to the Dirac monopole, Eq. (4.7) admits infinitely many bound states with $\omega^2<0$. Indeed, if $\omega=0$ and $r\ll 1$, one can neglect $m_{\rm W}^2$ in the potential, and the solution is

$$\psi(r)=\sqrt{r}\cos\left(\sqrt{2|n|-1}\ln(\sqrt{r})\right).$$

This function oscillates infinitely many times as $r\to 0$; hence it does not correspond to the ground state. Therefore, there should be eigenstates with $\omega^2<0$. It follows that the Dirac monopoles are unstable with respect to developing the electroweak condensate [58], except for $n=\pm1$, when the perturbation theory does not apply.

In curved space, the range of the radial coordinate r in (4.7) is restricted to the outer black hole region, $r\geq r_h$, which bounds the attractive term $-|n|/(2r^2)$ in the potential. As a result, large black holes are stable, while the small ones exhibit instabilities characterized by negative modes—normalizable solutions of (4.7) with $\omega^2<0$.

By varying the black hole size, one can identify the threshold radius $r_h=r_h^0(n)$, for which the first instability just settles in as a zero mode—normalizable solution of (4.7) with $\omega=0$. This should occur when the hypermagnetic field at the horizon becomes sufficiently strong to trigger the electroweak condensation, leading to the condition

$$|\mathrm{B}(r_h^0)|=\frac{|n|}{2(r_h^0)^2}\simeq m_{\rm W}^2=\frac{g^2}{2}\Rightarrow r_h^0\simeq\frac{\sqrt{|n|}}{g}=1.13\times\sqrt{|n|}. \tag{4.8}$$

Numerical solutions to Eq. (4.7) for small $|n|$ yield actually slightly smaller values of $r_h^0(n)$ [see Table II below]. This discrepancy is explained by the fact that the estimate $|\mathrm{B}|=m_{\rm W}^2$ is obtained for a field orthogonal to a plane, not to a spherical horizon. However, when $|n|\gg 1$, the horizon becomes large and locally approximates a plane. In this regime, the numerical results recover the expected scaling $r_h^0(n)=\sqrt{|n|}/g+\cdots$, where the dots denote terms that vanish as $|n|\to\infty$.

For $|n|=2$, where $j(n)=0$, the perturbations in (4.5) are spherically symmetric. Starting from a large value of r_h and gradually decreasing it, the first zero mode appears for $r_h^0(2)\approx 0.89$, with the corresponding wave function $\psi_0(r)$ being *nodeless*. As r_h decreases further, this solution becomes a negative mode, with $\omega_0^2<0$. However, when $r_h=r_h^1(2)\approx 0.04$, the equation develops a second zero mode $\psi_1(r)$, which has *one node*.

As r_h continues to decrease, $\psi_1(r)$ also becomes a negative mode, alongside the nodeless $\psi_0(r)$. Further modes with an increasing number of nodes will continue to develop as the black hole size shrinks. In practice, we obtain these bound state solutions by applying the numerical multiple shooting method [see Ref. [41] for details].

Reducing r_h all the way down to the minimal value $r_h=|Q|$, Eq. (4.7) develops a total of 15 bound states. The values $r_h=r_h^k$ for which the k-node zero mode appears are shown in Table I. For $r_h<r_h^k$, each zero mode becomes negative, and the number of instabilities increases. For example, at $r_h=10^{-5}$, there are four negative modes; their profiles $\psi_k(r_\star)$ and the values of $|\omega_k(r_h)|\times r_h$ for $k=0$, 1, 2 are shown in Fig. 1.

TABLE II. Values $r_h^k(n)$ for which Eq. (4.7) admits a k-node zero mode.

n	2	4	6	10	20	40	100	200
$r_h^0(n)$	0.894	1.465	1.927	2.682	4.109	6.164	10.290	14.966
$r_h^1(n)$	0.043	0.245	0.508	1.054	2.274	4.191	8.202	12.823
$r_h^2(n)$	0.001	0.024	0.089	0.306	1.066	2.627	6.342	10.829

The eigenvalues $\omega_k^2(r_h) \leq 0$ start from zero at $r_h = r_h^k$ and then decrease as r_h gets smaller. However, the product $|\omega| r_h$ rapidly approaches a constant value.

In summary, small RN black holes with $|n| = 2$ are unstable with respect to the formation of an electroweak condensate. Each new instability manifests as a zero mode $\psi_k(r)$ at $r_h = r_h^k(2)$, which represents a static deformation of the RN black hole by the condensate that begins to form. This can be viewed as a perturbative approximation of a new static hairy solution that merges with the RN family for $r_h = r_h^k$ but deviates from it for $r_h < r_h^k$. The new solutions are spherically symmetric since $j(n) = 0$ for $|n| = 2$.

The same arguments apply for $|n| > 2$, where $j(n) > 0$ and the solutions (4.5) are no longer spherically symmetric. A zero mode $\psi_k(r)$ that appears for $r_h = r_h^k(n)$ then describes a static deformation of the RN black hole by a nonspherically symmetric condensate. This deformation generalizes to a static, nonperturbative hairy solution for $r_h < r_h^k(n)$. The values of $r_h^k(n)$ for $k = 0, 1, 2$ and $n > 2$ are given in Table II and shown in Fig. 2. The profiles of the nodeless zero mode ψ_0 in Fig. 2 show that the solution becomes increasingly localized at the horizon when n increases.

It is worth mentioning the analytical formula obtained by solving Eq. (4.7) within the WKB approximation [66]:

$$r_h^k(n) = \frac{\sqrt{|n|}}{g}\left(1 - \frac{2}{\sqrt{|n|}}\left(k + \frac{1}{2}\right)\right), \quad k = 0, 1, 2\ldots, \quad |n| \gg 1. \tag{4.9}$$

For $n = 200$, this gives values of $r_h^k(n)$ that agree with those in the last column of Table II, with relative discrepancies of 0.4%, 1%, and 4% for $k = 0$, 1, 2, respectively. The agreement is reasonable.

To recapitulate, Eq. (4.7) admit bound state solutions with $\omega = 0$ for discrete values $r_h^k(n)$ of the black hole size. These zero modes can be used for a perturbative approximation of new hairy solutions that exist for $r_h < r_h^k(n)$. The hairy solutions are spherically symmetric only for $|n| = 2$, while for $|n| > 2$, the spherical symmetry is lost.

V. SPHERICALLY SYMMETRIC HAIRY SOLUTIONS FOR $n = \pm 2$

As explained above, the RN solution (3.7) with $|n| = 2$ becomes unstable with respect to the formation of a spherically symmetric condensate when the horizon radius is small. This instability is expected to lead to the emergence of more general static and spherically symmetric non-Abelian solutions describing hairy black holes. Such solutions must satisfy Eq. (3.4).

Notably, except for $|n| = 2$, Eq. (3.4e) requires that $f' = f\phi = 0$, which only permits the simplest Abelian solutions described above. However, for $|n| = 2$, we have $\nu^2 - 1 = 0$, so Eq. (3.4e) is automatically satisfied, allowing for solutions with nonconstant $f(r)$ and $\phi(r)$.

Such solutions were previously reported in Ref. [43]; below, we reproduce them and highlight their most important features. Although the two signs of $n = \pm 2$ correspond to two values of the magnetic charge $P = n/(2e) = \pm 1/e$, the radial amplitudes $N(r), \sigma(r), f(r), \phi(r)$ are the same in both cases.

Equation (3.4d) can be solved as

$$\sigma(r) = \exp\left(-\kappa \int_r^\infty \frac{\mathcal{U}_1}{r}\, dr\right), \tag{5.1}$$

using which the remaining Eqs. (3.4a)–(3.4c) reduce to

$$(Nf')' + \frac{\kappa}{r}\mathcal{U}_1 N f' = \left(\frac{f^2 - 1}{r^2} + \frac{g^2}{2}\phi^2\right) f, \tag{5.2a}$$

$$(r^2 N\phi')' + \kappa r \mathcal{U}_1 N\phi' = \left(\frac{\beta r^2}{4}(\phi^2 - 1) + \frac{1}{2}f^2\right)\phi, \tag{5.2b}$$

$$1 - (rN)' = \kappa\left(N\mathcal{U}_1 + \mathcal{U}_0 + \frac{1}{2g'^2 r^2}\right). \tag{5.2c}$$

The simplest solution is the RN for which $f = 0$, $\phi = 1$, and N is given by (3.6). Perturbing this solution as $f \to \delta f$, $\phi \to 1 + \delta\phi$, and $N \to N + \delta N$, and then linearizing the equations with respect to the static perturbations, yield

$$(N\delta f')' = \left(-\frac{1}{r^2} + m_{\rm W}^2\right)\delta f, \qquad \frac{1}{r^2}(r^2 N\delta\phi')' = m_{\rm H}^2\delta\phi,$$
$$(r\delta N)' = 0. \tag{5.3}$$

The first of these equations is precisely Eq. (4.7) with $|n| = 2$ and $\omega = 0$. As we know, this equation admits a nontrivial solution for $r_h = r_h^0(2) = 0.894$, and we expect this perturbative zero mode to generalize to a nonperturbative solution of Eq. (5.2) when $r_h < 0.894$.

Assuming that at the horizon $r = r_h$, where $N(r_h) = 0$ and $N'(r_h) \equiv N'_h > 0$, the equations imply

$$N'_h = \frac{1}{r_h}\left(1 - \kappa\mathcal{U}_{0h} - \frac{\kappa}{2g'^2 r_h^2}\right),$$
$$f'_h = \frac{1}{N'_h}\left(\frac{f_h^2 - 1}{r_h^2} + \frac{g^2}{2}\phi_h^2\right) f_h,$$
$$\phi'_h = \frac{1}{r_h^2 N'_h}\left(\frac{\beta r_h^2}{4}(\phi_h^2 - 1) + \frac{1}{2}f_h^2\right)\phi_h, \tag{5.4}$$

where the subscript h denotes the value at $r = r_h$. This determines the boundary conditions at the horizon in terms of f_h and ϕ_h.

For $r \to \infty$, the perturbations should vanish, and the solutions should approach the RN form. Thus, we have in

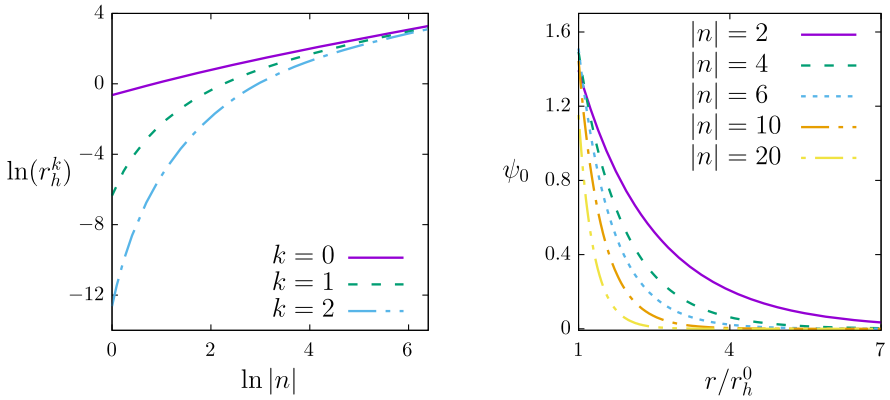


FIG. 2. The RN horizon radius $r_h^k(n)$, for which there exists a k-node zero mode $\psi_k(r)$ (left), and the profile of the fundamental zero mode $\psi_0(r)$ (right).

this limit

$$N = 1 - \frac{2M}{r} + \delta N_{\mathcal{N}}, \qquad f = C_f e^{-m_{\rm w} r} + \delta f_{\mathcal{N}},$$
$$\phi = 1 + \frac{C_\phi}{r} e^{-m_{\rm H} r} + \delta\phi_{\mathcal{N}}. \tag{5.5}$$

Here, M, C_f, C_ϕ are integration constants corresponding to the massless Newtonian mode and the two massive linear modes described by (5.3), while $\delta N_{\mathcal{N}}$, $\delta f_{\mathcal{N}}$, $\delta\phi_{\mathcal{N}}$ contain the subleading terms and nonlinear corrections. These expressions determine the boundary conditions at large r. The values of $\delta N_{\mathcal{N}}$, $\delta f_{\mathcal{N}}$, $\delta\phi_{\mathcal{N}}$ can be obtained by converting (5.2) into integral equations and iterating [see Ref. [41] for details].

Integrating the equations with the above boundary conditions and adjusting the values of the five free parameters $f_h, \phi_h, M, C_f, C_\phi$ within the numerical multiple shooting method [67], yield global solutions in the region $r > r_h$.

There always exists the trivial RN solution with $f(r) = 0, \phi(r) = 1$, but for $r_h < 0.894$, we also find solutions with nonconstant $f(r)$ and $\phi(r)$ that increasingly deviate from the RN solution as r_h decreases.

The horizon radius r_h of these hairy black holes ranges within the limits $r_h \in [r_{\rm ex}, r_h^0 = 0.894]$. The maximal value r_h^0 corresponds to the bifurcation with the RN solution, while the minimal value $r_{\rm ex}$ determines the extremal solution for which $N_h' = 0$.

Notably, the formula (5.4) remain valid even as $N_h' \to 0$, provided that $f_h \to 1$, $\phi_h \to 0$, $f_h' \to 0$, $\phi_h' \to 0$, and $r_h \to r_{\rm ex}$. The value $r_{\rm ex}$ is determined as the root of the equation $N_h' = 0$ in (5.4). Remarkably, it coincides with the radius $r_{\rm ex} \approx g|Q|$ of the extremal RNdS solution in (3.23).

For $|n| = 2$ one finds $r_{\rm ex} \approx 1.09 \times 10^{-16}$, which is close to the Planck length.

Examples of hairy solutions for $r_h = 0.8$, $r_h = 0.24$, and the extremal solution with $r_h = r_{\rm ex}$ are shown in Fig. 3. The function $\sigma(r)$ (not shown in the figures) is determined by (5.1) and remains very close to unity since κ is very small. As r_h shrinks, the horizon value of the Higgs field ϕ_h decreases and approaches zero, while f_h increases and approaches unity, as illustrated in Figs. 3 and 4. This is a manifestation of symmetry restoration in the presence of a

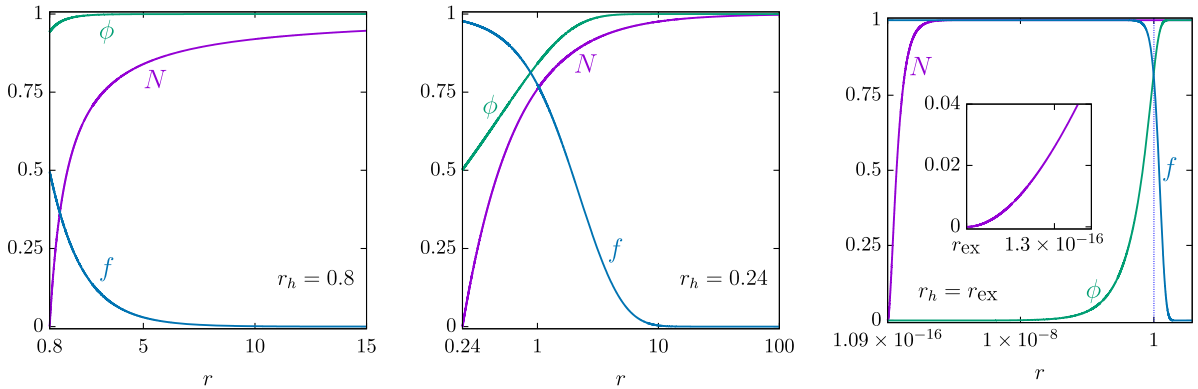


FIG. 3. Profiles of the hairy solutions with $r_h = 0.8$ (left), $r_h = 0.24$ (center), and the extremal solution with $r_h = r_{\rm ex} \approx 1.09 \times 10^{-16}$ (right). In the extremal case, $N(r_h) = N'(r_h) = 0$.

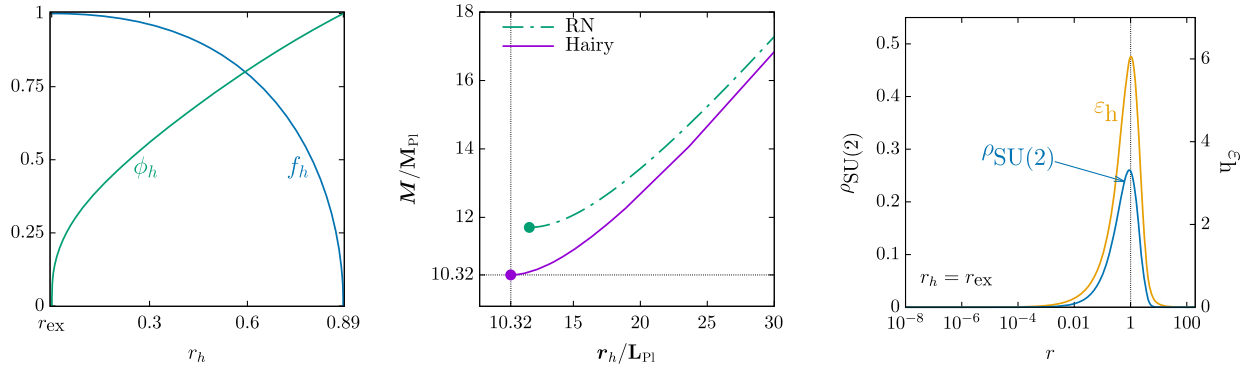


FIG. 4. Left: the horizon values $\phi_h = \phi(r_h)$ and $f_h = f(r_h)$ for the fundamental hairy solutions. Center: the mass of the hairy and RN solutions, with the former being always less energetic than the latter. Right: the radial densities of the magnetic charge and of the energy stored in the hair.

strong magnetic field [68]. When r_h is small, the U(1) hypermagnetic field, $|\mathrm{B}| = n/(2r^2) = \pm 1/r^2$ [as in (3.22)], becomes very large at the horizon. As a result, the value of ϕ_h is driven to zero, along with the value of the SU(2) field strength, which is proportional to $(1 - f_h^2)$. As f_h increases, the SU(2) component of the magnetic charge shifts *outside* the horizon. This phenomenon can be understood as follows.

A. The charge

Both the hairy black holes and the RN black hole share the same total magnetic charge measured at infinity, given by (2.52)

$$P = \frac{1}{4\pi}\oint_{S^2}\mathcal{F} = \frac{n}{2e} = \pm\frac{1}{e}. \tag{5.6}$$

In the RN case, this charge is entirely confined inside the horizon. For the hairy black hole, the charge remains inside the horizon according to the 't Hooft description. However, in the Nambu description, the charge splits as $P = P_{\mathrm{H}} + P_{\mathrm{h}}$, where P_{H} is contained inside the horizon, while P_{h} is distributed outside.

The exterior charge P_{h} is determined by integrating the magnetic charge density (2.51):

$$\begin{aligned} P_{\mathrm{h}} &= \int_{r>r_h}\tilde{\mathcal{J}}^0\sqrt{-\mathrm{g}}d^3x \equiv \int_{r_h}^{\infty}\rho_{\mathrm{SU}(2)}(r)dr = \frac{e}{8\pi}\int_{r>r_h}\epsilon^{ijk}\partial_i\psi_{jk}d^3x \\ &= -\frac{e}{8\pi}\oint_{r=r_h}\psi_{jk}dx^j\wedge dx^k = -\frac{e}{4\pi}\oint_{r=r_h}\psi_{\vartheta\varphi}d\vartheta d\varphi = f_h^2 g'^2 P. \end{aligned} \tag{5.7}$$

Here, we used the fact that the fields (3.2) are already in the unitary gauge. Thus, Eq. (2.40) implies that

$$g^2\psi_{\vartheta\varphi} = \mathrm{W}^1_\vartheta\mathrm{W}^2_\varphi - \mathrm{W}^2_\vartheta\mathrm{W}^1_\varphi = \nu f^2(r)\sin\vartheta, \tag{5.8}$$

which decays exponentially fast at infinity. The same result can be derived using the relation $P_{\mathrm{h}} = P - P(V)$, where $P(V)$ is given by (2.53) and V is the volume for $r < r_h$.

Since f_h increases when r_h decreases, the hair charge P_{h} grows from zero to its maximal value of g'^2P in the extremal limit. On the other hand, the horizon charge P_{H} decreases from P to g^2P in the extremal limit.

To summarize, within the Nambu description, the charged condensate outside the black hole horizon carries 22% of the total charge in the extremal limit, $P_{\mathrm{h}} = g'^2P \approx 0.22P$. The radial profile of the condensate charge density $\rho_{\mathrm{SU}(2)}$, as defined in Eq. (5.7), exhibits a peak at $r \approx 1$, as shown in Fig. 4.

Although the descriptions by Nambu and by 't Hooft appear to yield different results for $n = \pm 2$, for large $|n|$ they become mutually consistent and, in a certain sense, "dual" to each other, as we shall see below.

B. The ADM mass

The ADM mass is defined by Eq. (2.23), where $M = m(\infty)$ is the asymptotic value of the mass function appearing in the relation $N(r) = 1–2m(r)/r$. The mass function $m(r)$ satisfies Eq. (3.4c), given by

$$m'(r) = \frac{\kappa}{2}r^2T_{\hat{0}\hat{0}} = \frac{\kappa}{2}\left(\frac{1}{2g'^2r^2} + N\mathcal{U}_1 + \mathcal{U}_0\right), \tag{5.9}$$

and integrating this with the boundary condition $N(r_h) = 0$ yields

$$M = m(\infty) = \frac{r_h}{2} + \frac{\kappa}{4g'^2 r_h} + \frac{\kappa}{2}\int_{r_h}^{\infty} (N\mathcal{U}_1 + \mathcal{U}_0)dr. \tag{5.10}$$

For the RN solution (3.6), we have $f = 0, \phi = 1$, and $Q^2 = \kappa/(2e^2)$ for $n = \pm 2$. Using this in (5.10) yields the mass of the RN solution:

$$M_{\rm RN} = \frac{1}{2}\left(r_h + \frac{Q^2}{r_h}\right). \tag{5.11}$$

As shown in the central panel of Fig. 4, the mass M of hairy solutions is always below $M_{\rm RN}$ for a given r_h, so that hairy black holes are less energetic than the RN black holes of the same size.

As explained above, hairy black holes contain the charge $P_{\rm h} = f_h^2 g'^2 P$ in the hair and $P_{\rm H} = P - P_{\rm h}$ inside the horizon. This allows one to split the black hole mass into the "horizon mass" $M_{\rm H}$ and the "hair mass" $M_{\rm h}$,

$$M = \frac{1}{2}\left(r_h + (g^2 + (1 - f_h^2)^2 g'^2)\frac{Q^2}{r_h}\right) + M_{\rm h} \equiv M_{\rm H} + M_{\rm h}, \tag{5.12}$$

where $M_{\rm H}$ is the mass of the RN black hole with charge $P_{\rm H}$ and size r_h. It turns out that $M_{\rm H} \gg M_{\rm h}$, so $M \approx M_{\rm H}$ with very high precision.

The formula (5.12) will be justified below within a more general context. At present, we simply note that in the extremal limit, where $r_h = r_{\rm ex} \approx g|Q|$ and $f_h = 1$, the horizon mass $M_{\rm H}$ in (5.12) reduces to the sum of the first two terms on the right in (5.10). Hence, $M = M_{\rm H} + M_{\rm h}$, with

$$M_{\rm H} = \frac{1}{2}\left(r_{\rm ex} + \frac{g^2 Q^2}{r_{\rm ex}}\right) \approx g|Q|, \quad M_{\rm h} = \frac{\kappa}{2}\int_{r_h}^{\infty} (N\mathcal{U}_1 + \mathcal{U}_0)dr. \tag{5.13}$$

Here, the hair mass $M_{\rm h}$ is determined by the nonlinear f, ϕ fields forming the condensate, so this represents the mass of the condensate. It is instructive to consider their values rescaled according to (2.25):

$$\begin{aligned} \mathcal{M}_{\rm H} &= \frac{8\pi}{\kappa} M_{\rm H} = \frac{8\pi g}{\sqrt{2\kappa}e} + \mathcal{O}(\kappa^{7/2}) = 5 \times 10^{17}, \\ \mathcal{M}_{\rm h} &= \frac{8\pi}{\kappa} M_{\rm h} = 4\pi \int_{r_{\rm ex}}^{\infty} (N\mathcal{U}_1 + \mathcal{U}_0)dr \\ &\equiv \int_{r_{\rm ex}}^{\infty} \varepsilon_{\rm h}(r)dr = 15.759. \end{aligned} \tag{5.14}$$

The value of $\mathcal{M}_{\rm h}$ is obtained from our numerical solution. As a result, the hair mass is negligible as compared to the horizon mass, with $\mathcal{M}_{\rm h}/\mathcal{M}_{\rm H} \approx 3 \times 10^{-17}$, meaning $M \approx M_{\rm H}$.

The latter relation has an important consequence: although the mass of the extremal RN black hole is equal to the charge,

$$M_{\rm RN} = |Q|, \tag{5.15}$$

the mass of the extremal hairy solution is *smaller* than the charge:

$$M = M_{\rm H} + M_{\rm h} \approx M_{\rm H} \approx g|Q| \approx 0.88 \times |Q| < |Q|. \tag{5.16}$$

Therefore, the hairy black hole is energetically favored compared to the RN black hole. This remarkable feature can be explained by recalling that the Zeeman energy is negative. The W bosons contained in the condensate interact with the magnetic field of the black hole, which shifts their mass as $m_{\rm W}^2 \to m_{\rm W}^2 - |{\rm B}|$. This renders the condensate almost massless. Although the condensate carries 22% of the total charge, i.e., $Q_{\rm h} \equiv \sqrt{\kappa/2}P_{\rm h} = 0.22 \times Q$, its relative contribution to the total mass is only 3×10^{-17}. Therefore, the mass-to-charge ratio for the condensate is $M_{\rm h}/|Q_{\rm h}| \sim 10^{-16}$.

The radial energy density of the condensate, $\varepsilon_{\rm h}(r)$, defined in (5.14), has a sharp peak outside the horizon at $r \approx 1$, where the charge density $\rho_{{\rm SU}(2)}(r)$ is also maximal, as shown in Fig. 4. The condensate is gravitationally attracted by the black hole but repelled magnetically, as the horizon charge $P_{\rm H}$ and the condensate charge $P_{\rm h}$ have the same sign. Since $M_{\rm h}/|Q_{\rm h}| \sim 10^{-16}$, the magnetic repulsion is 16 orders of magnitude stronger than gravitational attraction.

This can be viewed as a manifestation of the weak gravity conjecture [69]. However, the condensate cannot be pushed away to infinity because it is composed of massive fields and encounters the Yukawa potential barrier at large r. Although the W bosons in the condensate are almost massless due to the negative Zeeman energy, the Z and Higgs bosons remain massive and follow the Yukawa law in the far field, which forces the condensate density to approach zero. As a result, the condensate is localized around the horizon.

Since $\mathcal{M} \approx \mathcal{M}_{\rm H}$, the dimensionful mass and horizon size of the extremal hairy black hole are given by

$$\begin{aligned} &\text{hairy}: \ \mathbf{M} = \frac{e^2}{4\pi\alpha}\mathcal{M} \times \boldsymbol{m}_0 \approx \frac{g}{\sqrt{\alpha}}\mathbf{M}_{\rm Pl} = 10.32 \times \mathbf{M}_{\rm Pl}, \\ &\boldsymbol{r}_{\rm ex} = r_{\rm ex}\boldsymbol{l}_0 \approx \frac{g}{\sqrt{\alpha}}\mathbf{L}_{\rm Pl}. \end{aligned} \tag{5.17}$$

For the extremal RN black hole with the same magnetic

charge, the mass and radius are obtained by dividing by g:

$$\text{RN:}\ \mathbf{M}=\frac{1}{\sqrt{\alpha}}\mathbf{M}_{\rm Pl}=11.71\times\mathbf{M}_{\rm Pl},\qquad \boldsymbol{r}_{\rm ex}=\frac{1}{\sqrt{\alpha}}\mathbf{L}_{\rm Pl}. \tag{5.18}$$

C. Extremal hairy black hole versus Cho-Maison monopole

For the extremal hairy black hole, one has $f_h=1$ and $\phi_h=0$, so that the horizon values of the fields correspond to the extremal RNdS solution (3.25). Therefore, the function $N(r)$ for the extremal hairy black hole has the same form as in (3.25),

$$N(r)=k^2(r)\left(1-\frac{r_{\rm ex}}{r}\right)^2\approx\left(1-\frac{r_{\rm ex}}{r}\right)^2. \tag{5.19}$$

Here, $r_{\rm ex}=g|Q|+\mathcal{O}(\kappa^{5/2})\sim 10^{-16}$ is determined by (3.23), and $k(r)$ interpolates between the same horizon limit as in (3.25), $k(r_{\rm ex})=\sqrt{1-2\Lambda r_{\rm ex}^2}=1+\mathcal{O}(\kappa^2)$, and $k(\infty)=1$. Hence, $k(r)\approx 1$. The function $N(r)$ quickly approaches unity, and already for $r\simeq 10^2\times r_{\rm ex}\sim 10^{-14}$, the geometry is practically flat. As a result, the massive fields described by $f(r)$ and $\phi(r)$ actually live in a flat geometry, and their profiles practically coincide with those for the flat space Cho-Maison monopole.

The Cho-Maison (CM) monopole [70] is the solution in the flat space limit, when $\kappa=0$ and $N=\sigma=1$, and Eq. (5.2) reduce to

$$f''=\left(\frac{f^2-1}{r^2}+\frac{g^2}{2}\phi^2\right)f,\quad (r^2\phi')'=\left(\frac{\beta r^2}{4}(\phi^2-1)+\frac{1}{2}f^2\right)\phi. \tag{5.20}$$

These equations admit a smooth solution with the boundary conditions for $0\leftarrow r\to\infty$:

$$1+\mathcal{O}(r^2)\leftarrow f(r)\to\mathcal{O}(e^{-m_{\rm w}r}),$$
$$\mathcal{O}(r^{\frac{\sqrt{3}-1}{2}})\leftarrow\phi(r)\to\mathcal{O}(e^{-m_{\rm H}r}). \tag{5.21}$$

This describes a magnetic monopole with the same magnetic charge $P=\pm 1/e$ as for the hairy black holes. The SU(2) part of the charge $g'^2P=0.22\times P$ is smoothly distributed in space in the condensate, while the U(1) part $g^2P=0.78\times P$ is pointlike and located at the origin. The latter carries the energy density $1/(2g'^2r^4)$, which renders the total monopole energy $E_{\rm mon}$ divergent. However, subtracting the divergent part leaves a finite value:

$$E_{\rm CM}=E_{\rm mon}-4\pi\int_0^\infty\frac{dr}{2g'^2r^2}=15.759,$$

[see Ref. [59] for details]. This is the same value as that in Eq. (5.14), where it corresponds to the energy of the condensate around the black hole.

The profiles of $f(r)$ and $\phi(r)$ for the extremal black hole in the region $r>r_{\rm ex}$ are very close to those for the CM monopole and converge to the latter pointwise in the $\kappa\to 0$ limit. Therefore, the extremal hairy black hole can be viewed as the CM monopole harboring in its center a tiny black hole whose radius is microscopically small compared to the size of the monopole itself.

As seen in Fig. 3 (right panel), the near-horizon region where the geometry essentially deviates from Minkowski space, $10^{-16}\le r\le 10^{-14}$, is *parametrically* small compared to the region containing the condensate, where $r\simeq 1$. The amplitudes $f(r)$ and $\phi(r)$ stay close to their horizon values $f_h=1,\phi_h=0$ in the interval that exceeds the horizon size by approximately 12 orders of magnitude, and only for $r\ge 10^{-4}$ they start to change. Therefore, the massive fields forming the condensate actually live in flat geometry and almost do not feel the presence of the black hole. However, the black hole is important because it regularizes the divergent part of the monopole energy by replacing it with the finite term $\mathcal{M}_{\rm H}$ in (5.14), so that the total energy becomes finite.

The hair mass $\mathcal{M}_{\rm h}$ of the extremal black hole is given by the integral in (5.14), where the integration starts at $r=r_{\rm ex}\sim\sqrt{\kappa}\sim 10^{-16}$. The regularized energy of the Cho-Maison monopole $E_{\rm CM}$ is given by the same integral, but the integration starts at $r=0$; hence $\mathcal{M}_{\rm h}=E_{\rm CM}+\mathcal{O}(\sqrt{\kappa})$.

To recapitulate, the extremal hairy solution can be viewed as a superposition of the flat space CM monopole of size $\sim$1 and a black hole of radius $\sim 10^{-16}$ [in electroweak units]. The tiny black hole almost does not affect the monopole configuration but renders its energy $E_{\rm mon}$ finite by providing the cutoff at the horizon. This can be illustrated as follows:

$$E_{\rm mon}=\lim_{\kappa\to 0}\frac{8\pi g}{\sqrt{2\kappa}e}+15.759=\infty$$
$$\Rightarrow\mathcal{M}=\frac{8\pi g}{\sqrt{2\kappa}e}+15.759=5\times 10^{17}+15.759. \tag{5.22}$$

When the gravity is taken into account, the divergent part of the monopole energy becomes finite, albeit large, and reduces to the black hole horizon mass $\mathcal{M}_{\rm H}=8\pi g/(\sqrt{2\kappa}e)$. The finite part of the monopole energy $E_{\rm CM}=15.759$ remains the same up to corrections of order 10^{-16} and becomes the mass of the black hole hair $\mathcal{M}_{\rm h}=15.759$.

D. Stability of the extremal hairy solution

The extremal hairy black hole with $n=\pm 2$ is expected to be stable. This expectation is motivated by its similarity to the flat-space Cho-Maison monopole, which has been

proven to be stable [58]. Although a complete stability analysis that includes gravitational effects is not yet available, the close resemblance between the electroweak field configurations with and without gravity suggests that the stability properties should be consistent.

Next, since the condensate significantly reduces the black hole mass, the hairy black hole with $M \approx 0.88|Q|$ cannot transition to a RN black hole, for which $M \geq |Q|$. This would require one either to increase the energy or to reduce the magnetic charge, but the latter is conserved due to the field topology. It is conceivable that the hairy black hole could decay into a lower-energy state. However, the perturbative analysis in the next section suggests that the spherical condensate with $n = \pm 2$ already represents the absolute energy minimum.

Therefore, the extremal hairy black holes with $n = \pm 2$ are likely to be stable.

E. The excited solutions

For the sake of completeness, it is important to mention also the excited zero mode solutions of Eq. (4.7), $\psi(r) = \psi_k(r)$ with $k > 0$, which exist for specific horizon values $r_h = r_h^k(n)$ shown in Tables I and II. These excited solutions can also be promoted to static hairy black holes at the nonperturbative level.

As an example, consider the one-node zero mode solution $\psi_1(r)$, which exists for $r_h^1(2) = 4.3 \times 10^{-2}$. When this solution is used as the input for the numerical solver and the horizon radius is set to $r_h = 4 \times 10^{-2} < r_h^1(2)$, we find a static hairy solution for which $f(r)$ is not monotonic, but instead exhibits a node. Additionally, for the same value of r_h, there is also the black hole solution with a monotonic $f(r)$.

Thus, for $r_h = 4 \times 10^{-2}$, there are two distinct hairy solutions: one fundamental and one excited. Similarly, for $r_h < r_h^2(2) = 1.1 \times 10^{-3}$, a second radial excitation is found, and so on.

The excited solutions have not been described in the literature. Their profiles for $r_h = 10^{-6}$ are shown in Fig. 5.

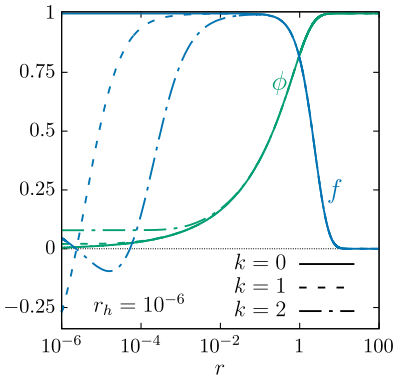


FIG. 5. The amplitudes $f(r)$ and $\phi(r)$ for the fundamental hairy solution with $r_h = 10^{-6}$ and for its first two radial excitations.

However, such solutions are presumably unstable, and we will not discuss them anymore.

VI. PERTURBATIVE DESCRIPTION OF HAIRY BLACK HOLES WITH $|n| > 2$

We considered above spherically symmetric hairy solutions with magnetic charge $n = \pm 2$, beginning with their perturbative description in terms of Eqs. (4.3)–(4.7), and later passing to the fully nonperturbative description. Now, we aim to extend the analysis to cases where $n > |2|$, when spherical symmetry is no longer preserved. As the first step, we will apply the perturbative approach.

Let us get back to Eqs. (4.3)–(4.7), which describe perturbations of the RN black hole. We choose the horizon radius $r_h = r_h^0(n)$ such that Eq. (4.7) admits a zero mode solution $\psi(r) = \psi_0(r)$. Substituting this into (4.5) yields a static solution of the Proca equation (4.3), which describes the electroweak condensate beginning to form on the RN background:

$$w_\mu dx^\mu = w_{\rm m}(r, \vartheta, \varphi) = e^{-i{\rm m}\varphi}\psi(r)(\sin\vartheta)^j \left(\tan\frac{\vartheta}{2}\right)^{\rm m}(d\vartheta - i\sin\vartheta d\varphi). \tag{6.1}$$

It is assumed here that $n > 0$, while for $n < 0$, one should replace this expression by its complex conjugate. We have $j = |n/2| - 1$. This solution is not unique since the azimuthal number ${\rm m} \in [-j, j]$ can take several values. Thus, the general solution is given by

$$w_\mu dx^\mu = \sum_{\rm m} c_{\rm m} w_{\rm m}(r, \vartheta, \varphi), \tag{6.2}$$

where $c_{\rm m}$ are constant coefficients. This solution is defined up to an overall sign, which can be flipped by the gauge transformation (2.15) generated by $\mathfrak{V} = -\tau_3$. The effect of this transformation is ${\rm T}_1 \to -{\rm T}_1$ and ${\rm T}_2 \to -{\rm T}_2$, resulting in $w \to -w$, while the RN background remains unchanged.

Since w must be a single-valued function of φ modulo a gauge transformation, it should either be invariant under $\varphi \to \varphi + 2\pi$ or change sign. Therefore, since $w_{\rm m} \sim \exp(-i{\rm m}\varphi)$, the azimuthal number m must take either integer or half-integer values, regardless of the value of $j = |n|/2 - 1$, which can itself be either an integer or half integer.

Additionally, one must have $|{\rm m}| \leq j$, since otherwise the mode (6.1) would diverge at $\vartheta = 0$ or $\vartheta = \pi$. Consequently, the allowed values for m are as follows:

(i) if $j = 0$, then ${\rm m} = 0$;
(ii) if $j = \frac{1}{2}$, then ${\rm m} = \pm\frac{1}{2}$ or ${\rm m} = 0$;
(iii) if $j = 1$, then ${\rm m} = \pm\frac{1}{2}$ or ${\rm m} = 0, \pm 1$; and
(iv) if $j = \frac{3}{2}$, then ${\rm m} = \pm\frac{3}{2}, \pm\frac{1}{2}$ or ${\rm m} = 0, \pm 1$, etc.

Therefore, m assumes either $2j$ or $2j+1$ distinct values, among which $\mathrm{m}=0$ is always present.

If $|n|=2$, then $j=\mathrm{m}=0$, and there is only one coefficient c_0 in (6.2), which can be fixed by normalization; hence there is no ambiguity. For $|n|>2$ one has $j>0$, spherical symmetry is lost, and the azimuthal number m can take several values. As a result, there are several coefficients c_{m} in (6.2). Within the framework of linear perturbation theory, these coefficients are arbitrary, but higher-order perturbation theory imposes conditions on them. Specifically, the choice of these coefficients should minimize the energy of the condensate.

In what follows, we adopt the approach of [45], which involves expanding around the RN solution up to the second-order terms and then minimizing the energy. We neglect the backreaction of perturbations on the RN geometry, as it is proportional to κ.

A. Electroweak equations in the unitary gauge

Switching to the unitary gauge, where $\Phi=(0,\phi)^{\mathrm{T}}$ with ϕ being real valued, one defines the complex valued W field and its strength:

$$w_\mu=\frac{1}{g}(\mathrm{W}^1_\mu+i\mathrm{W}^2_\mu),\qquad w_{\mu\nu}=\mathcal{D}_\mu w_\nu-\mathcal{D}_\nu w_\mu, \tag{6.3}$$

where $\mathcal{D}_\mu=\nabla_\mu+i\mathrm{W}^3_\mu$. The electroweak Lagrangian in (2.13) then takes the following form:

$$\begin{aligned}-\mathcal{L}_{\mathrm{EW}}=&\frac{1}{4g'^2}(B_{\mu\nu})^2+\frac{1}{4g^2}(\mathrm{W}^3_{\mu\nu})^2+\frac{1}{4}|w_{\mu\nu}|^2\\&+(\partial_\mu\phi)^2+\frac{1}{4}(g^2|w_\mu|^2+(B_\mu-\mathrm{W}^3_\mu)^2)\phi^2\\&+\frac{\beta}{8}(\phi^2-1)^2,\end{aligned} \tag{6.4}$$

with $B_{\mu\nu}=\partial_\mu B_\nu-\partial_\nu B_\mu$, where

$$\mathrm{W}^3_{\mu\nu}=\partial_\mu\mathrm{W}^3_\nu-\partial_\nu\mathrm{W}^3_\mu+g^2\psi_{\mu\nu},\quad \psi_{\mu\nu}=\frac{i}{2}(w_\mu\bar w_\nu-w_\nu\bar w_\mu). \tag{6.5}$$

The Nambu electromagnetic field and Z field, as given in (2.26), become

$$\begin{aligned}e\mathcal{F}_{\mu\nu}&=g^2B_{\mu\nu}+g'^2\mathrm{W}^3_{\mu\nu}=eF_{\mu\nu}+e^2\psi_{\mu\nu},\\ \mathcal{Z}_{\mu\nu}&=B_{\mu\nu}-\mathrm{W}^3_{\mu\nu}=Z_{\mu\nu}-g^2\psi_{\mu\nu}.\end{aligned} \tag{6.6}$$

Here, $F_{\mu\nu}=\partial_\mu A_\nu-\partial_\nu A_\mu$ and $Z_{\mu\nu}=\partial_\mu Z_\nu-\partial_\nu Z_\mu$ are the 't Hooft fields, with the potentials

$$eA_\mu=g^2B_\mu+g'^2\mathrm{W}^3_\mu,\qquad Z_\mu=B_\mu-\mathrm{W}^3_\mu. \tag{6.7}$$

Notice that $\psi_{\mu\nu}$ in (6.5) is the same as in (2.40), while $F_{\mu\nu}$ is the same as in (2.37).

The electroweak equations (2.17) then take the form

$$\nabla^\mu F_{\nu\mu}=4\pi J_\nu, \tag{6.8a}$$

$$\nabla^\mu Z_{\nu\mu}+\frac{\phi^2}{2}Z_\nu=-4\pi\frac{g}{g'}J_\nu, \tag{6.8b}$$

$$\mathcal{D}^\mu w_{\mu\nu}+i(g^2\psi_{\nu\sigma}+gg'F_{\nu\sigma}-g^2Z_{\nu\sigma})w^\sigma=\frac{g^2\phi^2}{2}w_\nu, \tag{6.8c}$$

$$\nabla^\mu\nabla_\mu\phi=\frac{1}{4}(g^2w_\mu\bar w^\mu+Z_\mu Z^\mu)\phi+\frac{\beta}{4}(\phi^2-1)\phi. \tag{6.8d}$$

The gauge covariant derivative can be written as

$$\mathcal{D}_\mu=\nabla_\mu+i(eA_\mu-g^2Z_\mu), \tag{6.9}$$

and the current is

$$4\pi J_\nu=e\nabla^\sigma\psi_{\sigma\nu}+e\Im(\bar w^\sigma w_{\sigma\nu}). \tag{6.10}$$

One has $\mathcal{F}_{\mu\nu}=F_{\mu\nu}+e\psi_{\mu\nu}$, whose divergence yields

$$\begin{aligned}4\pi\mathcal{J}_\nu&=\nabla^\mu\mathcal{F}_{\nu\mu}=\nabla^\mu F_{\nu\mu}+e\nabla^\mu\psi_{\nu\mu}\\&=4\pi J_\nu-e\nabla^\mu\psi_{\mu\nu}=e\Im(\bar w^\sigma w_{\sigma\nu});\end{aligned} \tag{6.11}$$

hence the 't Hooft current and Nambu current are related to each other as follows:

$$J_\nu=\mathcal{J}_\nu+\frac{e}{4\pi}\nabla^\sigma\psi_{\sigma\nu}. \tag{6.12}$$

B. Condensate energy

Equation (6.8) admit the solution

$$A_\mu dx^\mu=-\frac{n}{2e}\cos\vartheta d\varphi,\quad Z_\mu=w_\mu=0,\quad \phi=1, \tag{6.13}$$

assuming the background geometry to be the RN given by (3.6) and (3.7).

Linearizing the equations around this solution, the only bounded solution for the first-order corrections of A_μ, Z_μ, ϕ is the trivial one; hence, these fields remain unchanged in the first perturbative order. However, the first-order correction for w_μ can be nontrivial since it fulfils the same Proca equation as in (4.3), whose bounded solution is given by Eq. (6.1) and (6.2) above. This solution has only two nonvanishing components, w_ϑ and $w_\varphi=-iw_\vartheta\sin\vartheta$ [assuming that $n>0$], implying the following relations:

$$|w_\mu|^2 \equiv w_\mu \bar{w}^\mu = \frac{2}{r^2}|\psi(r)|^2 \times \Theta(\vartheta,\varphi),$$
$$\Theta(\vartheta,\varphi) = (\sin\vartheta)^{2j}\sum_{\mathrm{k,m}} c_\mathrm{k} c_\mathrm{m}\left(\tan\frac{\vartheta}{2}\right)^{\mathrm{k+m}} e^{i(\mathrm{k-m})\varphi}. \quad (6.14)$$

The tensor $\psi_{\mu\nu} = -\psi_{\nu\mu}$, defined in (6.5), also has only two components,

$$\psi_{\vartheta\varphi} = -\psi_{\varphi\vartheta} = -\frac{r^2}{2}|w_\mu|^2 \sin\vartheta = -|\psi(r)|^2\Theta(\vartheta,\varphi)\sin\vartheta. \quad (6.15)$$

The nonzero components of the strength tensor $w_{\mu\nu}$ are

$$w_{r\vartheta} = -w_{\vartheta r} = \partial_r w_\vartheta, \qquad w_{r\varphi} = -w_{\varphi r} = \partial_r w_\varphi, \quad (6.16)$$

while

$$w_{\vartheta\varphi} = \partial_\vartheta w_\varphi - (\partial_\varphi + ieA_\varphi)w_\vartheta = w_{\varphi\vartheta} = 0. \quad (6.17)$$

As a result,

$$(\psi_{\mu\nu})^2 = \frac{1}{2}|w_\mu|^4,$$
$$|w_{\mu\nu}|^2 = 2N(r)\left|\frac{\psi'(r)}{\psi(r)}\right|^2 |w_\mu|^2 \equiv 2\Omega^2(r)|w_\mu|^2. \quad (6.18)$$

It follows that $\Im(\bar{w}^\sigma w_{\sigma\nu}) = 0$; hence the Nambu current vanishes, $\mathcal{J}_\mu = 0$, while the 't Hooft current (6.10) becomes

$$4\pi J_\mu = e\nabla^\sigma \psi_{\sigma\mu}. \quad (6.19)$$

At this point, it is important to emphasize the difference between the Nambu tensor $\mathcal{F}_{\mu\nu}$ and the 't Hooft tensor $F_{\mu\nu}$. The electric current $\mathcal{J}^\mu$ associated with $\mathcal{F}_{\mu\nu}$ vanishes in the second perturbative order, but the magnetic current $\tilde{\mathcal{J}}^\mu$ does not vanish and determines the magnetic charge density. Conversely, for the tensor $F_{\mu\nu}$ the situation is reversed:

$$\mathcal{J}^\mu = \frac{1}{4\pi}\nabla_\sigma \mathcal{F}^{\mu\sigma} = 0, \quad \tilde{\mathcal{J}}^0 = \frac{1}{4\pi}\nabla_\sigma \tilde{\mathcal{F}}^{0\sigma} = \frac{e}{8\pi\sqrt{-\mathrm{g}}}\epsilon^{ijk}\partial_i \psi_{jk},$$
$$J^\mu = \frac{1}{4\pi}\nabla_\sigma F^{\mu\sigma} = \frac{e}{4\pi}\nabla_\sigma \psi^{\sigma\mu}, \quad \tilde{J}^0 = \frac{1}{4\pi}\nabla_\sigma \tilde{F}^{0\sigma} = 0. \quad (6.20)$$

Therefore, $F_{\mu\nu}$ defines the electric current, whereas $\mathcal{F}_{\mu\nu}$ gives rise to the magnetic current. However, it should be noted that the electric current $\mathcal{J}^\mu$ starts deviating from zero at higher perturbative orders, while the magnetic current $\tilde{J}^\mu$ vanishes at all orders.

The nonzero components of J_μ are

$$J_\vartheta = \frac{e}{8\pi\sin\vartheta}\partial_\varphi |w_\mu|^2, \qquad J_\varphi = -\frac{e\sin\vartheta}{8\pi}\partial_\vartheta |w_\mu|^2. \quad (6.21)$$

This current is tangent to the horizon and orthogonal to the gradient of $|w_\mu|^2$. Restricting to $r = r_h$, the condition $|w_\mu|^2 = \text{const}$ determines lines on the horizon that are orthogonal to the gradient of $|w_\mu|^2$. Therefore, the current J^μ is tangent to the level lines of $|w_\mu|^2$.

The current, being quadratic in w_μ, acts as a source for the second-order correction $f_{\mu\nu} = \partial_\mu f_\nu - \partial_\nu f_\mu$ to the background electromagnetic field, leading to

$$F_{\mu\nu} = \partial_\mu A_\nu - \partial_\nu A_\mu + f_{\mu\nu} \equiv \overset{(0)}{F}_{\mu\nu} + f_{\mu\nu}, \quad (6.22)$$

with the same A_μ as in (6.13). The current also induces nonzero Z_μ and a deviation $\delta\phi = \phi - 1$. Expanding Eq. (6.8) to second order gives

$$\nabla^\mu f_{\nu\mu} = e\nabla^\sigma \psi_{\sigma\nu} \equiv 4\pi J_\nu^{(f)}, \quad (6.23a)$$

$$\nabla^\mu Z_{\nu\mu} + \frac{1}{2}Z_\nu = -g^2\nabla^\sigma \psi_{\sigma\nu} \equiv 4\pi J_\nu^{(Z)}, \quad (6.23b)$$

$$-\nabla^\mu \nabla_\mu \delta\phi + \frac{\beta}{2}\delta\phi = -\frac{g^2}{4}|w_\mu|^2 \equiv 4\pi J^{(\phi)}, \quad (6.23c)$$

whose solution is quadratic in c_m. Substituting this solution into (6.4) yields the condensate energy density, containing terms up to fourth order in c_m:

$$\mathcal{E}_\mathrm{cond} \equiv -\mathcal{L}_\mathrm{EW} = \frac{1}{4}(gF_{\mu\nu} + g'Z_{\mu\nu})^2 + \frac{1}{4}(g'F_{\mu\nu} - gZ_{\mu\nu} + g\psi_{\mu\nu})^2$$
$$+ \frac{1}{4}|w_{\mu\nu}|^2 + \frac{g^2}{4}|w_\mu|^2(1 + 2\delta\phi) + \frac{1}{4}(Z_\mu)^2 + (\partial_\mu\delta\phi)^2 + \frac{\beta}{2}\delta\phi^2. \quad (6.24)$$

This determines the condensate energy

$$E_{\rm cond} = \int \mathcal{E}_{\rm cond}\sqrt{-g}d^3x. \tag{6.25}$$

Integrating by parts, using Eq. (6.23), and omitting the zeroth-order contribution yields

$$E_{\rm cond} = E_w + E_{fZ\phi}, \tag{6.26}$$

where

$$\begin{aligned} E_w &= \int \left(\frac{e}{2}\overset{(0)}{F}_{\mu\nu}\psi^{\mu\nu} + \frac{g^2}{4}(\psi_{\mu\nu})^2 + \frac{1}{4}|w_{\mu\nu}|^2 + \frac{g^2}{4}|w_\mu|^2\right) \\ &\quad \times \sqrt{-g}d^3x \\ &= \int \left(\frac{g^2}{8}|w_\mu|^4 + \frac{\Omega^2(r) + m_{\rm W}^2(r)}{2}|w_\mu|^2\right)\sqrt{-g}d^3x, \\ E_{fZ\phi} &= 4\pi\int\left(-\frac{1}{2}f^\nu J_\nu^{(f)} - \frac{1}{2}Z^\nu J_\nu^{(Z)} - \delta\phi J^{(\phi)}\right)\sqrt{-g}d^3x. \end{aligned} \tag{6.27}$$

Here $\Omega^2(r)$ is defined in (6.18), while

$$m_{\rm W}^2(r) = m_{\rm W}^2 - |{\rm B}(r)| = \frac{g^2}{2} - \frac{|n|}{2r^2}, \tag{6.28}$$

where the last term arises from the $\overset{(0)}{F}_{\mu\nu}\psi^{\mu\nu}$ contribution to (6.27). The modulus $|n|$ appears because flipping the sign of n changes the signs of both $F_{\mu\nu}$ and $\psi_{\mu\nu}$. This explicitly demonstrates that the Zeeman interaction with the background field effectively reduces the W boson mass.

The E_w term can be computed using the already known first-order solution for w_μ, while $E_{fZ\phi}$ requires solving Eq. (6.23) to determine the second-order corrections f_μ, Z_μ, $\delta\phi$. These can be obtained through the following steps.

First, expand the function $\Theta(\vartheta,\varphi)$ defined in (6.14) over spherical harmonics:

$$\Theta(\vartheta,\varphi) = \sum_{J=0}^{2j}\sum_{M=-J}^{J} C_{JM}Y_{JM}(\vartheta,\varphi), \tag{6.29}$$

with $j = |n/2| - 1$. As explained above after Eq. (6.2), the azimuthal numbers k, m in Eq. (6.14) can either be all integers or all half integers. Therefore, their difference, k-m, is always an integer, which implies that the azimuthal number M in (6.29) must be an integer. Since $2j$ is also an integer, it follows that J must be an integer as well. Thus, Eq. (6.29) involves sums over integer values of J and M.

The next step is to introduce

$$X^{(I)}(r,\vartheta,\varphi) = \sum_{J=0}^{2j}\sum_{M=-J}^{J} R_{JM}^{(I)}(r)Y_{JM}(\vartheta,\varphi), \tag{6.30}$$

where the index I runs over f, Z, ϕ, and the radial functions satisfy the equation

$$\left(\frac{1}{q}\frac{d}{dr}qN\frac{d}{dr} - \frac{J(J+1)}{r^2} - m^2\right)R_{JM}^{(I)} = a\frac{\psi^2(r)}{r^2}C_{JM}, \tag{6.31}$$

with the following parameters:

$$\begin{aligned} &I = f\colon\ q = 1, \quad a = -e, \quad m^2 = 0; \\ &I = Z\colon\ q = 1, \quad a = g^2, \quad m^2 = m_{\rm Z}^2 = 1/2; \\ &I = \phi\colon\ q = r^2, \quad a = g^2/2, \quad m^2 = m_{\rm H}^2 = \beta/2. \end{aligned} \tag{6.32}$$

Since $f_{\mu\nu} = \partial_\mu f_\nu - \partial_\nu f_\mu$, Eq. (6.23) are fulfilled by

$$\begin{aligned} &f_\vartheta = \frac{1}{\sin\vartheta}\partial_\varphi X^{(f)}, \qquad f_\varphi = -\sin\vartheta\partial_\vartheta X^{(f)}, \\ &Z_\vartheta = \frac{1}{\sin\vartheta}\partial_\varphi X^{(Z)}, \qquad Z_\varphi = -\sin\vartheta\partial_\vartheta X^{(Z)}, \qquad \delta\phi = X^{(\phi)}. \end{aligned} \tag{6.33}$$

Injecting this solution into $E_{fZ\phi}$ in (6.27) gives, after some algebra,

$$E_{fZ\phi} = \frac{1}{2}\sum_{J,M}\bar{C}_{JM}\int_{r_h}^{\infty}|\psi(r)|^2\left\{\frac{J(J+1)}{r^2}(g^2R_{JM}^{(Z)} - eR_{JM}^{(f)}) + g^2R_{JM}^{(\phi)}\right\}dr, \tag{6.34}$$

and one should stress that the formula contains the complex conjugated $\bar{C}_{JM}$ and not C_{JM}.

As a result, the problem reduces to solving the radial equations (6.31). It follows that

$$f_{\vartheta\varphi} = \sin\vartheta\sum_{J,M}J(J+1)R_{JM}^{(f)}(r)Y_{JM}(\vartheta,\varphi); \tag{6.35}$$

hence

$$\oint\frac{1}{2}f_{ik}dx^i\wedge dx^k = \oint f_{\vartheta\varphi}d\vartheta d\varphi = 0. \tag{6.36}$$

Therefore, the total magnetic flux of $F_{\mu\nu}$, given by (6.22), is the same as for the background:

$$\oint \frac{1}{2} F_{ik} dx^i \wedge dx^k = \frac{2\pi n}{e}, \tag{6.37}$$

but the magnetic field is no longer purely radial and homogeneous on the sphere, since components of f_{ik} show a general dependance on ϑ, φ, while the components $f_{r\vartheta}$, $f_{r\varphi}$ do not vanish.

As we shall see below, the fields $f_{\mu\nu}$ and $Z_{\mu\nu}$ create $|n|-2$ vortices orthogonal to the horizon, forming the black hole corona.

C. Energy minimization

The condensate energy $E_w + E_{fZ\phi}$ should be minimized with respect to the coefficients $c_{\rm m}$. Since computing the $E_{fZ\phi}$ term requires additional effort, we leave this for future work and focus only on minimizing E_w. Already, this gives the expected result: a lattice of vortices on the horizon, forming the electroweak corona.

This suggests that the minima of E_w coincide with those of $E_w + E_{fZ\phi}$ or close to them. Although we cannot immediately prove this, it seems natural that the E_w term should be dominant because it contains only w_μ, which is the leading correction to the background configuration, while $E_{fZ\phi}$ contains contributions from the subleading second-order corrections for the f, Z, ϕ fields.

Therefore, we minimize

$$\langle |w_\mu|^4 \rangle \equiv \int |w_\mu|^4 \sqrt{-g} d^3x, \tag{6.38}$$

while keeping the norm fixed:

$$\langle |w_\mu|^2 \rangle \equiv \int |w_\mu|^2 \sqrt{-g} d^3x = \text{const}. \tag{6.39}$$

This is equivalent to minimizing

$$E_w = \text{const} \times \langle |w_\mu|^4 \rangle + \text{const} \times \langle |w_\mu|^2 \rangle. \tag{6.40}$$

Using (6.14), one finds that $\langle |w_\mu|^2 \rangle = \text{const.} \times E_2$ with

$$E_2 = \sum_{\mathrm{m} \in [-j,j]} A_{\mathrm{j,m}} c_{\mathrm{m}}^2, \tag{6.41}$$

where

$$\begin{aligned} A_{\mathrm{j,m}} &= \int_0^\pi (\sin\vartheta)^{2j+1} \left(\tan\frac{\vartheta}{2}\right)^{2\mathrm{m}} d\vartheta \\ &= 2^{2j+1} \frac{\Gamma(j+1+\mathrm{m})\Gamma(j+1-\mathrm{m})}{\Gamma(2j+2)}. \end{aligned} \tag{6.42}$$

Similarly, after some algebra, one finds that $\langle |w_\mu|^4 \rangle = \text{const} \times E_4$ with

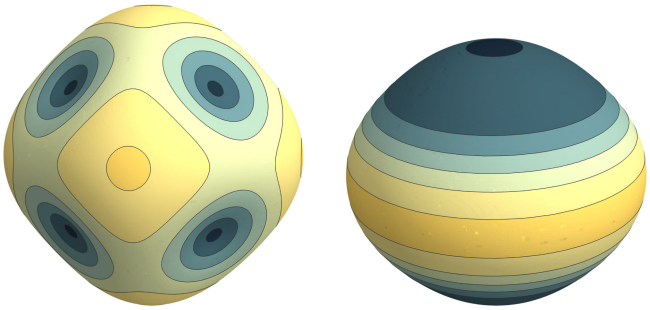


FIG. 6. Left: the horizon distribution of the W condensate $\bar{w}^\mu w_\mu$ minimizing the energy for $n = 10$. The level lines coincide with the current flow, forming loops around vortices that start at the horizon in the radial direction (dark spots). The current flows in the opposite direction around the yellow regions, where the condensate is maximal and where the vortices return to the horizon. Right: the same distribution when all vortices merge into two oppositely directed multivortices.

$$E_4 = \sum_{\mathrm{k,m,l}} A_{2j,\mathrm{k+l}} c_{\mathrm{m}} c_{\mathrm{k}} c_{\mathrm{l}} c_{\mathrm{k+l-m}}, \tag{6.43}$$

where it is assumed that $c_{\rm m} = 0$ if $|m| > j$.

Therefore, omitting constant factors, the problem reduces to the minimization of

$$E_c = E_4 + \mu(E_2 - 1), \tag{6.44}$$

with respect to $c_{\rm m}$, where μ is the Lagrange multiplier, and with E_2 and E_4 expressed by Eqs. (6.41) and (6.43).

Assuming, for example, that $n = 10$, hence $j = 4$ and $m = -4, -3, \ldots 4$, there are nine coefficients $c_{\rm m}$ to find. Their values corresponding to the absolute minimum of E_c determine the function $|w_\mu|^2$ in (6.14), whose horizon profile is shown in Fig. 6 (left panel). The figure shows the level lines, which coincide with the flow lines of the current J^μ.

As seen in Fig. 6, the flow lines form loops. A loop of current generates a magnetic field in the orthogonal direction, so the loops in Fig. 6 encircle radially directed vortices located at the points where the condensate $|w_\mu|^2$ vanishes [dark spots]. There are four vortices on the visible side of the surface in Fig. 6 (left panel), and the same number on the other side, so altogether there are eight vortices [$8 = |n| - 2$] homogeneously distributed over the horizon. The condensate exhibits, in this case, the same discrete symmetries as an octahedron.

The difference $|n| - 2$ arises because, for $|n| = 2$, the black hole is spherically symmetric, and the condensate produces no currents, meaning there are no vortices. We checked that minimization of (6.44) gives one vortex for $n = 3$, two vortices for $n = 4$, and so on. These vortices repel each other and form a lattice on the horizon such that their mutual separations are maximal. These solutions correspond to the global energy minimum.

The vortices start at the horizon where the condensate $|w_\mu|^2$ vanishes [dark spots in Fig. 6], but, as we shall now see, they eventually return to the horizon in the regions where the condensate $|w_\mu|^2$ is maximal [yellow spots in Fig. 6].

D. Structure of vortices

The vortices carry nonzero magnetic and Z fluxes, but their net flux through the horizon is zero. Therefore, they start at the horizon and then return, being attached to the horizon at both ends, similarly to the coronal loops in the Sun's atmosphere.

The vortices leave the horizon in the dark regions, which are encircled by an electric current flowing in the anticlockwise direction [for $n > 0$]. They return back in the yellow regions, where the current flows in a clockwise direction. The fluxes through the dark and yellow regions mutually compensate, as can be seen as follows.

One notices that the term containing the derivatives in the radial equation (6.31) vanishes at the horizon because the first derivative of $R^{(f)}_{JM}(r)$ vanishes there due to the boundary conditions. This means that $f_{r\vartheta} = f_{r\varphi} = 0$ at the horizon.

Equation (6.31) then implies that for $J > 0$, one has $J(J+1)R^{(f)}_{JM}(r_h) = e\psi^2(r_h)C_{JM}$. Injecting this into (6.35) (where $J > 0$) and using (6.29), yields the horizon value of the magnetic field,

$$f_{\vartheta\varphi} = e\psi^2(r_h)\sin\vartheta \sum_{J>0,M} C_{JM}Y_{JM}(\vartheta,\varphi) = e\psi^2(r_h)\sin\vartheta\{\Theta(\vartheta,\varphi) - C_{00}Y_{00}\}, \tag{6.45}$$

where $C_{00} = \oint \Theta(\vartheta,\varphi)Y_{00}d^2\Omega$ with $d^2\Omega = \sin\vartheta d\vartheta d\varphi$.

Therefore, the condensate creates a magnetic field that is purely radial at the horizon:

$$\delta\mathcal{B}^r = \frac{\epsilon^{r\vartheta\varphi}}{\sqrt{-g}}f_{\vartheta\varphi} = \frac{n}{|n|}\times\frac{e}{2}\left(|w_\mu|^2 - \frac{1}{4\pi}\oint |w_\mu|^2 d^2\Omega\right), \tag{6.46}$$

where we have used Eq. (6.14) and restored the dependence on the sign of n.

The total flux of $\delta\mathcal{B}^r$ through the horizon is zero, but locally this field is nonzero. Specifically, $\delta\mathcal{B}^r > 0$ where the condensate density $|w_\mu|^2$ is large, which results in the enhancement of the background magnetic field $\mathcal{B}^r = n/(2er_h^2)$. On the other hand, $\delta\mathcal{B}^r < 0$ near the vortex centers where $|w_\mu|^2 = 0$, leading to the weakening of the background field. This phenomenon corresponds to the *antiscreening* property of the condensate [47,48]; see Appendix C.

Therefore, the sign of $\delta\mathcal{B}^r$ is determined by the value of the condensate density $|w_\mu|^2$, whose profile is shown in Fig. 6. The vortices leave the horizon in regions marked by dark colors in Fig. 6, where $\delta\mathcal{B}^r < 0$ [for $n > 0$] and carry away a negative magnetic flux. They return to the horizon in the yellow regions, bringing back the same flux.

The total magnetic flux carried by a vortex can be obtained by integrating $\delta\mathcal{B}^r$ over a dark region where it is sign definite. The flux of the massive Z field can be computed similarly and will have an opposite sign, because of the opposite sign of the source term for the Z field in Eq. (6.31).

The magnetic charge density $\sim\epsilon^{ijk}\partial_i\psi_{jk}$ is also maximal in the yellow regions in Fig. 6, together with the condensate density $|w_\mu|^2$. Therefore, these regions are magnetically charged when considered within the Nambu approach. There are eight vortices and six charged yellow regions in Fig. 6 (left panel).

Each vortex center [dark region] is surrounded by three yellow regions. Since none of the latter is favored, each vortex, carrying a negative [for $n > 0$] outgoing magnetic flux, must split into three flux jets flowing toward the three neighboring yellow regions. Each yellow region is surrounded by four vortices and, hence, absorbs incoming jets from four neighboring vortices. Therefore, there are eight vortices splitting into 24 jets, which together form the black hole corona—a rather complicated pattern, whose complexity increases with growing n.

E. Axial symmetry

The axially symmetric configuration with $c_{\rm m} \propto \delta_{\rm m\,0}$ is also a stationary point of the energy (6.44). It can be viewed as a system in which all elementary vortices merge into two oppositely directed multivortices, generated by two oppositely directed azimuthal currents. The system is invariant under $\vartheta \to \pi - \vartheta$, except for the current density, which changes sign.

The condensate $|w_\mu|^2$, the radial magnetic field $F_{\vartheta\varphi}$, and the magnetic charge density $\sim\epsilon^{ijk}\partial_i\psi_{jk}$ attain maximal values at the equator, where the azimuthal current changes sign, as shown in the right panel of Fig. 6 [see also (6.21)].

However, the Hessian matrix has negative eigenvalues in this case, indicating that such solutions are unstable and should decay into nonaxially symmetric configurations. This is because the elementary vortices forming a multivortex repel each other.

Setting $c_{\rm m} = c_0\delta_{\rm m\,0}$ and minimizing the energy yields $c_0 = 1/\sqrt{2}$. Equation (6.14) then implies that

$$\Theta(\vartheta,\varphi) = \frac{1}{2}(\sin\vartheta)^{2j}. \tag{6.47}$$

Inserting this into Eqs. (6.45) and (6.46), we obtain the horizon value of the magnetic field [compare with Eq. (C15) in Appendix C]:

$$\delta\mathcal{B}^r = e\frac{n}{|n|}\frac{\psi^2(r_h)}{2r_h^2}\times\left((\sin\vartheta)^{2j}-\frac{\sqrt{\pi}\Gamma(j+1)}{2\Gamma(j+3/2)}\right), \quad (6.48)$$

where $j=|n|/2-1\geq 0$. This describes two multivortices made of $|n|-2$ elementary vortices: one along the z axis in the northern hemisphere [the dark spot in Fig. 6, right panel], and the other one along the negative direction of the z axis in the southern hemisphere. Each vortex starts at the horizon in the polar region, extends outside, spreads out like a fountain, and then returns back to the horizon in the equatorial region.

F. Special cases

Let us consider the lowest values of n.

1. $|n|=2$

In the case where the condensate is spherically symmetric, the currents vanish, and consequently, there are no vortices. This leads to $\delta\mathcal{B}^r=0$ [see Eq. (6.48) with $j=0$], meaning the magnetic field is purely radial and homogeneous on the sphere.

The energy E_c in (6.44) depends only on one coefficient c_0, and the minimization yields a unique solution: $c_0=1/\sqrt{2}$, corresponding to the global minimum.

Thus, it is plausible that nonperturbative generalizations of this solution—the hairy black holes with $|n|=2$—are stable, as discussed in Sec. V D.

2. $|n|=4$

If we do not assume the axial symmetry, the condensate corresponding to the global energy minimum would be determined by three coefficients $c_0, c_{\pm 1}$. However, having obtained these coefficients by minimizing the energy, they can be transformed to $c_{\rm m}\propto\delta_{\rm m\,0}$ by a global rotation. This means that the global minimum remains axially symmetric.

In this case, there are $|n|-2=2$ elementary vortices, which position themselves at opposite sides of the sphere due to their mutual repulsion. Since this perturbative solution is stable, it is plausible that its nonperturbative generalizations—the hairy black holes with $|n|=4$—would also be stable. These solutions will be explored in Sec. VIII.

3. $|n|=3$

In this case there are two axially symmetric solutions. The first solution contains a single vortex along the positive z axis, say. This solution it is not invariant under $\vartheta\to\pi-\vartheta$, since it has a preferred direction for the vortex. Consequently, it must support a nonzero dipole moment. Despite this, it represents the global minimum of the energy.

The second solution is invariant under $\vartheta\to\pi-\vartheta$, and it contains two oppositely directed half vortices. While this solution is symmetric, it is energetically less favorable than the first one and does not correspond to the global energy minimum.

Therefore, the first solution is less symmetric but stable, while the second one is more symmetric but less stable.

G. Conclusion of the perturbative analysis

Summarizing the above discussion, minimum-energy hairy solutions with higher magnetic charge $|n|$ can have at most only discrete symmetries. As a result, constructing them at the nonperturbative level would require full 3D numerical simulations. However, in the special case of axial symmetry, the magnetic charge can take arbitrary values, but the complexity of the problem is reduced. In this case, only 2D simulations are needed, although they do not necessarily yield the global energy minimum.

Therefore, in what follows, we shall restrict to the axially symmetric sector.

VII. AXIAL SYMMETRY

Choosing the spacetime coordinates as $x^\mu=(t,\mathrm{r},\vartheta,\varphi)$, we assume the invariance under the action of two symmetry generators:

$$\imath=\frac{\partial}{\partial t}, \qquad \varsigma=\frac{\partial}{\partial\varphi}, \quad (7.1)$$

where the timelike Killing vector $\imath$ is assumed to be hypersurface orthogonal. Additionally, we impose invariance under reflections across the equatorial plane, $\vartheta\to\pi-\vartheta$.

A. Static and axially symmetric gravitational fields

The line element is parametrized as

$$ds^2=-e^{2\mathrm{U}}\mathrm{N}(\mathrm{r})dt^2+e^{-2\mathrm{U}}dl^2,$$
$$dl^2=e^{2\mathrm{K}}\left[\frac{d\mathrm{r}^2}{\mathrm{N}(\mathrm{r})}+\mathrm{r}^2d\vartheta^2\right]+e^{2\mathrm{S}}\mathrm{r}^2\sin^2\vartheta d\varphi^2, \quad (7.2)$$

where U, K, S depend on r, ϑ and N(r) is an auxiliary function. It is important to note that the radial coordinate r is not the same as the Schwarzschild coordinate r used in previous sections. The radial coordinate is defined up to diffeomorphisms $\mathrm{r}\to\tilde{\mathrm{r}}=\tilde{\mathrm{r}}(\mathrm{r})$, which lead to the transformations $\mathrm{U}\to\tilde{\mathrm{U}}$, $\mathrm{N}\to\tilde{\mathrm{N}}$, $\mathrm{K}\to\tilde{\mathrm{K}}$, $\mathrm{S}\to\tilde{\mathrm{S}}$, where

$$\frac{d\mathrm{r}}{\mathrm{r}\sqrt{\mathrm{N}}}=\frac{d\tilde{\mathrm{r}}}{\tilde{\mathrm{r}}\sqrt{\tilde{\mathrm{N}}}}, \qquad e^{\mathrm{U}}\sqrt{\mathrm{N}}=e^{\tilde{\mathrm{U}}}\sqrt{\tilde{\mathrm{N}}}, \quad (7.3)$$

$$\mathrm{r}\sqrt{\mathrm{N}}e^{\mathrm{K}}=\tilde{\mathrm{r}}\sqrt{\tilde{\mathrm{N}}}\,e^{\tilde{\mathrm{K}}}, \qquad \mathrm{r}\sqrt{\mathrm{N}}e^{\mathrm{S}}=\tilde{\mathrm{r}}\sqrt{\tilde{\mathrm{N}}}\,e^{\tilde{\mathrm{S}}}. \quad (7.4)$$

This gauge freedom can be fixed by choosing a specific form for the auxiliary function N(r). For example, one can set N(r) = 1.

However, even after fixing the radial coordinate r, the line element still admits a large gauge symmetry. Indeed, if N(r) = 1, then the r, ϑ part of the metric can be represented as

$$e^{2K-2U}(dr^2 + r^2 d\vartheta^2) = e^{2K-2U}|d\varpi|^2, \tag{7.5}$$

where the complex variable is $\varpi = re^{i\vartheta}$. Rewriting this in terms of a new complex variable $\tilde{\varpi}$ such that $\varpi = \varpi(\tilde{\varpi})$, the line element retains the same structure, up to the replacement

$$K \to \tilde{K} = K + \ln\left|\frac{d\varpi}{d\tilde{\varpi}}\right|. \tag{7.6}$$

This reveals that the r, ϑ sector of the geometry enjoys a conformal symmetry generated by holomorphic functions $\varpi(\tilde{\varpi})$. However, it turns out that this symmetry is ultimately fixed by the boundary conditions given in Eq. (7.7) below, which permit only the identity transformation $\varpi = \tilde{\varpi}$.

For nonextremal black hole solutions we choose $N(r) = 1 - r_H/r$, where $r = r_H$ corresponds to the position of the event horizon. To ensure that the geometry is asymptotically flat and regular outside the event horizon, we impose the following boundary conditions:

$$\begin{aligned}
&\text{infinity,} && r = \infty\colon\ U = K = S = 0;\\
&\text{horizon,} && r = r_H\colon\ |\partial_r U| < \infty, \quad |\partial_r K| < \infty, \quad |\partial_r S| < \infty;\\
&\text{symmetry axis,} && \vartheta = 0, \pi\colon\ \partial_\vartheta U = \partial_\vartheta K = \partial_\vartheta S = 0;\\
&\text{equator,} && \vartheta = \pi/2\colon\ \partial_\vartheta U = \partial_\vartheta K = \partial_\vartheta S = 0.
\end{aligned} \tag{7.7}$$

It turns out that imposing these conditions automatically ensures that at the symmetry axis one has

$$\vartheta = 0, \pi\colon\ K = S, \tag{7.8}$$

which is needed for the absence of the conical singularity.

The functions U, K, S satisfy second-order differential equations, which are obtained by taking suitable linear combinations of the Einstein equations (2.19):

$$\left(\frac{1}{2}e^{S-2U}r^2(Ne^{2U})'_r \sin\vartheta\right)'_r + (e^S U'_\vartheta \sin\vartheta)'_\vartheta = -\kappa\left(T^0{}_0 - \frac{1}{2}T\right)\sqrt{-g}, \tag{7.9a}$$

$$(r\sqrt{N}(r\sqrt{N}e^S)'_r \sin\vartheta)'_r + (e^S \sin\vartheta)''_{\vartheta\vartheta} = \kappa(T^r{}_r + T^\vartheta{}_\vartheta)\sqrt{-g}, \tag{7.9b}$$

$$r\sqrt{N}(r\sqrt{N}K'_r)'_r + K''_{\vartheta\vartheta} + Nr^2(U'_r)^2 + (U'_\vartheta)^2 + r^2 N' U'_r + \frac{1}{2}(r^2 N'_r)'_r = r^2 e^{2K-2U}\kappa T^\varphi{}_\varphi, \tag{7.9c}$$

with $T = T^\mu{}_\mu$. At large distances, where the theory reduces to Einstein-Maxwell, one has $T^r_r + T^\vartheta_\vartheta = 0$, which allows for an exact integration of the S equation (7.9b). The solution which remains bounded for any ϑ is given by

$$r\sqrt{N}e^S = A_1 e^\xi + A_2 e^{-\xi} \quad \text{with} \quad \xi = \int \frac{dr}{r\sqrt{N}}. \tag{7.10}$$

The integration constants A_1, A_2 can be adjusted to ensure that $S \to 0$ as $r \to \infty$. At shorter distances, where $T^r_r + T^\vartheta_\vartheta \neq 0$, the solution can no longer be obtained analytically. Instead, the S equation must be solved numerically together with the other field equations in (7.9).

Among the remaining Einstein equations (2.19), there are also constraints

$$\mathcal{C}_1 \equiv r\sqrt{-g}(G^r{}_r - \kappa T^r{}_r) = 0, \quad \mathcal{C}_2 \equiv \frac{\sqrt{-g}}{r}(G^r{}_\vartheta - \kappa T^r{}_\vartheta) = 0, \tag{7.11}$$

which do not involve second derivatives of U, K, but only those of S. These equations can be solved for $\partial_r K$ and $\partial_\vartheta K$, giving

$$\partial_r K = \mathcal{K}_1, \qquad \partial_\vartheta K = \mathcal{K}_2, \tag{7.12}$$

where $\mathcal{K}_1$, $\mathcal{K}_2$ are functions that do not depend on K. The function K can be obtained by integrating these two equations, as in the vacuum case [71], provided that the compatibility condition,

$$\partial_\vartheta \mathcal{K}_1 = \partial_{\rm r} \mathcal{K}_2, \tag{7.13}$$

is satisfied. This condition follows from Eqs. (7.9a) and (7.9b), while Eq. (7.9c) is automatically fulfilled as a consequence of (7.12).

In practice, however, it is preferable to treat the two Eq. (7.11) as constraints rather than solving them explicitly. Specifically, the two nontrivial Bianchi identities $\nabla_\mu(G^\mu{}_\nu - \kappa T^\mu{}_\nu) = 0$ for $\nu = {\rm r}, \vartheta$ can be rewritten as

$$\partial_\vartheta \mathcal{C}_2 = -{\rm N}\partial_{\rm r}\mathcal{C}_1 - \frac{1}{2}{\rm N}'\mathcal{C}_1 + \ldots, \quad \partial_\vartheta \mathcal{C}_1 = {\rm r}^2\partial_{\rm r}\mathcal{C}_2 + {\rm r}\mathcal{C}_2 + \ldots, \tag{7.14}$$

where the dots denote terms that vanish if the second-order equations (7.9) are satisfied. It follows that if the constraints $\mathcal{C}_1 = 0, \mathcal{C}_2 = 0$ hold at the symmetry axis, then they will be satisfied everywhere. At the symmetry axis, we have

$$\vartheta = 0, \pi\colon\ \mathcal{C}_1 = -{\rm r}e^{\rm S}\partial_\vartheta({\rm K} - 2{\rm S}), \qquad \mathcal{C}_2 = {\rm r}{\rm N}e^{\rm S}\partial_{\rm r}({\rm K} - {\rm S}), \tag{7.15}$$

which vanish owing to the boundary conditions (7.7). Thus, by solving the three second-order equations (7.9) with the boundary conditions (7.7), the two constraint equations (7.11) are automatically satisfied.

B. The integral formula for the ADM mass

The ADM mass M in (2.23) can be expressed as a surface integral over a sphere at spatial infinity, following Komar [72]:

$$M = -\frac{1}{8\pi}\oint_{S^2_\infty} \star d(\imath_\mu dx^\mu). \tag{7.16}$$

Here $\imath_\mu$ are the covariant components of the timelike Killing vector, and the star denotes the four-dimensional Hodge dual. Using Gauss's theorem, the surface integral at infinity can be transformed into a volume integral over the three space, plus a surface integral over the event horizon. This gives

$$M = \frac{{\rm k_H A_H}}{4\pi} + \frac{1}{4\pi}\int_{\rm r>r_H} R_{\hat{0}\hat{0}}\sqrt{-{\rm g}}\, d^3x. \tag{7.17}$$

The first term represents the contribution from the event horizon, where $\rm k_H$ is the surface gravity and $\rm A_H$ is the horizon area. In the second term one has $R_{\hat{0}\hat{0}} = R_{\mu\nu}\imath^\mu\imath^\nu/|\imath^\alpha\imath_\alpha| = -R^0{}_0$. The surface gravity is expressed by

$${\rm k_H^2} = -\frac{1}{2}\nabla^\mu \imath_\nu \nabla_\mu \imath^\nu\Big|_{\rm r=r_H}. \tag{7.18}$$

Using the line element (7.2), one obtains

$${\rm k_H} = \frac{{\rm N}'}{2}e^{2{\rm U}-{\rm K}}\Big|_{\rm r=r_H}, \quad {\rm A_H} = 2\pi {\rm r_H^2}\int_0^\pi e^{{\rm K}-2{\rm U}+{\rm S}}\sin\vartheta d\vartheta\Big|_{\rm r=r_H}. \tag{7.19}$$

The surface gravity should be constant at the horizon, which follows from the second constraint equation in (7.12). At $\rm r = r_H$, where $\rm N = 0$, this equation simplifies to

$$\partial_\vartheta {\rm K}|_{\rm r=r_H} = 2\partial_\vartheta {\rm U}|_{\rm r=r_H} \Rightarrow \partial_\vartheta(2{\rm U} - {\rm K})|_{\rm r=r_H} = 0. \tag{7.20}$$

Thus, 2U–K is independent of ϑ at the horizon, ensuring that $\rm k_H$ remains constant.

The mass formula (7.17) can be easily verified since $R_{\hat{0}\hat{0}}\sqrt{-{\rm g}}$ corresponds to the right-hand side of Eq. (7.9). Therefore, replacing it by the left-hand side of the same equation, integrating, and using the boundary condition (7.7) yield

$$\begin{aligned}\frac{1}{4\pi}\int_{\rm r>r_H} R_{\hat{0}\hat{0}}\sqrt{-{\rm g}}\, d^3x &= \frac{1}{4\pi}\int_0^{2\pi} d\varphi \int_0^\pi \frac{1}{2} e^{\rm S-2U}{\rm r}^2({\rm N}e^{2\rm U})'_{\rm r}\sin\vartheta d\vartheta\Big|_{\rm r=r_H}^{\rm r=\infty} \\ &= M - \frac{1}{4\pi}\frac{{\rm N}'({\rm r_H})}{2}{\rm r_H^2}\int_0^{2\pi} d\varphi\int_0^\pi e^{\rm S}\sin\vartheta d\vartheta\Big|_{\rm r=r_H} = M - \frac{{\rm k_H A_H}}{4\pi}.\end{aligned} \tag{7.21}$$

Here we used the fact that at large r, one has $\rm S, U \to 0$ and ${\rm N}e^{2\rm U} = 1 - 2M/{\rm r} + \mathcal{O}(1/{\rm r}^2)$, along with the condition that 2U–K remains constant at the horizon.

C. Axially symmetric electroweak fields

Since the two Killing vectors in Eq. (7.1) commute with each other, there is a gauge where the fields do not depend on t, φ. Additionally, we require the electroweak fields to be purely magnetic and their energy density to be invariant under reflections across the equatorial plane, $\vartheta \to \pi - \vartheta$. We choose the fields as follows:

$${\rm W} = {\rm T}_2(F_1 d{\rm r} + F_2 d\vartheta) + \nu({\rm T}_3 F_3 - {\rm T}_1 F_4)d\varphi, \qquad B = \nu Y d\varphi, \qquad \Phi = \begin{pmatrix}\phi_1\\ \phi_2\end{pmatrix}, \tag{7.22}$$

where $F_1, F_2, F_3, F_4, Y, \phi_1, \phi_2$ are seven real valued functions of r, ϑ, and the constant is given by

$$\nu = -n/2, \qquad n \in \mathbb{Z}. \tag{7.23}$$

This is the same condition as in (3.3), and it will be justified shortly.

The SU(2) gauge field in (7.22) corresponds to the static and purely magnetic ansatz of Rebbi and Rossi [73]. The fields (7.22) retain their form under gauge transformations (2.15) generated by $\mathfrak{V} = \exp\{i\chi(\mathrm{r},\vartheta)\mathrm{T}_2\}$, whose effect is

$$\begin{aligned}
&F_1 \to F_1 + \partial_{\mathrm{r}}\chi, \quad F_2 \to F_2 + \partial_\vartheta\chi, \quad Y \to Y,\\
&F_3 \to F_3\cos\chi - F_4\sin\chi, \quad F_4 \to F_4\cos\chi + F_3\sin\chi,\\
&\phi_1 \to \phi_1\cos(\chi/2) + \phi_2\sin(\chi/2),\\
&\phi_2 \to \phi_2\cos(\chi/2) - \phi_1\sin(\chi/2).
\end{aligned} \tag{7.24}$$

Injecting (7.2) and (7.22) into (2.20) yields components of the energy-momentum tensor $T_{\mu\nu}$, shown in Appendix A. Injecting into (2.26) and (2.41) yields $\mathcal{J}^\varphi$ and J^φ as the only nonzero components of the electric currents. Hence, the currents are purely azimuthal. Injecting into (2.43) yields only one nontrivial component of the magnetic current, corresponding to the magnetic charge density $\tilde{\mathcal{J}}^0$. The energy-momentum tensor and the currents are gauge invariant.

Modulo gauge transformations (7.24), the zero energy configuration is

$$\begin{aligned}
&F_1 = F_2 = F_4 = \phi_1 = 0, \qquad \phi_2 = 1,\\
&F_3 = Y = \mathrm{const} \equiv Y_\infty,
\end{aligned} \tag{7.25}$$

which retains its form under gauge transformations generated by $\mathfrak{V} = \exp\{i\mathcal{C}\nu\varphi(1+\tau_3)/2\}$ with a constant $\mathcal{C}$, whose effect is $Y_\infty \to Y_\infty + \mathcal{C}$.

The electroweak Lagrangian is

$$\begin{aligned}
L_{\mathrm{WS}} &= \int \mathcal{L}_{\mathrm{WS}}\sqrt{-\mathrm{g}}d^3x = \int T^0{}_0\sqrt{-\mathrm{g}}d^3x\\
&= -2\pi\int(a_1 + a_2 + a_3 + a_4 + a_5)d\mathrm{r}d\vartheta,
\end{aligned} \tag{7.26}$$

where $a_1, \ldots, a_5$ are given by (A2) in Appendix A. Varying the Lagrangian with respect to the seven amplitudes $F_1, F_2, F_3, F_4, Y, \phi_1, \phi_2$ yields the electroweak equations. Together with the Einstein equations (7.9), this gives a closed system of ten second-order partial differential equations, whose solutions describe static, axially symmetric, and purely magnetic EWS fields. Before solving these equations, some preliminary work remains to be done.

D. Removing the string singularity

The gauge fields in (7.22) contain the Dirac string singularity at the symmetry axis because their φ components do not vanish there. This singularity can be removed by setting

$$\begin{aligned}
&F_1 = -\frac{H_1(\mathrm{r},\vartheta)}{\mathrm{r}\sqrt{\mathrm{N}}}, \qquad F_2 = H_2(\mathrm{r},\vartheta), \qquad F_3 = \cos\vartheta + H_3(\mathrm{r},\vartheta)\sin\vartheta,\\
&F_4 = H_4(\mathrm{r},\vartheta)\sin\vartheta, \qquad Y = \cos\vartheta + y(\mathrm{r},\vartheta)\sin\vartheta,
\end{aligned} \tag{7.27}$$

and then performing the gauge transformation generated by

$$\mathfrak{V}_\pm = e^{-i\nu\varphi\mathrm{T}_3}e^{-i\vartheta\mathrm{T}_2}e^{\pm i\nu\varphi/2}, \tag{7.28}$$

which brings the SU(2) field to the form

$$\mathrm{W} = \mathrm{T}_\varphi\left(-\frac{H_1}{\mathrm{r}\sqrt{\mathrm{N}}}d\mathrm{r} + (H_2 - 1)d\vartheta\right) + \nu(\mathrm{T}_r H_3 + \mathrm{T}_\vartheta(1 - H_4))\sin\vartheta d\varphi, \tag{7.29}$$

where the angle-dependent SU(2) generators are $\mathrm{T}_r = e^a_r\mathrm{T}_a$, $\mathrm{T}_\vartheta = e^a_\vartheta\mathrm{T}_a$, $\mathrm{T}_\varphi = e^a_\varphi\mathrm{T}_a$ with

$$e^a_r = (\sin\vartheta\cos(\nu\varphi), \sin\vartheta\sin(\nu\varphi), \cos\vartheta), \qquad e^a_\vartheta = \partial_\vartheta e^a_r, \qquad e^a_\varphi = \frac{1}{\nu\sin\vartheta}\partial_\varphi e^a_r. \tag{7.30}$$

This field is φ dependent but regular at the symmetry axis, owing to the boundary conditions defined in Eq. (7.35) below (see Ref. [59] for details). The U(1) and Higgs fields become

$$\begin{aligned}
B_\pm &= \nu(\cos\vartheta \pm 1 + y\sin\vartheta)d\varphi,\\
\Phi_\pm &= e^{\pm i\nu\varphi/2}\begin{pmatrix}(\phi_1\cos(\vartheta/2) - \phi_2\sin(\vartheta/2))e^{-i\nu\varphi/2}\\ (\phi_1\sin(\vartheta/2) + \phi_2\cos(\vartheta/2))e^{+i\nu\varphi/2}\end{pmatrix},
\end{aligned} \tag{7.31}$$

where the upper "+" and lower "−" signs correspond to two local gauges used, respectively, in the southern and northern hemispheres. These two gauges are related to each other in the equatorial region by the U(1) transformation with $\mathfrak{V} = \exp(i\nu\varphi)$. When expressed in these two local gauges, the U(1) and Higgs fields are everywhere regular.

The above formulas suggest that $\nu = -n/2$ should be an integer. However, it can be a half-integer as well. In that case, the φ-dependent part of T_r changes sign under $\varphi \to \varphi + 2\pi$, but the correct sign can be restored by the global gauge transformation generated by $\mathfrak{V} = \tau_3$ or $\mathfrak{V} = -\tau_3$, whose effect is

$$\mathrm{T}_1 \to -\mathrm{T}_1, \qquad \mathrm{T}_2 \to -\mathrm{T}_2, \tag{7.32}$$

so that the field (7.29) does not change. Similarly, if ν is a half integer, then the lower component of Φ_+ and the upper component of Φ_- change sign under $\varphi \to \varphi + 2\pi$, but the correct sign can be restored by the gauge transformations generated by $\mathfrak{V} = \tau_3$ and $\mathfrak{V} = -\tau_3$, respectively. The fields (7.31) then remain invariant. As a result, all integer values of n in (7.23) are allowed.

To summarize, by passing to the parametrization in terms of the seven amplitudes H_1, H_2, H_3, H_4, y, ϕ_1, and ϕ_2, subject to the boundary conditions to be specified below, the electroweak fields become regular at the symmetry axis.

E. Fixing the gauge

The equations for $H_1, H_2, H_3, H_4, y, \phi_1$, and ϕ_2 admit pure gauge solutions due to the residual gauge invariance (7.24). Such zero modes should be removed by fixing the gauge, as otherwise the differential operators in the equations are not invertible. The gauge can be fixed by setting to zero the covariant divergence of the two vector $F_1 dr + F_2 d\vartheta$ in (7.22), computed with respect to the r, ϑ part of the metric. This requires that

$$\mathrm{r}\sqrt{\mathrm{N}}\partial_{\mathrm{r}} H_1 = \partial_\vartheta H_2 \Rightarrow \partial_\xi H_1 = \partial_\vartheta H_2, \quad \text{where } \xi = \int_{r_H}^{\mathrm{r}} \frac{d\mathrm{r}}{\mathrm{r}\sqrt{\mathrm{N}}}. \tag{7.33}$$

This gauge condition insures good numerical convergence, although it gives rise to a spurious long-range mode in the solutions at large r [59]. The condition (7.33) still allows for residual gauge transformations (7.24) with the gauge parameter χ subject to

$$(\partial^2_{\xi\xi} + \partial^2_{\vartheta\vartheta})\chi = 0. \tag{7.34}$$

Since $\xi \in [0, \infty)$, $\vartheta \in [0, \pi]$, this equation possesses bounded solutions which generate gauge transformations $H_1 \to H_1 - \partial_\xi \chi$ and $H_2 \to H_2 + \partial_\vartheta \chi$. At the same time, as seen in (7.27), H_1 must vanish at the horizon where $\xi = 0$ since otherwise the gauge field amplitude F_1 diverges. As a result, the only allowed solution of (7.34) is $\chi = \text{const}$, but this is also ruled out since otherwise the value of the Higgs field components would change according to (7.24), whereas we impose at infinity $\phi_1 = 0$ and $\phi_2 = 1$.

Therefore, the gauge is completely fixed by the condition (7.33). Using this condition, all equations assume a manifestly elliptic form.

F. Boundary conditions and numerical procedure

The axially symmetric EWS fields are the line element in (7.2) and the electroweak fields in (7.29) and (7.31) expressed in terms of ten functions, $\mathrm{U}, \mathrm{K}, \mathrm{S}, H_1, H_2, H_3, H_4, y, \phi_1, \phi_2$ which satisfy ten elliptic equations. Solutions of these equations also satisfy the gravitational constraints (7.11) owing to the boundary conditions described by Eq. (7.35) below.

We use the compact radial variable $\mathrm{x} \in [0, 1]$ such that

$$\mathrm{r} = \sqrt{\mathrm{r}_{\mathrm{H}}^2 + \mathrm{x}^2/(1-\mathrm{x})^2},$$

and since we assume reflection invariance of the energy density under $\vartheta \to \pi - \vartheta$, we can restrict the range of the angular variable to $\vartheta \in [0, \pi/2]$. This assumption implies that U, K, S, H_2, H_4, and ϕ_2 remain invariant under $\vartheta \to \pi - \vartheta$, while H_1, H_3, y, and ϕ_1 change sign (see Ref. [59] for details). Regularity at the horizon and along the symmetry axis, together with asymptotic flatness, then imposes the following boundary conditions:

$$\begin{aligned}
&\text{axis, } \vartheta = 0\text{: } \partial_\vartheta = 0 \quad \text{for} \quad \mathrm{U}, \mathrm{S}, H_2, H_4, \phi_2;\\
&\qquad \mathrm{K} - \mathrm{S} = H_1 = H_3 = y = \phi_1 = 0;\\
&\text{equator, } \vartheta = \pi/2\text{: } \partial_\vartheta = 0 \quad \text{for} \quad \mathrm{U}, \mathrm{K}, \mathrm{S}, H_2, H_4, \phi_2;\\
&\qquad H_1 = H_3 = y = \phi_1 = 0;\\
&\text{horizon, } \mathrm{x} = 0\text{: } H_1 = 0\text{: } \partial_{\mathrm{x}} = 0 \text{ for the rest;}\\
&\text{infinity, } \mathrm{x} = 1\text{: } \phi_2 = 1;\ 0 \text{ for the rest.}
\end{aligned} \tag{7.35}$$

It turns out that these boundary conditions automatically ensure that at the symmetry axis one has

$$\vartheta = 0\text{: } H_2 = H_4, \qquad \partial_\vartheta \mathrm{K} = 0, \tag{7.36}$$

as needed for the regularity.

We solve the field equations with these boundary conditions to determine the components of the "state vector"

$$\Psi = [H_1, H_2, H_3, H_4, y, \phi_1, \phi_2, \mathrm{U}, \mathrm{K}, \mathrm{S}], \tag{7.37}$$

which are functions of r, ϑ. We solve the equations with the FreeFem numerical solver based on the finite element method [74]. This solver uses the weak form of differential equations obtained by transforming them into integral

equations, and the functions to be determined are expanded over elementary basis functions obtained by triangulating the integration domain. To handle the nonlinearities, we use the Newton-Raphson algorithm. To estimate the numerical accuracy of the solutions, we use the virial relation that should hold on shell.

G. Virial relations

Consider the one form generating a spatial dilatation,

$$\zeta_\mu dx^\mu = \mathrm{r}e^{\mathrm{K-U}}d\mathrm{r}. \tag{7.38}$$

The tensor $\nabla_\mu\zeta_\nu + \nabla_\nu\zeta_\mu$ is diagonal and describes the variation of the spacetime metric induced by the dilatation. The virial relation can be expressed in terms of $\zeta^\mu = \mathrm{g}^{\mu\nu}\zeta_\nu$:

$$v_m \equiv \int_{\mathrm{r}>\mathrm{r_H}} T^\mu{}_\nu \nabla_\mu \zeta^\nu \sqrt{-\mathrm{g}} d^3x = 0. \tag{7.39}$$

Since $T^\mu{}_\nu\nabla_\mu\zeta^\nu = \nabla_\mu(T^\mu_\nu\zeta^\nu) - (\nabla_\mu T^\mu{}_\nu)\zeta^\nu$ and the energy-momentum tensor is conserved, the volume integral can be transformed to surface integrals over a two-sphere at infinity and over the horizon,

$$v_m = \oint_{\mathrm{r}\to\infty} T^\mu{}_\nu \zeta^\nu d^2S_\mu - \oint_{\mathrm{r}=\mathrm{r_H}} T^\mu{}_\nu\zeta^\nu d^2S_\mu. \tag{7.40}$$

As T^μ_ν is bounded for $\mathrm{r} \geq \mathrm{r_H}$ and approaches zero at infinity, the surface integral at infinity vanishes, while the integral over the horizon is zero because $\zeta^\nu \sim \mathrm{N}$. As a result, the integral in (7.39) vanishes, although its integrand does not.

It is instructive to see what happens in the spherically symmetric case when the metric reduces to (3.1), while the energy-momentum tensor is diagonal, so that we have $T^\mu{}_\nu = \mathrm{diag}[T^0{}_0(r), T^r{}_r(r), T^\vartheta{}_\vartheta(r), T^\varphi{}_\varphi(r)]$. This can correspond to any matter type, not only to the electroweak fields. The virial relation (7.39) reduces to

$$v_m = 4\pi\int_{r_H}^\infty \sigma r^2\left(NT^k{}_k + \frac{rN'}{2}T^r{}_r + \frac{r}{2\sigma^2}(\sigma^2N)'T^0{}_0\right)dr = 0, \tag{7.41}$$

where $T^k{}_k = T^r{}_r + T^\vartheta{}_\vartheta + T^\varphi{}_\varphi$ is the sum of the principal pressures. Taking into account the conservation condition $\nabla_\mu T^\mu{}_\nu = 0$, it is not difficult to see that this is equivalent to

$$v_m = 4\pi\int_{r_H}^\infty (r^3\sigma N T^r{}_r)'dr = 0, \tag{7.42}$$

which indeed holds, since at the lower limit N vanishes, while for $r\to\infty$, the components $T^\mu{}_\nu$ decay faster than $1/r^3$ (otherwise the energy would diverge).

In flat space, where $N = \sigma = 1$, Eq. (7.41) reduces to

$$v_\mathrm{m} = \int T^k{}_k\sqrt{-\mathrm{g}}d^3x = 0, \tag{7.43}$$

which should be fulfilled for any finite energy soliton configuration [75]. This is equivalent to the classical scaling relation of Derrick [76]. Therefore, (7.39) provides the generalization of Derrick's argument for black holes. This generalization is not unique, as ζ_μ in (7.38) can be multiplied by a scalar function without changing the value of the virial integral.

A similar virial relation in the gravity sector can be obtained by replacing $T^\mu{}_\nu$ with the Einstein tensor $G^\mu{}_\nu$:

$$v_g \equiv \int_{\mathrm{r}>\mathrm{r_H}} G^\mu{}_\nu\nabla_\mu\zeta^\nu\sqrt{-\mathrm{g}}d^3x = 0. \tag{7.44}$$

We adopt (7.39) and (7.44) as virial relations to test the quality of our numerical solutions. These relations are satisfied for all our solutions, with a precision depending on the numbers of discretization points N_x and N_ϑ along the x, ϑ axes (these numbers determine the triangulation pattern for the FreeFem solver). Taking $N_\mathrm{x} = 130$ and $N_\vartheta = 30$ typically yields $v_m \sim 10^{-7}$, $v_g \sim 10^{-8}$.

To the best of our knowledge, the above formulation of the virial relations has not been previously discussed in the literature, where alternative forms of virial relations can be found [see, e.g., Ref. [77]].

VIII. HAIRY SOLUTIONS WITH $n = \pm 4$

Before considering axially symmetric solutions with $|n| > 2$, we have reproduced the spherically symmetric solutions with $|n| = 2$ within the axially symmetric setting. This analysis, described in Appendix B, is needed to clarify the choice of the radial gauge. Here is the summary of the essential points.

A. Choice of the radial gauge

The axially symmetric fields in Eqs. (7.2), (7.22), and (7.27) depend on the radial coordinate r. This is not the same as the Schwarzschild coordinate r, and it is defined up to reparametrizations. This gauge freedom is fixed by specifying the auxiliary function N(r) in the line element (7.2).

For the nonextremal solutions, we choose

$$\mathrm{N}(\mathrm{r}) = 1 - \frac{\mathrm{r_H}}{\mathrm{r}}, \qquad \mathrm{r_H} \in [0, \mathrm{r_H^0}], \tag{8.1}$$

where $\mathrm{r} = \mathrm{r_H}$ corresponds to the position of the event horizon, and we refer to $\mathrm{r_H}$ as the "black hole size." However, since r is not the Schwarzschild coordinate, the parameter $\mathrm{r_H}$ does not have a direct physical meaning, although its value determines the horizon area. When

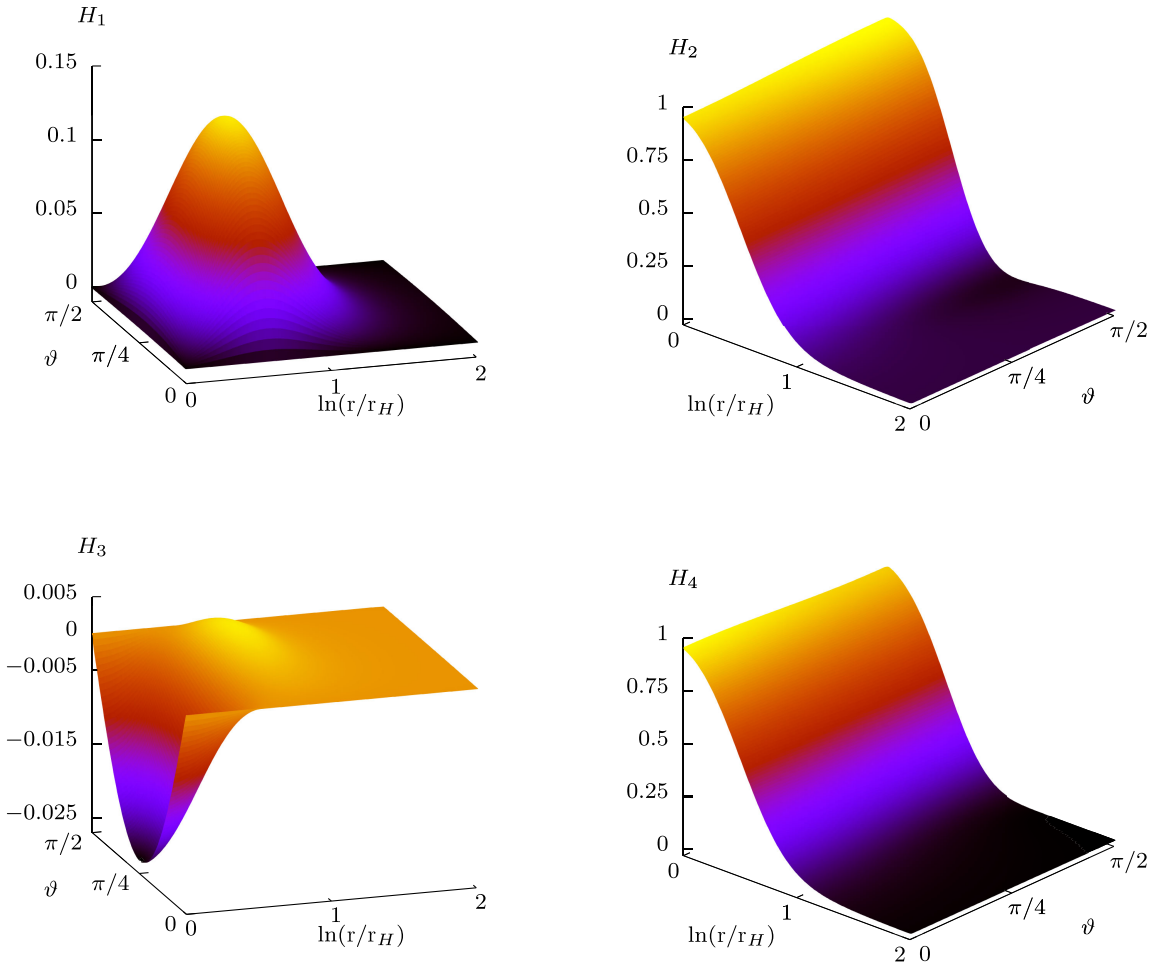


FIG. 7. The SU(2) amplitudes H_1, H_2, H_3, H_4 for the hairy black hole solution with $\kappa = 10^{-3}$, $\mathrm{r_H} = 0.7$, and $n = 4$ as functions of $\ln(\mathrm{r}/\mathrm{r_H})$ and ϑ.

$\mathrm{r_H} \to 0$, the solutions approach the extremal limit with a nonzero horizon area. When $\mathrm{r_H} \to \mathrm{r_H^0}$, the solutions merge with the RN solution, and we have $\mathrm{r_H^0} = r_+^0 - r_-^0$, where $r_+^0 = r_h^0$ and r_-^0 are the two RN horizons [see Eq. (B20)].

The RN solution (3.6), when transformed to the axially symmetric form (7.2) and (8.1), is expressed by Eq. (B3) in Appendix B.

The horizon values of the metric functions U, K, S grow without bounds in the extremal limit $\mathrm{r_H} \to 0$. Therefore, to study the extremal limit, we use a different gauge in which everything is finite at the horizon. This gauge is defined by

$$\mathrm{N(r)} = \mathrm{k^2(r)} \times \left(1 - \frac{\mathrm{r_H}}{\mathrm{r}}\right)^2,$$
$$\mathrm{k^2(r)} = 1 - \frac{\Lambda}{3}[\mathrm{r^2} + 2\mathrm{r_H r} + 3\mathrm{r_H^2}] \times \frac{1 + \mathrm{r_H^4}}{1 + \mathrm{r^4}}, \quad (8.2)$$

with $\mathrm{r_H} = r_{\mathrm{ex}}$, which is the horizon radius value for the extremal RNdS solution in Eq. (3.23). The horizon is located at $\mathrm{r} = \mathrm{r_H}$, and it is degenerate, meaning the surface gravity vanishes. This gauge choice is justified by the fact that, for some extremal hairy solutions (phase I), the horizon geometry coincides with that of the extremal RNdS geometry (3.25) and (3.7). The radial coordinate r then matches the Schwarzschild coordinate r at the horizon, where the function N(r) coincides with $N(r)$ from Eq. (3.25).

The gauge choices (8.1) and (8.2) are justified in Appendix B for spherically symmetric hairy solutions with $|n| = 2$, but they also apply to axially symmetric solutions with $|n| > 2$.

B. Structure of hairy solutions for $n = \pm 4$

The spherically symmetric solutions with $n = 2$ can be used as an initial guess to construct axially symmetric solutions with $n > 2$. Of course, n should be an integer to avoid the line singularities in the gauge fields, but the latter are not seen by the equations, which can be solved for any real n. Therefore, one can change the value of n by small steps, and we were able to proceed this way up to $n = 200$, beyond which the virial relations deteriorate.

We choose $n = 4$ to illustrate the solution profiles, as those for higher values of n are qualitatively the same.

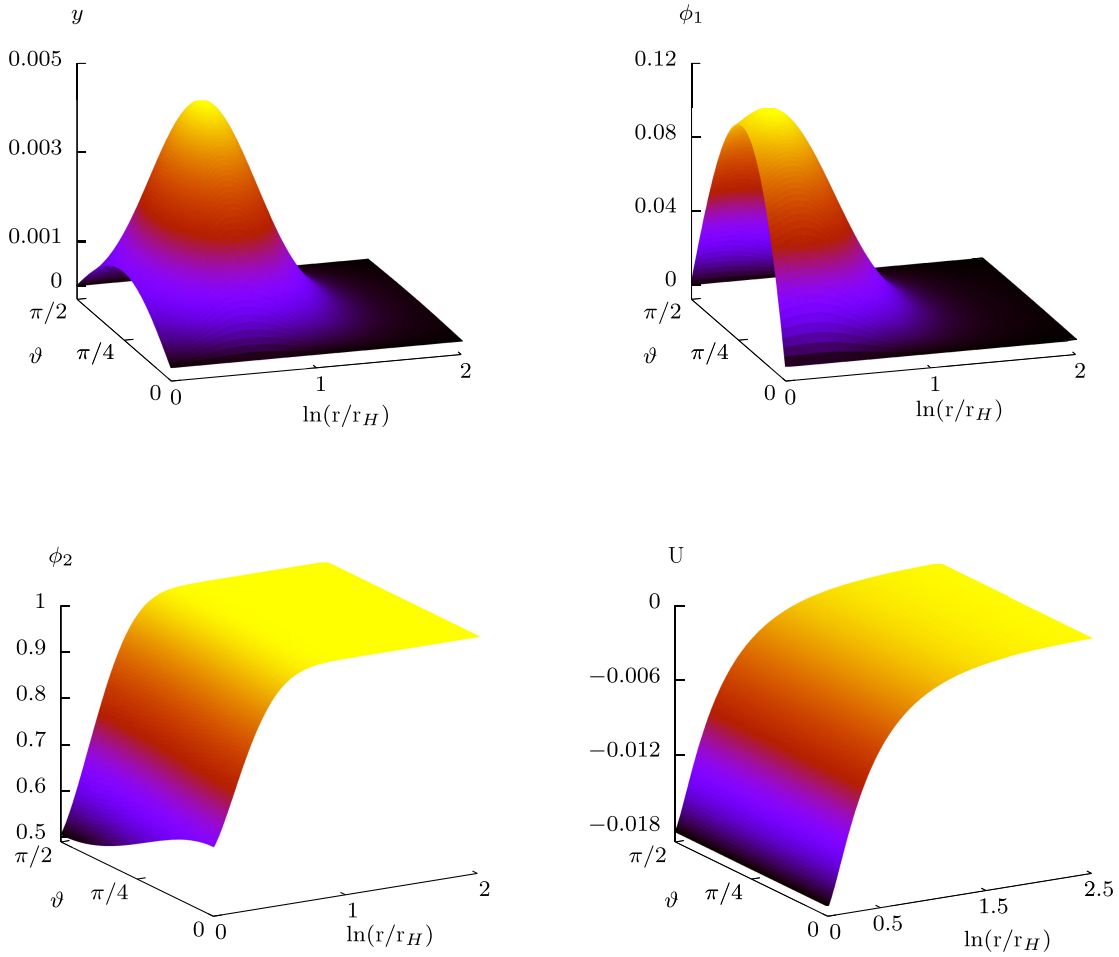


FIG. 8. The U(1) amplitude y, the Higgs amplitudes ϕ_1 and ϕ_2, and the metric amplitude U for the hairy black hole solution with $\kappa = 10^{-3}$, $r_H = 0.7$, and $n = 4$.

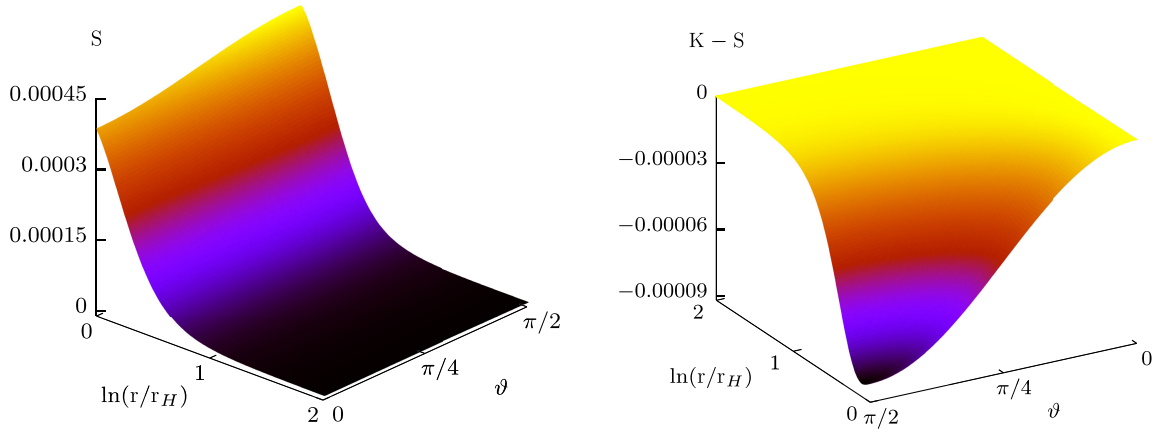


FIG. 9. The metric amplitude S and the difference K-S for the hairy black hole solution with $\kappa = 10^{-3}$, $r_H = 0.7$, $n = 4$.

Solutions with $n = 3$ are also qualitatively similar, but we choose $n = 4$ because, as mentioned above in Sec. VI and reiterated below, the solutions for $n = 4$ (but not for $n = 3$) appear to be stable.

The ten amplitudes $H_k, y, \phi_1, \phi_2, \mathrm{U}, \mathrm{K}, \mathrm{S}$ are invariant under $n \to -n$, but the fields in the ansatz (7.22), along with the electric currents (2.41) and the magnetic charge density (2.51), are sensitive to the sign of n. We set $\kappa = 10^{-3}$ instead

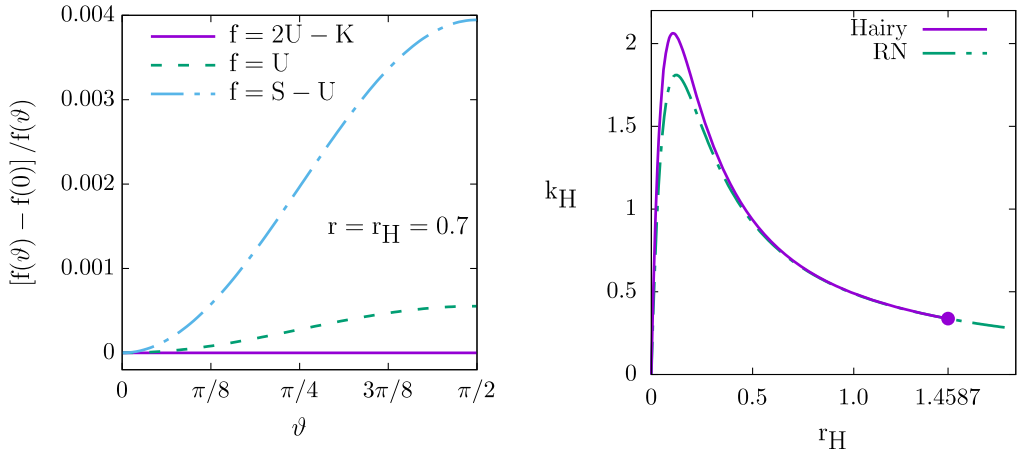


FIG. 10. Left: the angular dependence of 2U–K, U, and S–U at the horizon for the hairy black hole solution with $\kappa = 10^{-3}$, $r_H = 0.7$, and $n = 4$. Right: the surface gravity as a function of r_H for the hairy solutions with $\kappa = 10^{-3}$, $n = 4$, and for the RN solution. The maximal value of the surface gravity, and hence of the Hawking temperature $T = k_H/(2\pi)$, is higher for the hairy solutions than for the RN solution.

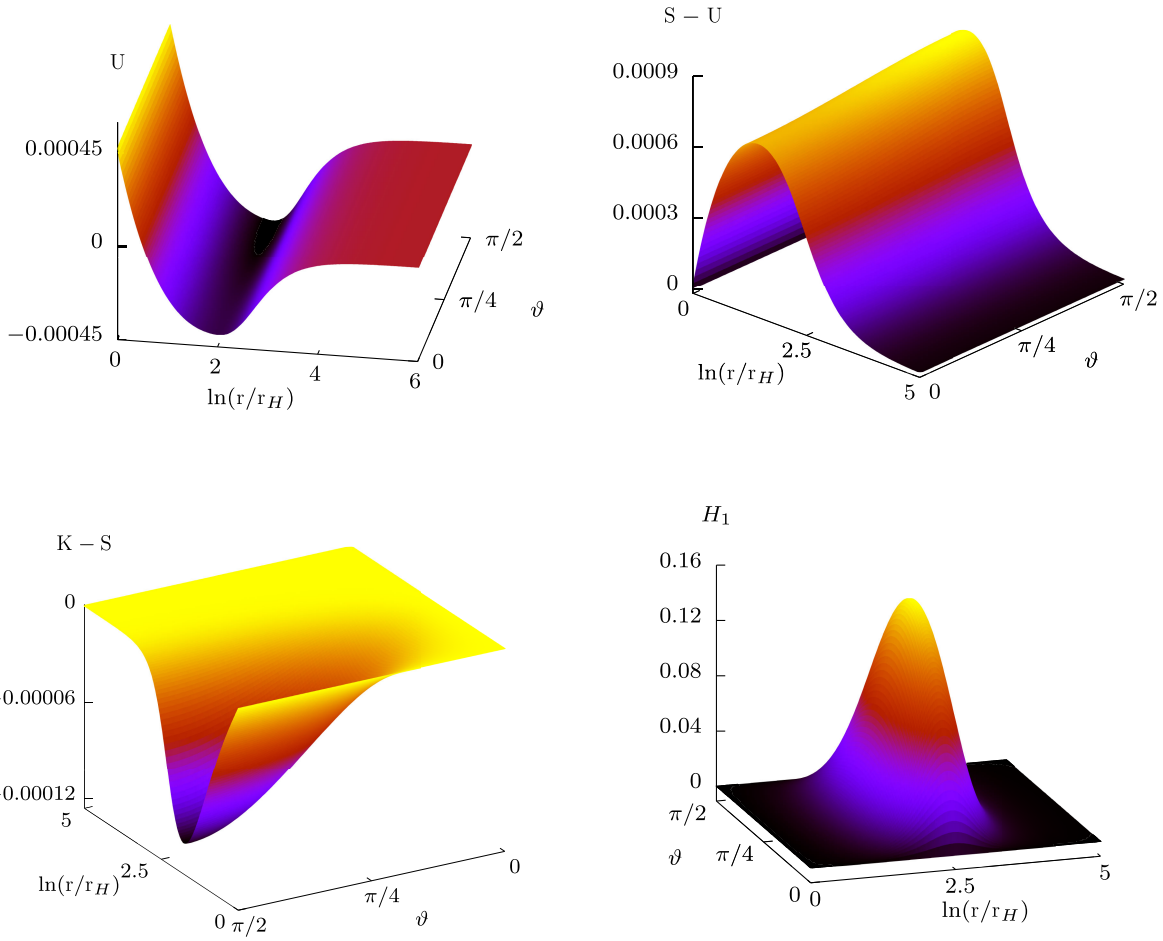


FIG. 11. The profiles of U, S–U, K–S, and H_1 for the extremal hairy black hole with $\kappa = 10^{-3}$ and $n = 4$.

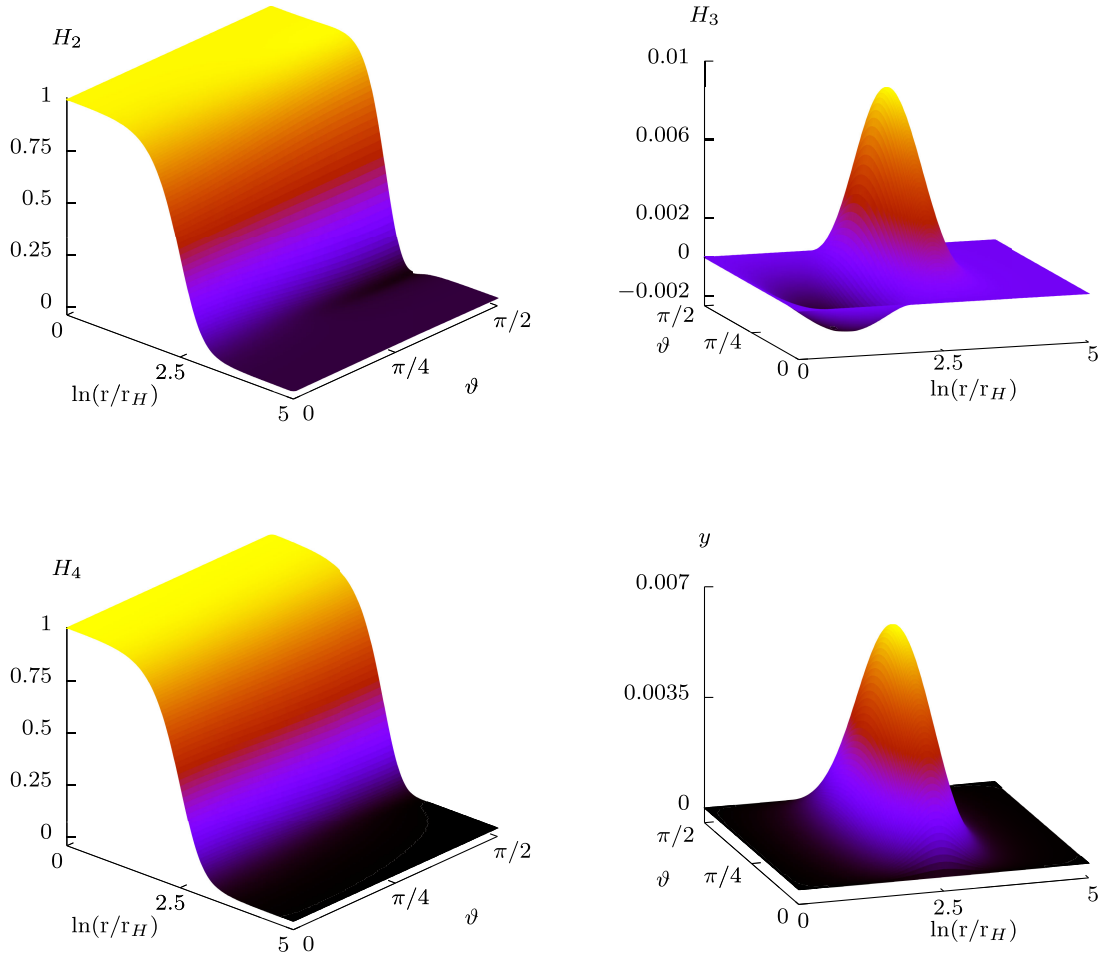


FIG. 12. The profiles of H_2, H_3, H_4, and y for the extremal hairy black hole with $\kappa = 10^{-3}$ and $n = 4$.

of choosing the physical value $\kappa \sim 10^{-33}$, as otherwise, the backreaction on the spacetime geometry would be difficult to observe. However, later we extrapolate the results to the physical value of κ. The radial gauge is fixed according to (8.1), where the black hole size parameter $\mathrm{r_H}$ ranges from zero up to the maximal value $\mathrm{r_H^0} \approx 1.4587$, which corresponds to the bifurcation with the RN solution.

If $\mathrm{r_H}$ is close to the upper bound $\mathrm{r_H^0}$, then the black holes are only "slightly hairy," and the geometry is close to the RN with magnetic charge $P = 2/e$. We therefore choose an intermediate value, $\mathrm{r_H} = 0.7$, and show in Figs. 7–9 the profiles of the ten amplitudes $H_k, y, \phi_1, \phi_2, \mathrm{U}, \mathrm{K}, \mathrm{S}$ as functions of $\ln(\mathrm{r/r_H})$ and ϑ. The symmetry axis is at $\vartheta = 0$, and the equator is at $\vartheta = \pi/2$.

The functions H_2, H_4, and ϕ_2, which do not vanish in the spherically symmetric case $n = 2$ [see Eq. (B2)], remain essentially the same and exhibit only weak ϑ dependence for $n = 4$. On the other hand, the functions H_1, H_3, y, ϕ_1, which vanish for $n = 2$, are no longer zero for $n > 2$. They exhibit strong ϑ dependence, with a pronounced maximum or minimum between the symmetry axis and the equatorial plane, and are antisymmetric under $\vartheta \to \pi - \vartheta$. Their ϑ dependence remains significant even at the horizon, except for H_1, which vanishes there.

The metric functions U, K, S almost do not depend on the angle ϑ and are close to the values defined by Eq. (B3) in the RN case. In particular, one has $\mathrm{K} \approx \mathrm{S}$. The difference K-S is maximal at the equator and can be seen as a measure of the deviation from spherical symmetry. For $\vartheta = 0$, one has $\mathrm{K} = \mathrm{S}$ and also $\partial_\vartheta \mathrm{K} = \partial_\vartheta \mathrm{S} = 0$. In view of Eq. (7.15), this guarantees that the two gravitational constraints $\mathcal{C}_1$ and $\mathcal{C}_2$ vanish at the symmetry axis, and Eq. (7.14) then implies that they should vanish everywhere, which is indeed confirmed with a good precision. All three metric functions U, K, S show a weak ϑ dependence at the horizon, but as required by Eq. (7.20), the combination 2U–K, which determines the surface gravity,

$$\mathrm{k_H} = \frac{\mathrm{N}'}{2} e^{2\mathrm{U}-\mathrm{K}}\Big|_{\mathrm{r=r_H}} = \frac{1}{2\mathrm{r_H}} e^{2\mathrm{U}-\mathrm{K}}\Big|_{\mathrm{r=r_H}}, \tag{8.3}$$

should be constant at the horizon. This is indeed confirmed by the numerics (see Fig. 10) and shows that the constraints are fulfilled.

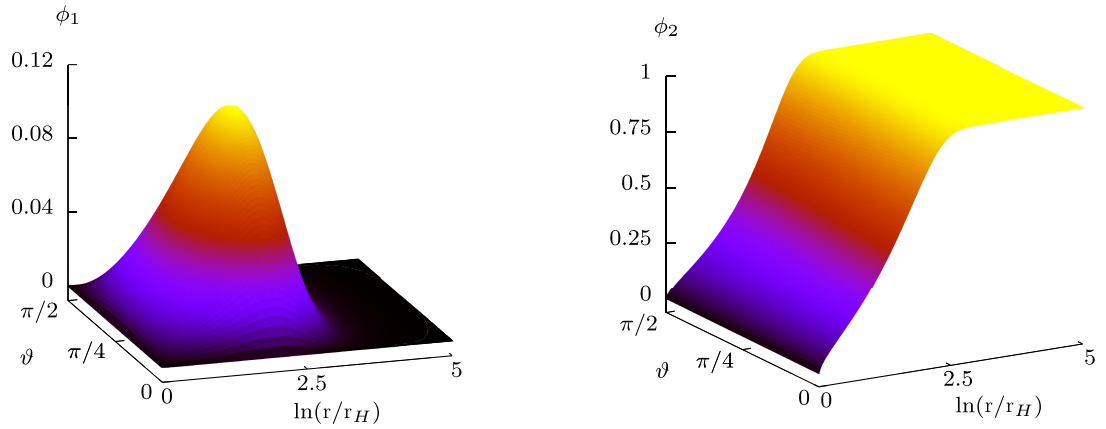


FIG. 13. The Higgs amplitudes ϕ_1 and ϕ_2 for the extremal hairy black hole with $\kappa = 10^{-3}$ and $n = 4$.

For the solution with $r_H = 0.7$ displayed in Figs. 7–9, one has $(2U - K)|_{r=r_H} = -0.0377$. Injecting this into (8.3) yields the value $k_H = 0.6878$.

When the horizon size decreases, the surface gravity first increases but then reaches a maximum value and starts decreasing, approaching zero in the extremal limit (see Fig. 10). In the extremal limit, $r_H \to 0$, the factor $1/r_H$ in (8.3) diverges, but its growth is damped by the exponent e^{2U-K}, which approaches zero because the horizon value of 2U–K becomes large and negative. Therefore, as in the spherically symmetric case, the horizon values of U and K grow without bound as the extremal limit is approached. The same conclusion holds for the S amplitude.

To analyze the extremal limit, we choose N(r) according to (8.2). Then, $N'(r_H) = 0$, and the surface gravity vanishes without requiring large values of the metric amplitudes at the horizon. The profiles of the extremal solution with $n = 4$ and $\kappa = 10^{-3}$ are shown in Figs. 11–13. The most notable change compared to the nonextremal solution in Figs. 7–9 is in the profiles of U and S–U. They show a nonmonotonic dependence on r and become very similar to those for the extremal spherically symmetric solution with $n = 2$ shown in Fig. 24 in Appendix B (for the nonextremal solution, one has $S - U \approx -U$).

Another important change is that all amplitudes are now constant at the horizon: S–U, K–S, H_1, H_3, y, ϕ_1, and ϕ_2 all vanish, H_2 and H_4 equal to unity, whereas U assumes a constant value. Therefore, the electroweak fields are in the false vacuum, $W^a_\mu = \Phi = 0$ [when expressed in the gauge (7.29) and (7.31)], and the horizon geometry is perfectly spherical, as will be shown in the next section. Thus, the horizon geometry coincides with that of the extremal RNdS solution (3.25). This motivates the gauge choice (8.2) with $r_H = r_{ex}$ given by (3.23).

We have described above hairy solutions for $n = 2$ and $n = 4$. The $n = 3$ solution is qualitatively the same as the one for $n = 4$. However, one may also wonder what happens when $n = 1$. The perturbation theory developed in Secs. IV and VI is valid only for $|n| > 1$, since for $|n| = 1$, the perturbations are unbounded. This implies that there are no hairy solutions with $|n| = 1$ bifurcating from the RN family. However, there could be hairy solutions that do not intersect with the RN family. To detect them, we start from the hairy solutions with $n = 2$ and then iteratively decrease n down to $n = 1$. The numerical procedure converges, but the properties of the result, such as the virial relation, suggest that this is not a true solution but rather a numerical artifact. Therefore, it seems that there are no hairy solutions with $n = \pm 1$ within the axially symmetric ansatz.

IX. PROPERTIES OF HAIRY BLACK HOLES

Let us now provide a more general description of hairy solutions for higher values of the magnetic charge. Nonextremal hairy black hole form a two-parameter family, characterized by an integer n that determines the magnetic charge and a real parameter r_H that sets the horizon size. At large distances from the horizon, the fields asymptotically approach those of the RN solution with magnetic charge $P = n/(2e)$. To begin with, we assume that the charge is not too large, such that $|Q| = \sqrt{\kappa/2}|P| \ll Q_m$, where Q_m is defined in (3.24).

We emphasize once again that the size parameter r_H does not have a direct physical meaning but merely serves as a label for the solutions. Its value determines the event horizon area A_H according to (7.19), and as r_H decreases, the horizon area shrinks.

When the size parameter reaches its maximal value, $r_H = r^0_H(n)$, the hairy solution reduces to the RN black hole of charge Q and horizon radius $r_h = r^0_h(n)$. The values of $r^0_h(n)$ for small n are shown in Table II (for $\kappa = 5.3 \times 10^{-33}$), while for large $|n|$, we find that $r^0_h(n) \approx \sqrt{|n|}/g$.

The relation between the maximal value $r^0_H(n)$ and the Schwarzschild radial coordinate $r^0_h(n)$ of the RN horizon is given by

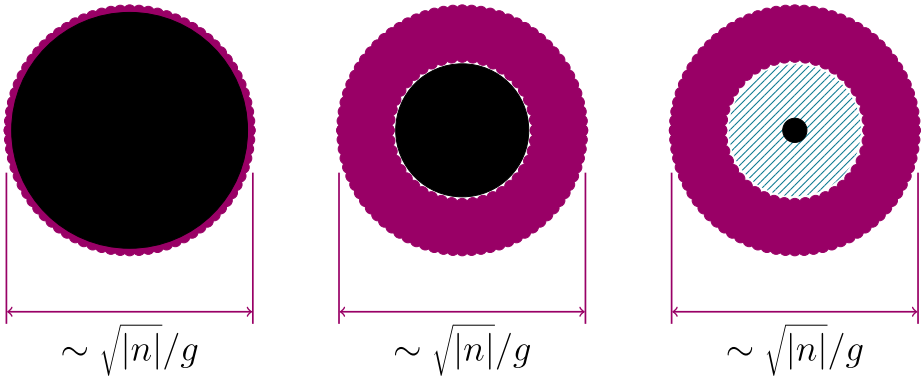


FIG. 14. As the horizon size decreases, the hair first emerges (left), then extends further (center), and eventually, a bubble of symmetric phase forms around the horizon (right).

$$\mathrm{r}_{\mathrm{H}}^{0}(n) = r_h^0(n) - \frac{Q^2}{r_h^0(n)} = r_h^0(n) + \mathcal{O}(\kappa). \tag{9.1}$$

For this value of $\mathrm{r_H}$, the strength of the hypermagnetic field at the horizon is just enough to trigger the electroweak condensation. In this regime, the condensate can be described perturbatively by linearizing the W equations around the RN background, which leads to Eq. (4.3). The solution to this equation, given by Eqs. (4.5) and (4.7), approaches zero outside the horizon more rapidly as $|n|$ increases [see Fig. 2]. Hence, close to the bifurcation point and for large $|n|$, the electroweak condensate is strongly localized near the horizon, as illustrated schematically in Fig. 14 (left panel).

When the size $\mathrm{r_H}$ becomes smaller than $\mathrm{r}_{\mathrm{H}}^{0}(n)$, the condensate begins to backreact, changing the geometry so that it is no longer purely RN. In this regime, the electroweak condensate extends further, spanning the interval $\mathrm{r} \in [\mathrm{r_H}, \mathrm{r}_{\mathrm{H}}^{0}]$, where the hypermagnetic field satisfies the condition $|\mathrm{B}| > m_{\mathrm{W}}^2$. The condensate terminates at approximately $\mathrm{r} \approx \mathrm{r}_{\mathrm{H}}^{0}(n) \approx r_h^0(n)$, where the hypermagnetic field reduces to the threshold value $|\mathrm{B}| \approx m_{\mathrm{W}}^2$ [Fig. 14, central panel].

When $\mathrm{r_H}$ decreases below a critical value $\mathrm{r}_{\mathrm{H}}^{\mathrm{b}}$, where the hypermagnetic field reaches the second threshold $|\mathrm{B}(\mathrm{r}_{\mathrm{H}}^{\mathrm{b}})| \approx m_{\mathrm{H}}^2$, the massive condensate ceases to expand and remains confined within the region $\mathrm{r}_{\mathrm{H}}^{\mathrm{b}} < \mathrm{r} < \mathrm{r}_{\mathrm{H}}^{0}$, where the field strength satisfies $m_{\mathrm{H}}^2 > |\mathrm{B}| > m_{\mathrm{W}}^2$. In the near-horizon region $\mathrm{r_H} < \mathrm{r} < \mathrm{r}_{\mathrm{H}}^{\mathrm{b}}$, the hypermagnetic field becomes strong enough, $|\mathrm{B}| > m_{\mathrm{H}}^2$, to suppress the W and Higgs fields. As a result, the full electroweak gauge symmetry is restored in this region [see Fig. 14, right panel]. This bubble of symmetric phase expands as $\mathrm{r_H}$ decreases further, reaching its maximal extent in the $\mathrm{r_H} \to 0$ limit. In this extremal limit, the horizon surface gravity vanishes, yet the horizon area remains finite.

A. The horizon oblateness

The hairy solutions are not spherically symmetric because the condensate is compressed toward the equatorial plane. Since the condensate backreacts and influences the spacetime geometry, the event horizon itself is not perfectly spherical. As a result, there is no uniquely defined event horizon radius.

However, the horizon area $\mathrm{A_H}$ remains a well-defined quantity and can be computed using Eq. (7.19). This allows us to *define* an effective average event horizon radius as

$$r_h = \sqrt{\frac{\mathrm{A_H}}{4\pi}}. \tag{9.2}$$

As illustrated in Fig. 15, the average radius r_h [and consequently the horizon area $\mathrm{A_H}$] is a monotonic function of $\mathrm{r_H}$. In the extremal limit $\mathrm{r_H} \to 0$, the radius and area approach finite values. Figure 15 also displays the surface gravity $\mathrm{k_H}$, computed from Eq. (7.19), which tends to zero in the extremal limit, as expected.

Since the horizon is not spherically symmetric, one can define the equatorial radius and polar radius as follows:

$$\begin{aligned} r_h^{\mathrm{eq}} &= \sqrt{g_{\varphi\varphi}}|_{\mathrm{r}=\mathrm{r_H},\vartheta=\pi/2} = \mathrm{r_H} e^{\mathrm{S-U}}|_{\mathrm{r}=\mathrm{r_H},\vartheta=\pi/2}, \\ r_h^{\mathrm{pl}} &= \frac{1}{\pi}\int_0^{\pi} \sqrt{\vartheta_\vartheta}|_{\mathrm{r}=\mathrm{r_H}} d\vartheta = \frac{\mathrm{r_H}}{\pi}\int_0^{\pi} e^{\mathrm{K-U}}|_{\mathrm{r}=\mathrm{r_H}} d\vartheta. \end{aligned} \tag{9.3}$$

This allows us to introduce the horizon oblateness, which is defined as

$$\delta = \frac{r_h^{\mathrm{eq}}}{r_h^{\mathrm{pl}}} - 1. \tag{9.4}$$

As seen in Fig. 15, the oblateness is positive and vanishes in the RN limit as expected. Interestingly, it also vanishes in the extremal limit, a feature that will be further analyzed below.

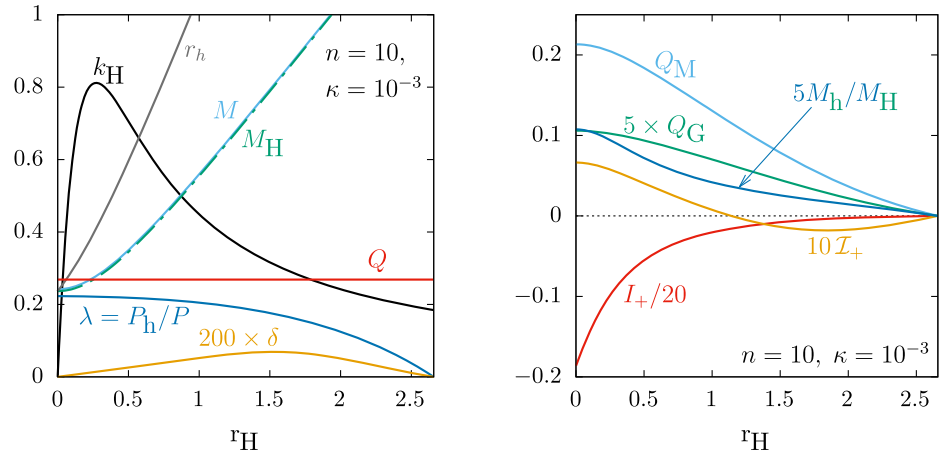


FIG. 15. Parameters of the nonextremal solutions with $n = 10$ and $\kappa = 10^{-3}$. As $r_H \to 0$, the solutions become extremal, while for $r_H \to 2.66$, they lose their hair and merge with the RN solution. The mass M of extremal and near extremal solutions is *less* than the charge Q.

B. The charge

Within the Nambu description, the total magnetic charge of the black hole splits into two components:

$$P = P_H + P_h = \frac{n}{2e}, \tag{9.5}$$

where P_h is the charge contained in the condensate outside the horizon. It is computed in the same way as in the spherically symmetric case in Eq. (5.7):

$$\begin{aligned} P_h &= \int_{r>r_H} \tilde{J}^0 \sqrt{-g} d^3x = \frac{e}{8\pi} \int_{r>r_H} \epsilon^{ijk} \partial_i \psi_{jk} d^3x \\ &= -\frac{e}{8\pi} \oint_{r=r_H} \psi_{jk} dx^j \wedge dx^k \\ &= -\frac{e}{4\pi} \oint_{r=r_H} \psi_{\vartheta\varphi} d\vartheta d\varphi \equiv \gamma g'^2 P \equiv \lambda P. \end{aligned} \tag{9.6}$$

Here, $\psi_{\mu\nu}$ is defined in (2.35). The remaining charge, $P_H = P - P_h$, is contained inside the black hole.

The ratio $\lambda = P_h/P$ vanishes in the RN limit $r_H \to r_H^0(n)$ and reaches its maximal value of $g'^2 \approx 0.22$ in the extremal limit $r_H \to 0$ [provided that the total charge P is not too large, as discussed in Sec. X below]. In this case we have $P_h \approx 0.22 \times P$ [see Fig. 15]. We also introduce the parameter $\gamma = P_h/(g'^2 P) = \lambda/g'^2$, which varies from zero to 1. In the spherically symmetric case, this parameter corresponds to $\gamma = f_h^2$, as seen in Eq. (5.7).

In summary, hairy black holes exist for $r_H \in [0, r_H^0]$. They lose their hair in the RN limit $r_H \to r_H^0$, where all the charge is contained inside the black hole. In contrast, they become maximally hairy in the extremal limit $r_H \to 0$, with approximately 22% of the magnetic charge contained in the hair outside the horizon.

C. The ADM mass

The ADM mass M can be determined either from the asymptotic expansion of the metric coefficient, $g_{00} = -1 + 2M/r + \mathcal{O}(1/r^2)$, or from the integral expression derived using the Einstein equations in (7.17),

$$M = \frac{k_H A_H}{4\pi} + \frac{\kappa}{8\pi} \int_{r>r_H} (-T^0{}_0 + T^k{}_k) \sqrt{-g} d^3x, \tag{9.7}$$

where the surface gravity k_H and the horizon area A_H are given by Eq. (7.19). Both methods yield consistent results with the same level of precision as for the virial relation.

As in the spherically symmetric case, the total mass can be decomposed as $M = M_H + M_h$, where M_H represents the mass of the RN black hole with the same area A_H and charge P_H. Some clarifications are necessary for computing M_H.

The horizon radius of the RN solution with the magnetic charge P and mass M is given by $r_h = M + \sqrt{M^2 - Q^2}$, where $Q^2 = (\kappa/2)P^2$. Expressing M in terms of r_h, we obtain

$$M = \frac{r_h}{2} + \frac{Q^2}{2r_h} = \frac{r_h}{2} + \frac{\kappa P^2}{4r_h}. \tag{9.8}$$

On the other hand, the total magnetic charge is carried by both the U(1) gauge field B_μ and the SU(2) field W^a_μ, leading to a decomposition: $P = P_{U(1)} + P_{SU(2)}$, where $P_{U(1)} = g^2 P$ and $P_{SU(2)} = g'^2 P$. Importantly, the square of the total charge P^2 in Eq. (9.8) can be represented in the form

$$P^2 = \frac{1}{g^2} P^2_{U(1)} + \frac{1}{g'^2} P^2_{SU(2)}. \tag{9.9}$$

This formula is crucial: although P is the sum of two

charges, P^2 should not be computed as the square of the sum. Instead, one must use Eq. (9.9) because the two charges are of different nature, and only the square of each charge contributes to the energy.

The magnetic charge of the hairy black hole splits as $P = P_{\rm H} + P_{\rm h}$, where $P_{\rm H}$ is the charge inside the black hole, and $P_{\rm h}$ is the hair charge defined by Eq. (9.6). The hair charge is always a part of the non-Abelian charge $P_{\rm SU(2)}$, leading to the relations

$$P_{\rm h} = \gamma P_{\rm SU(2)}, \qquad P_{\rm H} = P_{\rm U(1)} + (1-\gamma)P_{\rm SU(2)}, \tag{9.10}$$

where $\gamma \in [0,1]$ is the same parameter as that introduced in Eq. (9.6). Comparing with Eq. (9.9), the square of the charge contained inside the black hole is given by

$$P_{\rm H}^2 = \frac{1}{g^2}P_{\rm U(1)}^2 + \frac{(1-\gamma)^2}{g'^2}P_{\rm SU(2)}^2 = (g^2 + (1-\gamma)^2 g'^2)P^2. \tag{9.11}$$

Using the definition (9.2) of the average horizon radius r_h and comparing with Eq. (9.8), yields the following formula for computing the horizon mass:

$$M_{\rm H} = \frac{r_h}{2} + \frac{\kappa P_{\rm H}^2}{4r_h} = \frac{1}{2}\left(r_h + (g^2 + (1-\gamma)^2 g'^2)\frac{Q^2}{r_h}\right). \tag{9.12}$$

This expression matches the formula in Eq. (5.12) derived in the spherically symmetric case, upon replacing $\gamma \to f_h^2$. In the RN limit, where $\gamma = 0$, the expression reduces to Eq. (9.8). In the extremal limit, where $\gamma = 1$, the average radius is $r_h = r_{\rm ex} \approx g|Q|$, yielding

$$M_{\rm H} = \frac{1}{2}\left(r_h + g^2\frac{Q^2}{r_h}\right) \approx g|Q|. \tag{9.13}$$

As seen in Fig. 15, the mass M increases with $\mathrm{r_H}$. For $\kappa = 10^{-3}$, one finds that $M \approx M_{\rm H}$ (when $|Q| \ll Q_{\rm m}$). However, the relative contribution of the hair mass, $M_{\rm h}/M_{\rm H}$, grows with $|n|$. This contribution reaches its maximum in the extremal limit, where the black hole is maximally hairy, and vanishes in the RN limit.

D. Quadrupole moments

Far away from the horizon, all massive fields approach their vacuum values, and one has

$$B_\mu = \mathrm{W}^3_\mu \equiv eA_\mu, \qquad \mathrm{W}^1_\mu = \mathrm{W}^2_\mu = 0, \qquad \Phi = \begin{pmatrix} 0 \\ 1 \end{pmatrix}; \tag{9.14}$$

thus the theory reduces to the electrovacuum:

$$\mathcal{L} = \frac{1}{2\kappa}R - \frac{1}{4}F_{\mu\nu}F^{\mu\nu}, \tag{9.15}$$

where $F_{\mu\nu} = \partial_\mu A_\nu - \partial_\nu A_\mu$. Therefore, the hairy solutions approach an electrovacuum configuration at large distances, which to leading order corresponds to a magnetic RN black hole of mass M and charge $Q = \sqrt{\kappa/2}P$. However, the asymptotic behavior also contains subleading terms that encode deviations from the pure RN solution and give rise to gravitational and magnetic multipole moments. This allows us to define the gravitational $Q_{\rm G}$ and magnetic $Q_{\rm M}$ quadrupole moments.

Determining these moments proved to be particularly challenging, as the existing literature on gravitational multipoles often presents conflicting results. The correct formalism was developed by Geroch [78] and Hansen [79], but its direct application is difficult in our setting. Fortunately, Fodor *et al.* [80,81] showed that the Geroch–Hansen procedure can be reformulated in terms of the asymptotic expansion of the Ernst potentials in Weyl coordinates. Adopting this method, we were able to compute the quadrupole moments through the following steps.

Choosing the gauge where $\mathrm{N(r)} = 1$, the line element in Eq. (7.2) simplifies to

$$ds^2 = -e^{2\mathrm{U}}dt^2 + e^{-2\mathrm{U}}dl^2, \tag{9.16}$$

where the three metric is

$$dl^2 \equiv h_{ik}dx^i dx^k = e^{2\mathrm{K}}(d\mathrm{r}^2 + \mathrm{r}^2 d\vartheta^2) + \mathrm{r}^2 e^{2\mathrm{S}}\sin^2\vartheta d\varphi^2. \tag{9.17}$$

The purely magnetic Maxwell field $F_{\mu\nu}$ can be expressed in terms of a magnetic potential Ψ as

$$\sqrt{\frac{\kappa}{2}}F_{ik} = e^{-2\mathrm{U}}\sqrt{h}\epsilon_{iks}\partial^s\Psi. \tag{9.18}$$

In the far field region, the hairy solutions reduce to

$$e^{2\mathrm{U}} = e^{2\delta\mathrm{U}}\frac{x^2-\mu^2}{(x+M)^2}, \qquad e^{\mathrm{K}} = e^{\delta\mathrm{K}}\left(1 - \frac{\mu^2}{4\mathrm{r}^2}\right),$$
$$e^{\mathrm{S}} = e^{\delta\mathrm{S}}\left(1 - \frac{\mu^2}{4\mathrm{r}^2}\right), \qquad \Psi = \frac{Q}{x+M} + \delta\Psi, \tag{9.19}$$

where $\delta\mathrm{U}, \delta\mathrm{K}, \delta\mathrm{S}, \delta\Psi$ are the subleading terms describing deviations from the RN background. The variable x and the radial coordinate r are related by $x = \mathrm{r} + \mu^2/(4\mathrm{r})$, where $\mu^2 = M^2 - Q^2$. As seen in Fig. 15 (left panel), μ^2 is not necessarily positive.

In the leading order, the expressions in (9.19) correspond to the RN solution expressed in isotropic coordinates. By solving the equations of the electrovacuum theory (9.15) in

the power series, we obtain the deviations

$$\delta \mathrm{S} = -\frac{s_2}{2\mathrm{r}^2} + \ldots,$$
$$\delta \mathrm{K} = s_2 \frac{2\sin^2\vartheta - 1}{2\mathrm{r}^2} + \ldots,$$
$$\delta \mathrm{U} = \frac{Q_g(1 - 3\cos^2\vartheta) - M s_2/3}{2\mathrm{r}^3} + \ldots,$$
$$\delta \Psi = \frac{Q_m(1 - 3\cos^2\vartheta) + Q s_2/3}{2\mathrm{r}^3} + \ldots, \tag{9.20}$$

where Q_g, Q_m, and s_2 are integration constants, and the dots indicate higher-order terms. These constants can be determined from our numerical solutions, keeping in mind that the numerical solutions were obtained in a different radial gauge where $\mathrm{N}(\mathrm{r}) \neq 1$.

Introducing the Ernst potential [82,83], defined as

$$\mathcal{E} = e^{2\mathrm{U}} - \Psi^2, \tag{9.21}$$

the gravitational Q_G and magnetic Q_M quadrupole moments are determined by the asymptotic behavior of

$$\xi_\mathrm{G} = \frac{1 - \mathcal{E}}{1 + \mathcal{E}}, \qquad \xi_\mathrm{M} = \frac{2\Psi}{1 + \mathcal{E}} \tag{9.22}$$

near spatial infinity [80,81]. To achieve this, one must switch to the Weyl coordinates (ρ, z), where the three metric in (9.17) becomes

$$dl^2 = e^{2\mathrm{K}}(d\mathrm{r}^2 + \mathrm{r}^2 d\vartheta^2) + e^{2\mathrm{S}}\mathrm{r}^2\sin^2\vartheta d\varphi^2$$
$$= e^{2K(\rho,z)}(d\rho^2 + dz^2) + \rho^2 d\varphi^2, \tag{9.23}$$

with $K(\rho, z)$ expressed in terms of K, S. The next step is to consider the asymptotic expansions at the symmetry axis ($\rho = 0$, $z \to \infty$):

$$\xi_\mathrm{G} = \sum_{k\geq 0} \frac{a_k}{z^{k+1}}, \qquad \xi_\mathrm{M} = \sum_{k\geq 0} \frac{b_k}{z^{k+1}}. \tag{9.24}$$

The gravitational and magnetic quadrupole moments are then given by $Q_\mathrm{G} = -a_2$ and $Q_\mathrm{M} = -b_2$. Therefore, the task is to compute the coefficients a_2 and b_2 in the series (9.24).

To pass to the Weyl coordinates, we notice that since $T^r_r + T^\vartheta_\vartheta = 0$ in the electrovacuum, Eq. (7.10) with $\mathrm{N}(\mathrm{r}) = 1$ yields the exact solution for the amplitude S in (9.17),

$$e^\mathrm{S} = 1 + \frac{\mathrm{const}}{\mathrm{r}^2} = 1 - \frac{\mu^2 + 2s_2}{4\mathrm{r}^2}, \tag{9.25}$$

where we have also used (9.19) and (9.20). This implies that the relation between the Weyl coordinates ρ, z in (9.23) and the original coordinates r, ϑ in (9.17) is provided by the complex Joukowski transformation:

$$\rho + iz = \varpi - \frac{\mu^2 + 2s_2}{4\varpi}, \quad \text{with} \quad \varpi = i\mathrm{r}e^{-i\vartheta}. \tag{9.26}$$

Using this relation, the three metric in (9.17) can be transformed to the Weyl coordinates. After computing the potentials ξ_G and ξ_M, expanding them according to (9.24), and using (9.19) and (9.20), we obtain the expressions for the gravitational and magnetic quadrupole moments:

$$Q_\mathrm{G} = -Q_g - \frac{2}{3}M s_2, \qquad Q_\mathrm{M} = Q_m - \frac{2}{3}Q s_2. \tag{9.27}$$

It is important to note that the radial coordinate r used in (9.20) corresponds to the gauge where $\mathrm{N}(\mathrm{r}) = 1$, while our numerical solutions were obtained in a different gauge where $\mathrm{N}(\mathrm{r}) = 1 - \mathrm{r}_\mathrm{H}/\mathrm{r}$. Taking all this into account, we can determine the quadrupole moments, as shown in Fig. 15.

The quadrupole moments vanish for large r_H when the solution reduces to the RN. They grow as r_H decreases and the solution becomes more and more hairy. They reach maximal values in the extremal limit.

E. Condensate, vector fields, and currents

In the unitary gauge, the electroweak condensate around the black hole is described by a complex vector w^μ that satisfies Eq. (6.8c). The charged condensate induces an electric current J^μ, defined by Eqs. (6.5) and (6.10), which flows along the horizon. The current, in turn, generates the electromagnetic and Z fields governed by (6.8a) and (6.8b), forming a corona of vortices orthogonal to the horizon.

However, using the unitary gauge may lead to complications when the Higgs field approaches zero (see Appendix B in [59]), which occurs in the extremal limit. To avoid this issue, we do not impose the unitary gauge and use the fields $B_{\mu\nu}, \mathrm{W}^a_{\mu\nu}, \Phi$ obtained from our numerical solutions. Then we compute the unit vector

$$n^a = \frac{(\Phi^\dagger \tau^a \Phi)}{(\Phi^\dagger \Phi)}, \tag{9.28}$$

whose components remain finite when Φ approaches zero. The condensate density can be characterized by the tensor

$$\psi_{\mu\nu} = -\frac{1}{g^2}\epsilon_{abc} n^a \mathcal{D}_\mu n^b \mathcal{D}_\nu n^c, \tag{9.29}$$

as defined in Eq. (2.35). Using n^a, $\psi_{\mu\nu}$, one can compute the electromagnetic and Z fields. These fields are described by $\mathcal{F}_{\mu\nu}$ and $\mathcal{Z}_{\mu\nu}$, as defined in Eq. (2.26) following Nambu, or by $F_{\mu\nu}$ and $Z_{\mu\nu}$, as defined in Eq. (2.37) following 't Hooft.

The divergences of $\mathcal{F}_{\mu\nu}$ and $F_{\mu\nu}$ yield, according to Eq. (2.41), the currents $\mathcal{J}^\mu$ and J^μ, respectively. The definitions of Nambu and 't Hooft lead to two distinct yet dual interpretations of the near-field structure of solutions. However, global parameters such as the total charge and quadrupole moment are determined by the far-field behavior. Since the difference between $\mathcal{F}_{\mu\nu} - F_{\mu\nu} = e\psi_{\mu\nu}$ decays exponentially at infinity, these global quantities remain the same in both descriptions.

1. 't Hooft description

Let us consider first the fields $F_{\mu\nu}$ and $Z_{\mu\nu}$, and the associated current J^μ. According to Eq. (6.8b), the neutral current is given by $J^\mu_Z = -(g/g')J^\mu$.

As discussed in Sec. VI within the perturbative approach, the current J^μ flows along the horizon, generating vortices orthogonal to it. This behavior persists at the nonperturbative level as well. In the axially symmetric case under consideration, the current is purely azimuthal.

The electromagnetic tensor has the structure

$$\frac{1}{2}F_{\mu\nu}dx^\mu \wedge dx^\nu = P\sin\vartheta d\vartheta \wedge d\varphi + \Delta F_{\mathrm{r}\varphi} d\mathrm{r} \wedge d\varphi + \Delta F_{\vartheta\varphi} d\vartheta \wedge d\varphi, \tag{9.30}$$

where the first term on the right describes the radial magnetic field surrounding the black hole in the absence of the condensate. The remaining two terms, involving $\Delta F_{\mathrm{r}\varphi}$ and $\Delta F_{\vartheta\varphi}$, are generated by the condensate and are obtained from the numerical solution. These terms describe the magnetic field,

$$\Delta\mathcal{B} = \frac{1}{\sqrt{-\mathrm{g}}}(\Delta F_{\vartheta\varphi}\partial_\mathrm{r} + \Delta F_{\varphi\mathrm{r}}\partial_\vartheta). \tag{9.31}$$

The azimuthal current density J^φ is given by

$$4\pi\sqrt{-\mathrm{g}}J^\varphi = \partial_\mathrm{r}(\sqrt{-\mathrm{g}}F^{\varphi\mathrm{r}}) + \partial_\vartheta(\sqrt{-\mathrm{g}}F^{\varphi\vartheta}). \tag{9.32}$$

The current density changes sign across the equatorial plane and thus can be viewed as describing two distinct currents: one negative (for $n > 0$) in the upper hemisphere and one positive in the lower hemisphere. As a result, two loops of oppositely directed azimuthal currents emerge. Together, these currents support the field $\Delta\mathcal{B}$, whose numerical profile is shown in Fig. 16 (left panel). This field is purely solenoidal, winding around regions where the currents attain extremal values. The red spot in the upper half-space marks a negative extremum of the upper current, while the blue spot in the lower half-space indicates a positive extremum of the lower current.

The field $\Delta\mathcal{B}$ resembles that of a finite segment of a vortex oriented upward in the upper half-space and a similar vortex oriented downward in the lower half-space.

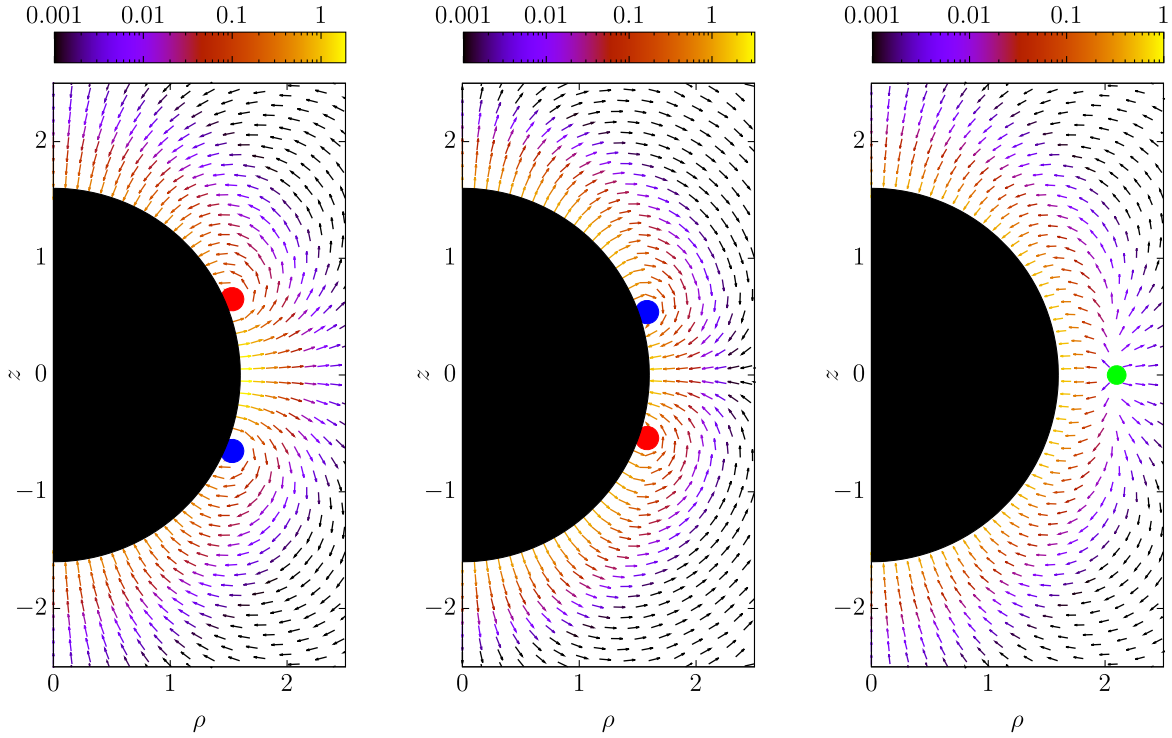


FIG. 16. Profiles of the 't Hooft magnetic field $\Delta\mathcal{B}$ (left), the 't Hooft massive magnetic field $\mathcal{B}_Z$ (center), and the Nambu magnetic field $\Delta\mathcal{B}$ (right) for the nonextremal hairy black hole with $n = 10$, $\mathrm{r_H} = 1.6$ and $\kappa = 10^{-3}$. In the first two panels, the blue and red (online) spots indicate, respectively, regions of positive and negative azimuthal currents, J^φ and J^φ_Z. In the third panel, the green spot marks the location of the maximal magnetic charge density $\tilde{\mathcal{J}}^0$. The field strength is represented by the arrow color.

Each vortex originates at the horizon in the polar region, extends outward, and eventually returns back to the horizon in the equatorial region.

When superposed with the background magnetic field $P\sin\vartheta d\vartheta\wedge d\varphi$, the field $\Delta\mathcal{B}$ exhibits an antiscreening effect: it enhances the background field in the equatorial region, where the condensate density $\sqrt{\psi_{\mu\nu}\psi^{\mu\nu}}$ is maximal, and screens the background field along the axis, where the condensate density vanishes. While the vortices do not change the total magnetic flux $4\pi P$, they redistribute it, making it inhomogeneous.

Integrating the current density (9.32) over a slice $\mathrm{r}\in[\mathrm{r_H},\infty)$, $\vartheta\in[0,\pi/2]$, with $\varphi=\mathrm{const}$ [compare with (2.49)] yields the total current in the upper half-space:

$$4\pi I_+ = 4\pi\int_{\mathrm{r_H}}^{\infty}d\mathrm{r}\int_0^{\pi/2}d\vartheta\sqrt{-\mathrm{g}}J^{\varphi} = \int_0^{\pi/2}d\vartheta\sqrt{-\mathrm{g}}F^{\varphi\mathrm{r}}\Big|_{\mathrm{r}=\mathrm{r_H}}^{\mathrm{r}=\infty}+\int_{\mathrm{r_H}}^{\infty}d\mathrm{r}\sqrt{-\mathrm{g}}F^{\varphi\vartheta}\Big|_{\vartheta=0}^{\vartheta=\pi/2}. \tag{9.33}$$

A similar computation in the lower half-space yields the current $I_-=-I_+$.

The dependence of I_+ on $\mathrm{r_H}$ is shown in Fig. 15. It vanishes when the solutions lose hair and bifurcate with the RN configuration, and it reaches its maximal amplitude in the extremal limit.

The direction of the currents depends on the sign of n:

$$I_\pm = \mp\frac{n}{|n|}|I_+|. \tag{9.34}$$

Thus, for $P=n/(2e)>0$, the current I_+ is always negative [see Fig. 15], meaning it flows opposite to the φ direction, whereas the current I_- is positive, flowing along the φ direction. This result is consistent with the perturbative limit [see Eq. (6.21) and Appendix C].

The central panel of Fig. 16 shows the profile of the massive magnetic field,

$$\mathcal{B}_Z=\frac{1}{\sqrt{-\mathrm{g}}}(Z_{\vartheta\varphi}\partial_{\mathrm{r}}+Z_{\varphi\mathrm{r}}\partial_\vartheta). \tag{9.35}$$

This time, there is no need to subtract the value in the absence of the condensate because it is zero. The profile is similar to that of $\Delta\mathcal{B}$, except that it flows in the opposite direction, since the Z field is sourced by $J^\mu_Z=(-g/g')J^\mu$. The vortex structure is now even more evident because the field $\mathcal{B}_Z$ is directed outward in the polar regions, resembling two vortices oriented upward and downward. The vortices wind around the currents and return back to the horizon in the equatorial region. The field strength decreases rapidly some distance away from the horizon, and the arrows in Fig. 16 become black where the field strength decreases by a factor of $\sim10^{-3}$. Both $\Delta\mathcal{B}$ and $\mathcal{B}_Z$ are purely radial at the horizon, and Fig. 17 (left panel) shows their horizon value, along with those for the current and condensate densities.

Although $J^\mu_Z=(-g/g')J^\mu$, meaning the extrema of the two currents coincide, the fields $\Delta\mathcal{B}$ and $\mathcal{B}_Z$ in Fig. 16 do not wind around exactly the same regions. This discrepancy arises because each field equation contains an additional term:

$$\partial_{\mathrm{r}}(\sqrt{-\mathrm{g}}\Delta F^{\varphi\mathrm{r}})+\partial_\vartheta(\sqrt{-\mathrm{g}}\Delta F^{\varphi\vartheta})=4\pi\sqrt{-\mathrm{g}}J^\varphi+\partial_\vartheta(\sqrt{-\mathrm{g}}P\sin\vartheta\mathrm{g}^{\vartheta\vartheta}g^{\varphi\varphi}),$$
$$\partial_{\mathrm{r}}(\sqrt{-\mathrm{g}}Z^{\varphi\mathrm{r}})+\partial_\vartheta(\sqrt{-\mathrm{g}}Z^{\varphi\vartheta})=4\pi\sqrt{-\mathrm{g}}J^\varphi_Z-\sqrt{-\mathrm{g}}\frac{(\Phi^\dagger\Phi)}{2}Z^\varphi. \tag{9.36}$$

To summarize, within the 't Hooft description, the electroweak condensate generates azimuthal currents that flow along the horizon. These currents create a magnetic field, which forms two vortices orthogonal to the horizon, anchored in the polar and equatorial regions. These vortices cause the magnetic field to become inhomogeneous, leading to the formations of the black hole "corona."

2. Nambu description

In the Nambu case, the massless and massive magnetic fields are given by

$$\mathcal{B}^i=\frac{1}{2\sqrt{-\mathrm{g}}}\epsilon^{ijk}\mathcal{F}_{jk},\qquad \mathcal{B}^i_{\mathcal{Z}}=\frac{1}{2\sqrt{-\mathrm{g}}}\epsilon^{ijk}\mathcal{Z}_{jk}. \tag{9.37}$$

These fields are not purely solenoidal, as their divergences do not vanish [see Eq. (2.51)]:

$$\nabla_k\mathcal{B}^k=\frac{e}{2\sqrt{-\mathrm{g}}}\epsilon^{ijk}\partial_i\psi_{jk},\qquad \nabla_k\mathcal{B}^k_{\mathcal{Z}}=-\frac{g^2}{2\sqrt{-\mathrm{g}}}\epsilon^{ijk}\partial_i\psi_{jk}. \tag{9.38}$$

The Nambu field generated by the condensate, $\Delta\mathcal{B}$, is defined similarly to the previous case, with the substitution $F\to\mathcal{F}$ in Eqs. (9.30) and (9.31).

As seen in the right panel of Fig. 16, the field $\Delta\mathcal{B}$ emanates from the region where the magnetic charge density is maximal [green spot in the figure] and then converges to the horizon. Thus, taking into account the rotational invariance, the magnetic charge P_{h} is distributed over a ring—a toroidal region outside the event horizon. This ring is especially pronounced in the extremal limit, as represented by the green area in Fig. 21 below, where the level surfaces of $\sqrt{-\mathrm{g}}\tilde{J}^0$ are

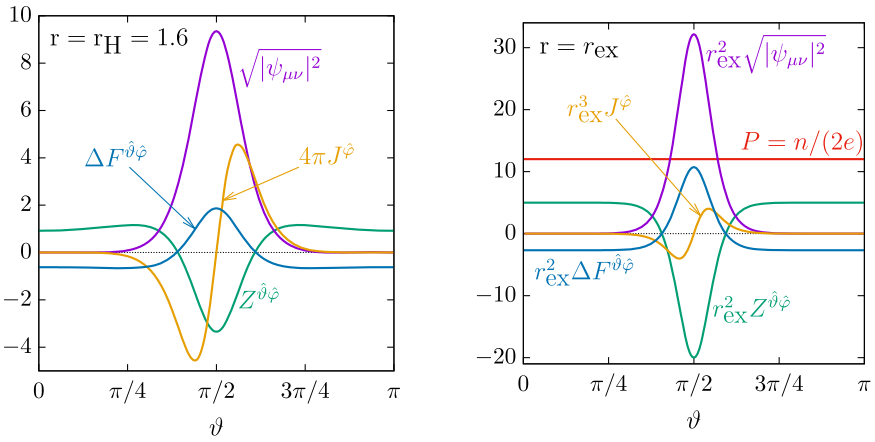


FIG. 17. The horizon values of the 't Hooft fields, current density, and condensate for the nonextremal hairy solution with $n = 10$, $r_H = 1.6$, and $\kappa = 10^{-3}$ (left) and for the extremal solution with $n = 10$ (right). The hatted indices denote projections on vectors of the orthonormal tetrad.

shown. The magnetic field created by the ring produces a *negative* flux through the horizon, ensuring that the latter contains only a part of the total magnetic charge.

The Nambu field also contains a solenoidal part associated with the electric current, defined by $\nabla_k \mathcal{F}^{ik} = 4\pi \mathcal{J}^i$. However, a similar relation for a $\mathcal{Z}$ current, analogous to that in (6.8), cannot be obtained since this would require a potential for $\mathcal{B}_{\mathcal{Z}}$, which does not exist since $\nabla_k \mathcal{B}^k_{\mathcal{Z}} \neq 0$. A potential for $\mathcal{B}$ does not exist either, but the current $\mathcal{J}$ is defined without the use of a potential.

The current density forms two rings of oppositely directed currents, which "sandwich" the magnetically charged ring [see Fig. 21]. The effect of the Nambu currents is subleading compared to that of the magnetic charge density. As seen in Fig. 15, the integrated current $\mathcal{I}_+$ is much weaker than the 't Hooft current I_+.

One should note that the curve $\mathcal{I}_+(r_H)$ in Fig. 15 differs from that shown in Fig. 3 of our previous report [57]. The difference arises because $\mathcal{I}_+$ in [57] was evaluated using the surface integral, the same one as in the first line in (9.33) but with $J^\varphi \to \mathcal{J}^\varphi$, which contains second derivatives, leading to large numerical errors. Using instead the contour integrals as in the second line in (9.33) increases the precision, yielding $\mathcal{I}_+(r_H)$ shown in Fig. 15. On the contrary, to compute the 't Hooft current $I_+(r_H)$, we always use the contour integral.

Summarizing, within the 't Hooft approach, all the magnetic charge is contained inside the black hole. However, there are strong azimuthal currents in the condensate that generate a corona made of vortices. In contrast, within the Nambu description, a portion of the magnetic charge is contained in a ring outside the horizon, which generates a magnetic field which "imitates" the vortex structure, as can be seen by comparing the left and right panels in Fig. 16.

X. EXTREMAL SOLUTIONS

The extremal hairy black holes are particularly interesting because, as argued by Maldacena, the presence of the corona should enhance the evaporation rate, causing nonextremal black holes to quickly relax to the extremal state with zero Hawking temperature [46]. For this reason, we discuss the extremal solutions in more detail.

Hairy black hole configurations are squashed toward the equatorial plane. However, as shown in Fig. 15, the horizon oblateness δ vanishes in the extremal limit, indicating that the horizon becomes spherical—provided the black hole charge is not too large.

Specifically, the extremal solutions exhibit two distinct phases depending on the value of their charge, $Q = \sqrt{\kappa/2} \times n/(2e) \approx 0.85\sqrt{\kappa} n$, in comparison to the critical value,

$$Q_\star \approx 0.62 Q_m = \frac{0.62}{2g\sqrt{\Lambda}} \approx \frac{0.72}{\sqrt{\kappa}}. \tag{10.1}$$

If $|Q| < Q_\star$ (or equivalently, $|n| < 0.85/\kappa$), the horizon remains spherical, and its oblateness δ vanishes. In this case, the horizon geometry coincides with that of the extremal RNdS solution (3.25). We refer to this regime as phase I.

For $|Q| > Q_\star$, the oblateness becomes nonzero, $\delta > 0$, and the horizon takes on an oblate shape, so the horizon geometry is no longer that of the RNdS solution. We refer to this regime as phase II.

Thus, the horizon oblateness δ serves as the order parameter for this phase transition. The parameter Q_m in (10.1) is the same as in (3.24), but it does not represent the maximum charge for extremal hairy solutions. Instead, in (10.1) and throughout the discussion below, Q_m is used as a natural scale for the charge.

The nonextremal solutions were obtained in the gauge (8.1), where $N(r) = 1 - r_H/r$. However, the fields in this gauge become unbounded in the extremal limit. To study the extremal case, we therefore switch to the radial gauge (8.2), where $N(r) \sim (1 - r_H/r)^2$. In this gauge, the horizon becomes degenerate, and the surface gravity vanishes. As explained in Appendix B, in the extremal case the size parameter r_H no longer distinguishes between different solutions, but rather corresponds to different radial gauges of the same solution.

In phase I, where the horizon geometry coincides with that of the extremal RNdS solution, we use the gauge (8.2) with $r_H = r_{ex}$, where r_{ex} is the radius of the extremal RNdS solution, determined by (3.23). With this choice, the radial coordinate r coincides with the Schwarzschild coordinate r at the horizon, and the function N(r) matches the near-horizon behavior of $N(r)$ for the extremal RNdS solution in (3.25). The horizon area is then given by $A_H = 4\pi r_{ex}^2$. Since the value of r_H is fixed, the only remaining essential physical parameter for extremal solutions is the charge n.

In phase II, the horizon geometry is no longer spherical. Moreover, the value of r_{ex}, as defined by Eq. (3.24), becomes complex if the charge is large, for $|Q| > Q_m$. Therefore, we abandon the condition $r_H = r_{ex}$ and instead use the gauge (8.2) with $r_H = 0.2$.

Below, we provide a detailed description of extremal hairy solutions in phases I and II.

A. Phase I: Spherical horizon, $|Q| < Q_\star$

If the total magnetic charge of the extremal black hole is not too large such that $|n| < 0.85/\kappa$, then the hypermagnetic field is strong enough to create around the horizon a bubble of false vacuum where $W^a_{\mu\nu} \approx 0$, $\Phi \approx 0$ and the electroweak symmetry is restored.

These field values are the same as those for the extremal RNdS solution (3.25). Moreover, as shown in Fig. 15, the horizon oblateness vanishes in the extremal limit, indicating that the horizon geometry is spherically symmetric—just as in the extremal RNdS case. Therefore, the field configuration approaches the extremal RNdS solution at the horizon, with radius r_{ex} determined by (3.23), and we accordingly set $r_H = r_{ex}$ in Eq. (8.2).

Since $r_H = r_h = r_{ex} \approx g|Q| \approx 0.75\sqrt{\kappa}|n|$, thus, according to (3.22), the horizon value of the hypermagnetic field is

$$|B(r_h)| = \frac{|n|}{2r_h^2} \approx \frac{0.89}{\kappa|n|}; \tag{10.2}$$

therefore, $|B(r_h)| > m_H^2$ in phase I.

The bubble of symmetric phase extends up to $r \approx r_b$, where $|B(r_b)| \approx m_H^2$, which occurs at $r_b \approx \sqrt{|n|/\beta} \approx 0.73\sqrt{|n|}$. This corresponds to the yellow area in the left panel of Fig. 20 below. The Higgs field is very close to zero in this region, and, as explained in Appendix E, it can be approximated by

$$\phi_1 \approx \left(\frac{r - r_{ex}}{r_{ex}}\right)^{\sigma/\lambda} S_1(\vartheta), \qquad \phi_2 \approx \left(\frac{r - r_{ex}}{r_{ex}}\right)^{\sigma/\lambda} S_2(\vartheta), \tag{10.3}$$

where $\lambda, \sigma, S_1, S_2$ are defined by (E5) and (E13)–(E15). Let us now analyze the situation from two different perspectives: the approaches of 't Hooft and of Nambu.

1. Structure of vortices forming the corona

Within the 't Hooft definition, the electromagnetic and Z fields are defined by Eqs. (2.35)–(2.38). They admit potentials (2.38) whose nonzero components are only azimuthal; hence $F_{j\varphi} = \partial_j A_\varphi$ and $Z_{j\varphi} = \partial_j Z_\varphi$. Subtracting from F_{ik} the background contribution, that is $P \sin\vartheta d\vartheta \wedge d\varphi = -d(P\cos\vartheta d\varphi)$, and using the definition of the magnetic field in Eq. (2.44) yield

$$\sqrt{-g}\Delta\mathcal{B}^i = \epsilon^{ij\varphi}\partial_j(A_\varphi + P\cos\vartheta), \quad \sqrt{-g}\mathcal{B}^i_Z = \epsilon^{ij\varphi}\partial_j Z_\varphi. \tag{10.4}$$

It follows that field lines of $\sqrt{-g}\Delta\mathcal{B}^k$ and $\sqrt{-g}\mathcal{B}^k_Z$ coincide with the level lines of $\Delta A_\varphi = A_\varphi + P\cos\vartheta$ and Z_φ shown in Fig. 18. They also coincide with lines of $\Delta\mathcal{B}^k$ and $\mathcal{B}^k_Z$. A disadvantage of this representation is that the density of field lines reduces in the polar regions where the factor $\sqrt{-g}$ approaches zero, whereas the actual values of the fields $\Delta\mathcal{B}^k$ and $\mathcal{B}^k_Z$ are not small at the poles, as seen in Fig. 16.

Nevertheless, Fig. 18 clearly shows the structure of the black hole corona, consisting of two vortices: one in the upper hemisphere (colored in blue) and the other in the lower hemisphere (colored in red).

Each vortex starts in the polar region, extends outward, and then returns to the horizon in the equatorial region. Therefore, each vortex forms loops attached to the horizon by both ends. This is reminiscent of the coronal loops in the solar atmosphere formed by the prominences. However, unlike the latter, each vortex is not a localized jet but spreads out in all azimuthal directions, like a fountain, before returning to the horizon.

The vortices carry fluxes, but since they leave the horizon and then return, the total flux through the horizon is zero (excluding the background contribution $4\pi P$).

Each vortex carries a magnetic dipole moment, and the vortices in the upper and lower hemispheres can be viewed as two magnetic dipoles oriented against each other so that the total dipole moment vanishes (but not the quadrupole moment).

The vortices mutually repel, which is why the field lines are squeezed when approaching the equatorial region.

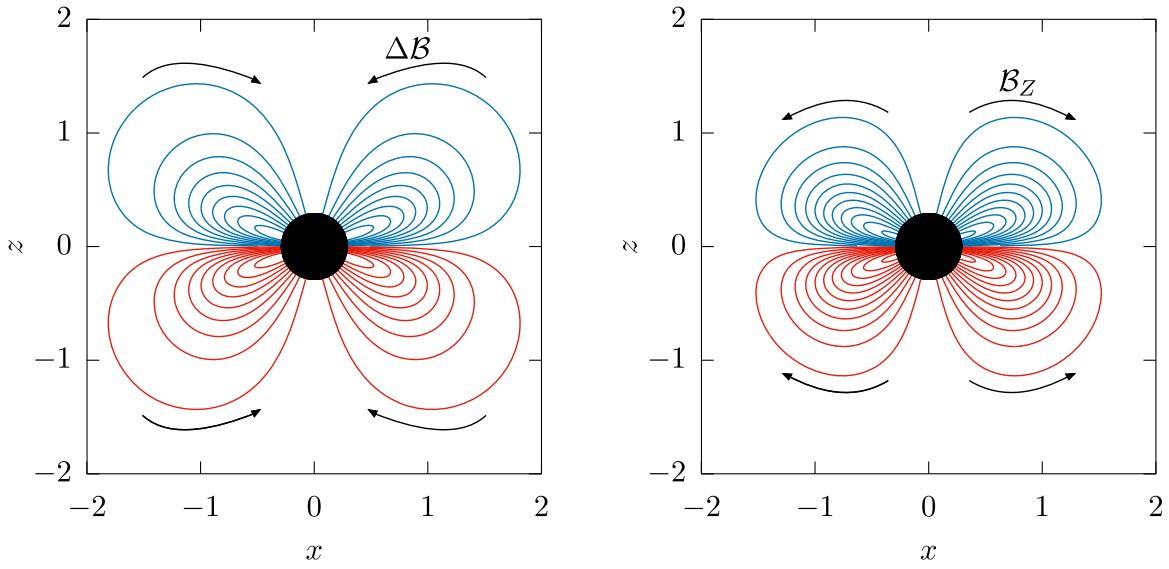


FIG. 18. Electroweak corona around the black hole: the level lines of $\Delta A_\varphi = A_\varphi + P\cos\vartheta$ (left) and of Z_φ (right) in "Cartesian" coordinates $x = \pm \mathrm{r}\sin\vartheta$, $z = \mathrm{r}\cos\vartheta$ for the extremal hairy solution with $n = 10$ and $\kappa = 10^{-3}$. They coincide, respectively, with the field lines of $\sqrt{-\mathrm{g}}\Delta\mathcal{B}^k$ and $\sqrt{-\mathrm{g}}\mathcal{B}^k_Z$, and with those of $\Delta\mathcal{B}^k$ and $\mathcal{B}^k_Z$. The arrows show the direction of the fields.

2. Vortex fluxes and the similarity with Nambu strings

The fluxes carried by vortices can be evaluated analytically for the extremal solutions. Specifically, the near-horizon behavior of the Higgs field expressed by Eq. (10.3) implies that the unit vector $n^a = (\Phi^\dagger\tau^a\Phi)/(\Phi^\dagger\Phi)$ depends on ϑ but is independent of r (within the lowest perturbative order).

Using this information in (2.26)–(2.37), one can evaluate the nonzero components of the condensate density and magnetic field at the horizon (see Appendix E):

$$-e\psi_{\vartheta\varphi} = g'^2\frac{n}{2e}\times\frac{|n|\left(\sin\frac{\vartheta}{2}\cos\frac{\vartheta}{2}\right)^{|n|-1}}{\left[\left(\cos\frac{\vartheta}{2}\right)^{|n|}+\left(\sin\frac{\vartheta}{2}\right)^{|n|}\right]^2},$$
$$F_{\vartheta\varphi} = g^2\frac{n}{2e}\sin\vartheta - e\psi_{\vartheta\varphi}. \tag{10.5}$$

It is worth noting that, introducing $\mathrm{t} = \tan(\vartheta/2)$, one has

$$g^2\psi_{\vartheta\varphi} = n\frac{d}{d\vartheta}\left(\frac{1}{1+\mathrm{t}^{|n|}}\right). \tag{10.6}$$

The derivative of $F_{\vartheta\varphi}$ determines the horizon value of the current density J_φ [see Eq. (E23)]. The flux of $F_{\vartheta\varphi}$ through the horizon is $4\pi P = 4\pi\times n/(2e)$.

One can split the electromagnetic field as in (9.30),

$$F_{\vartheta\varphi} = P\,\sin\vartheta + \Delta F_{\vartheta\varphi}, \tag{10.7}$$

where the first term on the right can be associated with the charge contained inside the black hole, while the second term can be interpreted as the magnetic field created by the condensate. One has

$$\Delta F_{\vartheta\varphi} = -\frac{g'^2}{e}Z_{\vartheta\varphi}, \qquad Z_{\vartheta\varphi} = \frac{n}{2}\sin\vartheta + g^2\psi_{\vartheta\varphi}. \tag{10.8}$$

The total fluxes of $\Delta F_{\vartheta\varphi}$ and $Z_{\vartheta\varphi}$ through the horizon vanish, but locally they are not zero because $\Delta F_{\vartheta\varphi}$ and $Z_{\vartheta\varphi}$ are sign definite in the polar regions where $0 < \vartheta < \vartheta_0$ and $\pi - \vartheta_0 < \vartheta < \pi$ [see Fig. 17, right panel]. They change sign at $\vartheta = \vartheta_0$, $\vartheta = \pi - \vartheta_0$, where

$$Z_{\vartheta\varphi}(\vartheta_0) = 0. \tag{10.9}$$

To analyze this condition, we use (10.6) and (10.8), which yields

$$Z_{\vartheta\varphi} = n\frac{d}{d\vartheta}\left(\frac{1}{1+\mathrm{t}^{|n|}}-\frac{1}{1+\mathrm{t}^2}\right)$$
$$= n(1+\mathrm{t}^2)\left(\frac{\mathrm{t}}{(1+\mathrm{t}^2)^2}-\frac{|n|}{2}\frac{\mathrm{t}^{|n|-1}}{(1+\mathrm{t}^{|n|})^2}\right); \tag{10.10}$$

hence $Z_{\vartheta\varphi}$ changes sign at the point where

$$\mathrm{t} = \left(\sqrt{\frac{2}{|n|}}\frac{1+\mathrm{t}^{|n|}}{1+\mathrm{t}^2}\right)^{2/(|n|-2)}. \tag{10.11}$$

This equation can be solved by iterations, which gives a value $\mathrm{t} = \mathrm{t}_0(|n|)$. In the large $|n|$ limit, one has $\mathrm{t}_0 \to 1$, whereas $(\mathrm{t}_0)^{|n|} \to 0$. It follows then from (10.11) that $2|n|\mathrm{t}_0^{|n|} \to 1$; therefore

$$\mathrm{t}_0 = 1 - \frac{\ln(2|n|)}{|n|} + \ldots \;\Rightarrow\; \vartheta_0 = \frac{\pi}{2} - \frac{\ln(2|n|)}{|n|} + \ldots, \tag{10.12}$$

the dots denoting subleading terms. As a result, the point ϑ_0 where the Z field changes sign approaches equator for large $|n|$. The flux through the northern polar region is

$$\Psi_Z = 2\pi \int_0^{\vartheta_0} Z_{\vartheta\varphi} d\vartheta = 2\pi n c(n), \tag{10.13}$$

where

$$c(n) = \frac{\mathrm{t}_0^2 - \mathrm{t}_0^{|n|}}{(1+\mathrm{t}_0^2)(1+\mathrm{t}_0^{|n|})}. \tag{10.14}$$

This is a monotonous function of $|n|$, such that $c(2) = 0$, $c(4) \approx 0.15$, and $c(n) \to 1/2$ for $|n| \to \infty$. This gives the fluxes leaving the horizon in the polar region:

$$\Psi_Z = +4\pi c(n) \times \frac{n}{2},$$
$$\Psi_F = -4\pi g'^2 c(n) \times \frac{n}{2e} = -4\pi g'^2 c(n) P. \tag{10.15}$$

Integrating over the equatorial region where $\vartheta_0 < \vartheta < \pi/2$ yields the same values, up to the sign, because fluxes leaving the horizon are the opposite of those entering the horizon.

Similarly, one obtains the fluxes in the southern hemisphere, which are the same due to the invariance of the system under the reflection $\vartheta \to \pi - \vartheta$.

The vortex fluxes arise from the electroweak condensation triggered by the background magnetic field. Using the value of the background flux through the northern hemisphere, $\Psi_F^0 \equiv 2\pi P = \pi n/e$, one can *define* the magnetic susceptibility as the ratio of the flux carried by the vortex to the background flux,

$$\Upsilon(n) = \Psi_F/\Psi_F^0 = -2g'^2 c(n). \tag{10.16}$$

The factor $c(n)$ has a geometrical origin because the vortices exist on top of the horizon which is not flat but spherical. The horizon radius increases with $|n|$, and therefore, for large $|n|$, the horizon locally approaches a plane, whereas $c(n) \to 1/2$. Therefore, for large $|n|$, one has $\Upsilon(n) \to -g'^2$ [diamagnetism], whereas the fluxes carried by each vortex are

$$\Psi_Z = \pi n, \qquad \Psi_F = -\pi n \times \frac{g'^2}{e}. \tag{10.17}$$

The value $\Psi_F/\Psi_Z = -g'^2/e$ is explained by the fact that the Z field is massless close to the horizon; hence it is proportional to the F field of the vortex, because the two fields are sourced by proportional currents J^μ and J_Z^μ whose ratio is $-g'/g = -g'^2/e$ [see Eqs. (6.8a) and (6.8b)].

It is interesting to compare the fluxes (10.17) with those of other known electroweak vortices reviewed in Appendix F. By setting $n = -4m$, the value of Ψ_F matches that in Eq. (F34), which corresponds to the chiral string—a Z string with a condensate in its core. Therefore, horizon vortices are similar to chiral strings.

As shown in Appendix F, the chiral string closely resembles the Nambu string, which terminates at the Nambu monopole [61]. The chiral string exhibits exactly the same Nambu fluxes (F35) as the Nambu string, and it carries the flux Ψ_F proportional to g'^2/e, similarly to the flux produced by the Nambu monopole. This suggests that the Nambu string can be identified with the chiral string (rather than with the Z string as is often assumed in the literature). Therefore, being similar to chiral strings, the horizon vortices are similar to Nambu strings. This analogy is actually quite natural, since the charge P_{h} contained in the hair is a multiple of the g'^2/e.

At the same time, the similarity cannot be complete, because Nambu/chiral strings interpolate along the orthogonal direction between the symmetric and broken phases, whereas for horizon vortices, the orthogonal direction lies along the horizon, where the system remains entirely in the symmetric phase. We now proceed to discuss this aspect in more detail.

3. The origin of vortices within the symmetric phase

The nonextremal hairy black holes carry the hypermagnetic field that creates an electroweak condensate, giving rise to vortices. The condensate is made of fields that are massive because the gauge symmetry is broken. The spherical symmetry is broken as well.

For the extremal solutions, both the electroweak symmetry and spherical symmetry are restored at the horizon. The geometry there is perfectly spherical; the SU(2) field strength and the Higgs field vanish, while the hypercharge field is spherically symmetric, $B = (n/2)\sin\vartheta d\vartheta \wedge d\varphi$. However, the F and Z fields are nonspherical and form vortices, whose horizon values are described by the above formulas. According to our numerics, their amplitudes are maximal at the horizon, where the condensate density also reaches its maximal value (see Fig. 19). How can this be, and what plays the role of the condensate responsible for vortex formation?

In fact, a similar issue has already been analyzed in flat space in Refs. [84,85]. It was found that, assuming the unitary gauge and approaching the symmetric phase, where $|\mathrm{B}| > m_{\mathrm{H}}^2$ and $\Phi = \mathrm{W}_{\mu\nu}^a = 0$, the SU(2) field potential W_μ^a is not zero but corresponds to a nontrivial "twisted" pure gauge. It is this pure gauge that plays the role of a *massless* condensate, rendering the F, Z fluxes inhomogeneous and creating vortices even in the symmetric phase.

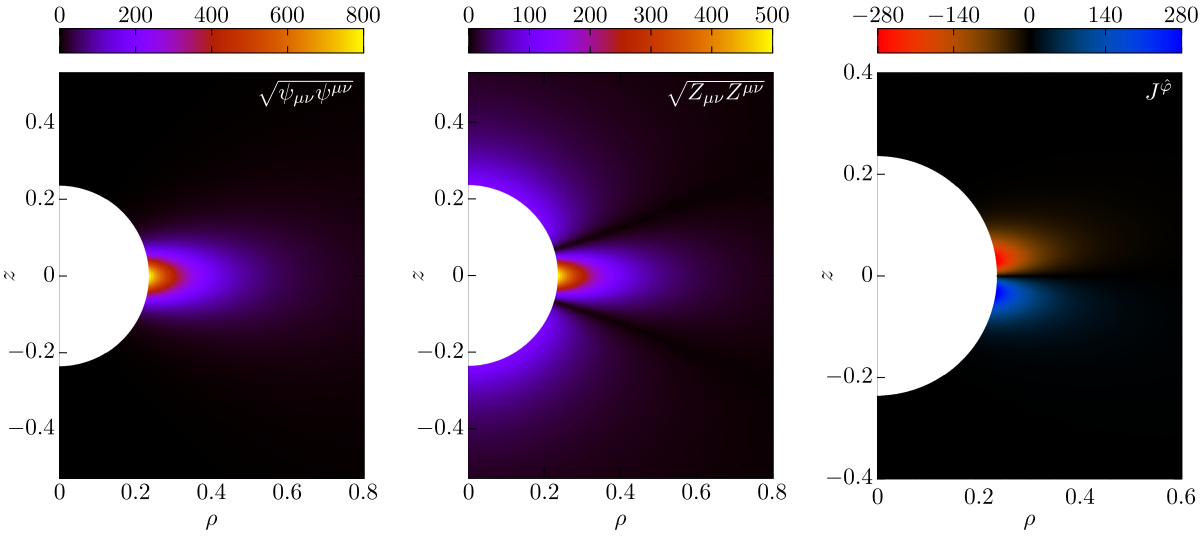


FIG. 19. The norms of the condensate $\sqrt{\psi_{\mu\nu}\psi^{\mu\nu}}$ (left), of the Z field $\sqrt{Z_{\mu\nu}Z^{\mu\nu}}$ (center), and the azimuthal current density $J^{\hat{\varphi}}$ (right) for the extremal solutions with $n = 10$ and $\kappa = 10^{-3}$.

This is precisely what happens in our case. At the horizon, where $\mathrm{W}^a_{\mu\nu} = 0$, Eqs. (2.26) and (2.37) yield

$$F_{ik} = \frac{g^2}{e}B_{ik} - e\psi_{ik}, \qquad Z_{ik} = B_{ik} + g^2\psi_{ik}, \tag{10.18}$$

where the condensate field ψ_{ik} is not spherically symmetric [see Eq. (10.5)], although the horizon geometry is.

The tensor $\psi_{\mu\nu}$ is given by the gauge invariant expression (2.35). Let us first consider the gauge (7.29)–(7.31), in which W^a_μ vanishes at the horizon. Then Eq. (2.35) reduces at the horizon to

$$g^2\psi_{ik} = -\epsilon_{abc}n^a\partial_i n^b\partial_k n^c, \tag{10.19}$$

where n^a is the $\Phi \to 0$ limit of $(\Phi^\dagger\tau^a\Phi)/(\Phi^\dagger\Phi)$. Using Φ given by Eq. (7.31) with ϕ_1, ϕ_2 from (10.3) yields

$$n^a = \frac{(S_1)^2 - (S_2)^2}{(S_1)^2 + (S_2)^2}e^a_r + \frac{2S_1S_2}{(S_1)^2 + (S_2)^2}e^a_\vartheta, \tag{10.20}$$

with unit vectors e^a_r, e^a_ϑ defined in (7.30) and $S_1(\vartheta), S_2(\vartheta)$ given by (E13) and (E14). Inserting this into (10.19) and using the relation $\nu = -n/2$ yields exactly the same components of the condensate density $\psi_{\vartheta\varphi} = -\psi_{\varphi\vartheta}$ as in (10.5).

One notices that ψ_{ik} in (10.19) is proportional to the volume form on the two-sphere spanned by the unit vector n^a. When ϑ, φ run over the horizon, the unit vector n^a spans the two-sphere $(-\nu)$ times, where the minus sign arises because n^a runs in the opposite direction, since one has $n^a = \mp\delta^a_3$ for $\vartheta = 0, \pi$, respectively. This corresponds to the "twist" of the condensate.

The horizon flux of ψ_{ik} is therefore proportional to $(-\nu) \times 4\pi$,

$$e\oint \psi_{\vartheta\varphi}d\vartheta d\varphi = -e \times \frac{(-\nu)\times 4\pi}{g^2} = e \times \frac{4\pi\nu}{g^2} = -g^2 \times 4\pi\frac{n}{2e} = -4\pi g^2 P. \tag{10.21}$$

This reproduces Eq. (E20) in Appendix E and ensures that the flux of $F_{\vartheta\varphi}$, defined according to (10.18), is equal to $4\pi P$, while the flux of $Z_{\vartheta\varphi}$ is zero.

However, the gauge in which W^a_μ vanishes at the horizon is not unitary. The Higgs field is given in this gauge by Eq. (7.31), where both the lower and upper components do not vanish, although they approach zero at the horizon. To pass to the unitary gauge where $\Phi = (0, \phi)^{\mathrm{T}}$, one can first apply the transformation inverse to that in (7.28), which brings the fields back to the form (7.22), where $\Phi = (\phi_1, \phi_2)^{\mathrm{T}}$.

Next, one applies another gauge transformation generated by $\exp(2i\alpha\mathrm{T}_2)$, whose effect on the upper component of the Higgs field is $\phi_1 \to \tilde{\phi}_1 = \phi_1\cos\alpha + \phi_2\sin\alpha$. Requiring that $\tilde{\phi}_1 = 0$ yields

$$\tan(\alpha) = -\frac{\phi_1}{\phi_2} = -\frac{S_1(\vartheta)}{S_2(\vartheta)} = \frac{2}{|\nu|+1}\frac{S_2'(\vartheta)}{S_2(\vartheta)} = \mathrm{t}\frac{\mathrm{t}^{|\nu|-1}-1}{\mathrm{t}^{|\nu|+1}+1}, \tag{10.22}$$

with $\mathrm{t} = \tan(\vartheta/2)$, and we used the formula (10.3) for the Higgs field in the horizon vicinity, and also Eqs. (E13) and (E14) from Appendix E.

As a result, the gauge transformation bringing the fields (7.29)–(7.31) to the unitary gauge is generated by

$$\mathfrak{V} = e^{i(\vartheta+2\alpha)\mathrm{T}_2} e^{i\nu\varphi\mathrm{T}_3} \tag{10.23}$$

[we have omitted the U(1) part]. The horizon value of the SU(2) field in this gauge is

$$\begin{aligned} \mathrm{T}_a \mathrm{W}^a_\mu dx^\mu &= i\mathfrak{V}\partial_\mu \mathfrak{V}^{-1} dx^\mu \\ &= \mathrm{T}_2 d(2\alpha+\vartheta) + \nu\{\cos(2\alpha+\vartheta)\mathrm{T}_3 \\ &\quad - \sin(2\alpha+\vartheta)\mathrm{T}_1\} d\varphi. \end{aligned} \tag{10.24}$$

Since in the unitary gauge we have $n^a = -\delta^a_3$, the formula (2.35) reduces to (2.40) and yields

$$\begin{aligned} g^2 \psi_{\vartheta\varphi} &= \mathrm{W}^1_\vartheta \mathrm{W}^2_\varphi - \mathrm{W}^1_\varphi \mathrm{W}^2_\vartheta = -\nu(\cos(2\alpha+\vartheta))' \\ &= n \frac{d}{d\vartheta}\left(\frac{1}{1+\mathrm{t}^{|n|}}\right), \end{aligned} \tag{10.25}$$

which precisely agrees with (10.6). Therefore, the condensate density ψ_{ik} responsible for the vortex formation within the symmetric phase can be viewed as a nontrivial pure gauge, in agreement with [84,85].

To recapitulate, in the gauge defined by Eqs. (7.29) and (7.31), one has $\mathrm{W}^a_\mu = 0$ at the horizon, but the condensate is supported by the nontrivial angular dependence of the unit vector n^a in Eq. (10.20). Upon passing to the unitary gauge, the unit vector n^a becomes trivial, while W^a_μ becomes the pure gauge configuration given by Eq. (10.24), inheriting the nontrivial angular dependence.

4. Agreement between the different descriptions

One more issue remains to be addressed. The equatorial region, where the vortices converge back to the horizon, $\vartheta_0 \le \vartheta \le \pi - \vartheta_0$, is notably narrow: its width decreases as $\ln(|n|)/|n|$ when $|n|$ increases [see Eq. (10.12)]. At the same time, the fluxes (10.17) scale as $|n|$; hence the vortex fields in this region grow as $n^2/\ln(|n|)$. As illustrated in Fig. 18, the density of field lines becomes very large in the equatorial region. This has interesting consequences.

As mentioned above, horizon vortices bear a resemblance to Nambu strings. When the latter terminate, the magnetic flux Ψ_F trapped inside the string spreads outward from the termination point, generating a radial magnetic field that mimics a magnetic monopole with charge proportional to g'^2/e [61]. Based on this, Maldacena proposed that the black hole corona consists of vortices attached to the horizon at one end and terminating on monopoles some distance away, as depicted in Fig. 4(b) of [46]. This interpretation is supported by the Nambu description, which suggests that a portion of the magnetic charge resides outside the horizon.

At the same time, we know that the corona rather consists of vortex segments attached to the horizon at both ends, forming loops. This might appear to contradict the interpretation of [46]. However, it turns out that the two interpretations are not mutually exclusive and can, in fact, be reconciled.

Specifically, let us compute the outgoing flux through the equatorial region of the total magnetic field, which includes both the background contribution and the vortex field, i.e., $F_{\vartheta\varphi} = P\sin\vartheta + \Delta F_{\vartheta\varphi}$ [see Eq. (10.7)]. Assuming that $|n| \gg 1$ and using (10.12) and (10.17), we obtain

$$\begin{aligned} \Psi_{\text{equator}} &= 2\pi \int_{\vartheta_0}^{\pi-\vartheta_0} (P\sin\vartheta + \Delta F_{\vartheta\varphi}) d\vartheta = 4\pi P\cos(\vartheta_0) - 2\Psi_F \\ &= 4\pi P\left(g'^2 + \frac{\ln(2|n|)}{|n|} + \ldots\right) \approx 4\pi g'^2 P, \end{aligned} \tag{10.26}$$

where the dots denote subleading terms. Since the vortex field $\Delta F_{\vartheta\varphi}$ is very large, it provides the dominant contribution, while the effect of the background field $P\sin\vartheta$ is subleading.

As a result, the total flux emitted by the narrow equatorial region corresponds to that of a magnetic monopole with charge $g'^2 P \propto g'^2/e$, aligning with the interpretation of [46]. Owing to their strong confinement in the equatorial region, the vortex fields mimic an "effective" magnetic charge $g'^2 P$ at the horizon, even though within the 't Hooft framework, all of the charge remains confined inside the horizon.

This effective charge is not localized at a single point but is instead distributed along a ring formed by the intersection of the horizon and the equatorial plane, as the flux Ψ_{equator} remains uniform along the azimuthal direction. One can therefore interpret the equatorial region of the event horizon as being effectively charged. Remarkably, this aligns with the Nambu perspective, which posits that the $g'^2 P$ portion of the total magnetic charge P resides in a ring outside the horizon [see below]. As a result, what the Nambu approach considers to be the actual charge $g'^2 P$ is, in the 't Hooft approach, effectively mimicked by the distribution of field lines, producing an equivalent charge of the same strength. The only distinction lies in their locations: in the 't Hooft approach, the charge is located at the horizon, whereas in the Nambu approach, it resides some distance away—a point that will be discussed below.

It is instructive to revisit the perturbative picture shown in Fig. 6. The right panel illustrates the axially symmetric solution, where the yellow equatorial zone appears charged within the Nambu approach. We now understand that this picture extends beyond the perturbative regime, showing that the equatorial zone corresponds to the region of the horizon that is effectively charged within the 't Hooft framework.

The left panel in Fig. 6 depicts a nonsymmetric minimum energy solution. At present, we have not tried to extend this solution at the nonperturbative level. However, if such a generalization exists, then the six yellow zones in the figure should likewise become effectively charged regions of the horizon, corresponding to monopoles. Consequently, the nonperturbative extension of the nonsymmetric solution in Fig. 6 should feature eight vortices, interpolating between to the dark zones, where the field lines leave the horizon, and the six monopoles, where the field lines converge back.

These observations establish a connection between the 't Hooft perspective, according to which all the magnetic charge is confined within the black hole, and the Nambu perspective, which suggests that part of the charge resides outside. Furthermore, they provide a link between the interpretation of vortices proposed in [46] and our findings.

5. Summary of the 't Hooft description

Let us recapitulate everything said above. Within the 't Hooft description, the electroweak condensate around the black hole supports currents flowing along the horizon. The condensate and the current attain their maximal values at the horizon (see Fig. 19). These currents create vortices attached to the horizon at both ends, resembling the coronal loops in the Sun's atmosphere (see Fig. 18). The vortices originate in the polar regions of the horizon, extend outside, spread out like fountains, and eventually return back to the horizon in the equatorial region. These vortices carry a magnetic flux proportional to g'^2/e, similar to Nambu strings. The narrow equatorial region, where the vortices converge to the horizon, can be viewed as carrying an effective charge g'^2P, since the field strengths are significantly high there. The vortices collectively form the black hole corona, while the condensate and corona constitute together the black hole hair.

6. The magnetic ring, ADM mass, and the weakness of gravity

Within the Nambu description, the electroweak condensate around the black hole is magnetically charged. For extremal solutions in phase I, the condensate carries the charge g'^2P, which represents 22% of the total charge, the remaining 78% being contained inside the black hole [see Sec. IX B above].

Although the 't Hooft current density is maximal at the horizon, the Nambu current density and the magnetic charge density both vanish there. However, as seen in Fig. 20, the magnetic charge density $\sqrt{-g}\tilde{\mathcal{J}}^0$ and the Nambu current density $\mathcal{J}^{\hat{\varphi}}$ become nonzero and achieve maximal values some distance away from the horizon, where the Higgs field deviates from zero. Therefore, one may say that, in the 't Hooft description, the charge and current are located at the horizon, whereas in the Nambu description, they are situated some distance away from it.

The 3D profiles are shown in Fig. 21, where the central ring [green online] corresponds to the level surfaces of the magnetic charge density. This ring is sandwiched between two others [blue and red online] containing superconducting currents $\mathcal{I}_+$ and $\mathcal{I}_- = -\mathcal{I}_+$ represented in Fig. 21 by level surfaces of $\sqrt{-g}\mathcal{J}^\varphi$. The Nambu currents are, however, relatively weak, the absolute values of $\mathcal{I}_\pm$ being about 2 orders of magnitude smaller than those for the 't Hooft currents $I_\pm$ [see Fig. 22].

The condensate terminates where $|\mathrm{B}| \approx m_{\mathrm{W}}^2$, at $r_{\mathrm{c}} \approx \sqrt{|n|}/g \approx 1.13\sqrt{|n|}$. Still farther away, the configuration approaches the RN solution (3.6) and (3.7) whose ADM mass turns out to be *smaller* than the charge,

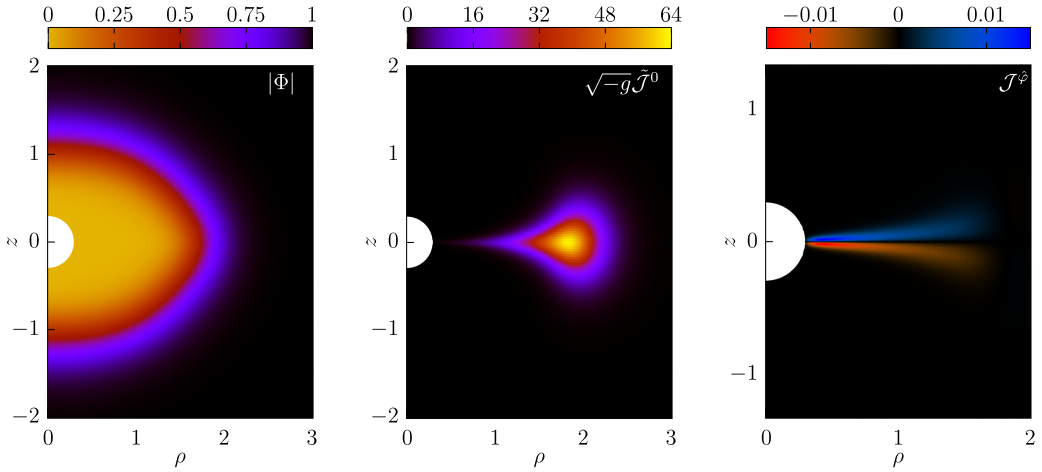


FIG. 20. The norm of the Higgs field $\sqrt{\Phi^\dagger\Phi}$ (left), the Nambu magnetic charge density $\sqrt{-g}\tilde{\mathcal{J}}^0$ (center), and the Nambu electric current density $\mathcal{J}^{\hat{\varphi}}$ (right) for the extremal solutions with $n = 40$ and $\kappa = 10^{-4}$.

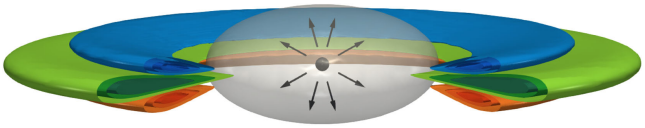


FIG. 21. The extremal solutions in phase I contain a small charged black hole inside a bubble of the symmetric phase (gray online), surrounded by a ring-shaped electroweak condensate supporting 22% of the total magnetic charge (green) and two opposite superconducting currents (blue and red). Farther away the condensate disappears and the magnetic field becomes Coulombian.

$$M < |Q|. \tag{10.27}$$

We have already observed this phenomenon in the spherically symmetric case [Sec. V B]. To repeat, the hair carries 22% of the total charge; hence its charge is $Q_{\rm h} = 0.22 \times Q$, but its mass $M_{\rm h}$ is small due to the negative Zeeman energy. This happens because the condensate contains charged W bosons whose interaction with the magnetic field of the black hole shifts their mass as $m_{\rm W}^2 \to m_{\rm W}^2 - |{\rm B}|$ [48]. As a result, one has $M_{\rm h} < |Q_{\rm h}|$, which explains (10.27).

If $|n|$ is not very large such that $|Q| \ll Q_\star$, then the mass-to-charge ratio for the hair is very small, $M_{\rm h}/|Q_{\rm h}| \sim \sqrt{\kappa} \ll 1$. For example, for $n = 2$, one has $M_{\rm h}/Q_{\rm h} \sim 10^{-16}$ [see the estimate below Eq. (5.16)]. The horizon contribution to the mass is then dominant, $M = M_{\rm H} + M_{\rm h} \approx M_{\rm H}$, where $M_{\rm H}$ is determined by (9.13) with $r_h = r_{\rm ex} \approx g|Q|$. One obtains in this case the same estimate as in (5.16),

$$M \approx r_h \approx g|Q| = 0.88 \times |Q|. \tag{10.28}$$

As $|n|$ increases, the ratio $M_{\rm h}/|Q_{\rm h}|$ also grows, and the estimate (10.28) ceases to be valid, but the inequality $M < |Q|$ continues to hold for all extremal solutions.

The smallness of the ratio $M_{\rm h}/|Q_{\rm h}|$ can be interpreted as a manifestation of the weak gravity conjecture [69]: gravity is the weakest force because the magnetic repulsion between the condensate and the black hole is stronger than the gravitational attraction. However, the condensate cannot be pushed away to infinity due to the Yukawa potential barrier at large distances, as the condensate consists of massive fields. The negative Zeeman energy renders the W bosons in the condensate almost massless, whereas the Z and Higgs bosons remain massive and follow the Yukawa law in the far field, which forces the condensate density to approach zero. As a result, the condensate remains exponentially localized in a region around the horizon. The massless corona extends beyond this region and approaches zero only polynomially, due to the presence of a magnetic quadrupole moment.

7. Solutions with $|Q| \ll Q_\star$ versus electroweak monopoles

We used in our numerics values of κ ranging between 10^{-10} and 10^{-2} since otherwise, it is challenging to achieve numerical convergence. Extrapolating our results to the physical value $\kappa \sim 10^{-33}$ then yields the following picture of extremal solutions with $|Q| \ll Q_\star$.

Their horizon size $r_{\rm ex} \approx 0.75\sqrt{\kappa}|n|$ is *parametrically* small compared to the size of the region where the massive fields change, $r_b \approx 0.73\sqrt{|n|} < r < r_c \approx 1.13\sqrt{|n|}$. Therefore, the tiny black hole does not gravitationally affect the electroweak configuration but only supports the strong hypermagnetic field, which is necessary to create the electroweak condensate. It also regularizes the energy of this field to a finite value, $M_{\rm H} \approx g|Q| \sim \sqrt{\kappa}, |n|$. The massive condensate resides far from the horizon, where the geometry is nearly flat. The condensate carries mass $M_{\rm h} \sim \kappa, |n|^{3/2}$ [as explained below after Eq. (10.34)], meaning the ratio $M_{\rm h}/\kappa$ remains finite as $\kappa \to 0$. This leads to the following consequence.

The dimensionful ADM mass in units of the electroweak mass scale is expressed by (2.24) and (2.25),

$$\mathbf{M} = \frac{e^2}{4\pi\alpha}\mathcal{M} \times \boldsymbol{m}_0, \tag{10.29}$$

where

$$\begin{aligned}\mathcal{M} &\equiv \frac{8\pi}{\kappa} \times M = \frac{8\pi}{\kappa} \times (M_{\rm H} + M_{\rm h}) \\ &= \frac{4\pi g|n|}{\sqrt{2\kappa}e} + \frac{8\pi}{\kappa}M_{\rm h} \equiv \mathcal{M}_{\rm H} + \mathcal{M}_{\rm h}.\end{aligned} \tag{10.30}$$

Therefore,

$$\mathbf{M} = \mathbf{M}_{\rm H} + \mathbf{M}_{\rm h}, \tag{10.31}$$

where the horizon contribution is

$$\mathbf{M}_{\rm H} = \frac{e^2}{4\pi\alpha}\mathcal{M}_{\rm H} \times \boldsymbol{m}_0 = \frac{eg|n|}{\sqrt{2\kappa\alpha}}\boldsymbol{m}_0 = 5.1|n|\mathbf{M}_{\rm Pl}. \tag{10.32}$$

Notice that this diverges when $\kappa \to 0$. At the same time, the hair contribution,

$$\mathbf{M}_{\rm h} = \frac{e^2}{4\pi\alpha}\mathcal{M}_{\rm h} \times \boldsymbol{m}_0, \tag{10.33}$$

remains finite when $\kappa \to 0$ because $\mathcal{M}_{\rm h}$ reduces in this limit precisely to the regularized mass of the flat space electroweak monopole: the Cho-Maison monopole for $|n| = 2$ [70] and its generalizations for $|n| > 2$ [59]. We have already discussed in Sec. V C the correspondence between the Cho-Maison monopole and the extremal hairy

black hole with $|n| = 2$. It turns out that a similar correspondence applies to higher charge solutions as well.

As a result, the extremal hairy solution with $|Q| \ll Q_\star$ can be viewed as the flat space monopole with the same charge Q harboring in the center a tiny charged black hole that almost does not affect the electroweak fields. The total mass of the flat space monopole is infinite because of the Coulombian singularity of the hypermagnetic field B at the origin, but gravity renders the mass finite due to the cutoff at the horizon. Therefore, the extremal hairy black holes provide "a classical UV completion" for the electroweak monopoles.

8. Increasing the charge

The size of the black hole is small compared to the size of the surrounding condensate only if the charge is not too large: $|Q| \approx 0.85\sqrt{\kappa}|n| \ll Q_\star \approx 0.72/\sqrt{\kappa}$. Increasing $|n|$, the size of the vacuum bubble $r_{\rm b} \approx 0.73\sqrt{|n|}$ increases, and the condensate size $r_{\rm c} \approx 1.13\sqrt{|n|}$ grows as well, but the horizon radius $r_{\rm ex} \approx 0.75\sqrt{\kappa}|n|$ grows faster, and when n becomes of the order of $1/\kappa$, the black hole starts absorbing the false vacuum region where the Higgs field is very small.

The horizon mass and hair mass are

$$M_{\rm H} \approx r_{\rm ex} \approx 0.75\sqrt{\kappa}|n|, \qquad M_{\rm h} \approx 0.10\kappa|n|^{3/2}, \tag{10.34}$$

where the latter follows from the estimate obtained in Minkowski space, because the rescaled hair mass $\mathcal{M}_{\rm h} = (8\pi/\kappa)M_{\rm h}$ essentially coincides with the regularized energy $E_{\rm reg}$ of the flat space monopole given by Eq. (5.24) in [59]. Taking gravity into account, our numerics confirm that $M_{\rm h} \propto |n|^{3/2}$ if $|Q| < Q_\star$.

As a result, although for small $|n|$ the horizon mass $M_{\rm H}$ is totally dominant as compared to the hair mass $M_{\rm h}$, the latter increases faster with growing $|n|$ and eventually overtakes the horizon mass. This means that the ratio $M_{\rm h}/|Q_{\rm h}|$ increases, but according to our numerics it always remains less than unity. The estimate (10.28) is no longer valid when Q approaches $Q_\star$, but the inequality $M < |Q|$ remains valid for ell extremal solutions.

On the other hand, the horizon value of the hypermagnetic field, $|{\rm B}(r_h)| \sim 1/|n|$ [see Eq. (10.2)], *decreases* with growing $|n|$, and when $|Q| \to Q_\star$ then $|{\rm B}(r_h)| \to m_{\rm H}^2$ and the Higgs field starts deviating from zero at the horizon. The solution then enters the next phase in which the electroweak symmetry is broken everywhere. Analyzing the condition $|{\rm B}(r_h)| = |n|/(2r_h^2) = m_{\rm H}^2$ together with Eq. (3.24) determining the value of $r_h = r_{\rm ex}$ yields

$$Q_\star = \frac{2\sqrt{2}g'}{g(g'^2+\beta)}\frac{1}{\sqrt{\kappa}} = \frac{0.7203}{\sqrt{\kappa}} = 0.6157Q_{\rm m}, \tag{10.35}$$

which reproduces (10.1) and agrees with our numerics.

B. Phase II: Oblate horizon, $|Q| > Q_\star$

If $|Q| < Q_\star$ then the horizon is spherical and one has $\delta = 0$, but for $|Q| > Q_\star$ one has $\delta > 0$; the horizon geometry is no longer spherical and is not described by the extremal RNdS solution (3.25). Therefore, the horizon symmetry changes through the transition point $|Q| = Q_\star$.

The horizon remains degenerate, and we continue to use the radial gauge defined by Eq. (8.2). However, since the horizon is no longer spherical, there is no longer any reason to enforce similarity with the RNdS case by imposing ${\rm r_H} = r_{\rm ex}$ in Eq. (8.2). Moreover, the expression for $r_{\rm ex}$ in Eq. (3.24) becomes complex valued when $|Q| > Q_{\rm m}$. For these reasons, we fix ${\rm r_H} = 0.2$ for all solutions in phase II.

Close to the transition point for $|Q| > Q_\star$ one has

$$\delta \propto (|Q| - Q_\star)^s. \tag{10.36}$$

This behavior resembles a second-order phase transition or possibly a crossover, given the rather large value of the critical exponent: according to our numerics, one finds $s \approx 10.8$ for $\kappa = 10^{-2}$.

Additionally, the fraction of the magnetic charge contained in the hair, which was constant in the previous phase, $\lambda = P_{\rm h}/P \approx 0.22$, starts to decrease for $|Q| > Q_\star$ [see Fig. 22, left panel]. As the charge increases, the black hole gradually absorbs the condensate and becomes less hairy; the ratio $M/|Q|$ increases, and the geometry approaches that of the extremal RN solution, and ultimately merges with it when the horizon size overtakes the condensate size. This occurs at $r_h = |Q| = r_{\rm c} \equiv r_h^0(n) = \sqrt{|n|}/g$, corresponding to the maximal charge

$$Q_{\rm max} = 2g'\sqrt{\beta}Q_{\rm m} = 1.29Q_{\rm m}, \tag{10.37}$$

which in turn corresponds to the maximal value $|n| = 8g'^2/\kappa = 1.78/\kappa$. This estimate of the maximal charge is supported by our numerics. No hairy solutions exist beyond this charge; black holes with $|Q| > Q_{\rm max}$ are thus RN.

The estimate (10.28) should be reformulated as an inequality valid for all extremal hairy solutions,

$$0.88 < M/|Q| \le 1. \tag{10.38}$$

Here the lower bound corresponds to the minimal charge when $|n| = 2$, whereas the upper bound is reached when the charge is maximal, $|Q| = Q_{\rm max}$.

C. Maximally hairy black holes

The amount of the black hole hair initially increases with charge, but begins to decrease after the phase transition. The black hole is maximally hairy near the critical point of the transition, at $|Q| \approx Q_\star \approx 0.62Q_{\rm m}$, where the ratio

$M_{\rm h}/M$ reaches its maximum [see Fig. 22, inset in the right panel]. This corresponds to the following values of the black hole charge, size and mass:

$$|n| \approx \frac{0.85}{\kappa} \approx 1.6 \times 10^{32}, \qquad \mathbf{r}_h \approx 1.41 \text{ cm},$$
$$\mathbf{M} \approx 2 \times 10^{25} \text{ kg}, \qquad \frac{\mathbf{M}_{\rm h}}{\mathbf{M}} \approx 0.11. \tag{10.39}$$

These estimates for the mass and radius are obtained for the physical value of $\kappa \sim 10^{-33}$, noting that for maximally hairy black holes one has $M \approx |Q|$, while the horizon radius $r_h = r_{\rm ex}$ is given by (3.23).

The resulting size and mass are typical for the planetary-mass black holes. The hair accounts for ≈11% of the total mass, implying that the black hole is surrounded by $\approx 2 \times 10^{24}$ kg of electroweak condensate [for comparison, the Earth mass is $\mathbf{M}_\oplus \approx 6 \times 10^{24}$ kg].

The value $\mathbf{M}_{\rm h}/\mathbf{M} \approx 0.11$ was obtained numerically for $10^{-3} < \kappa < 10^{-2}$, and appears to remain stable under variations of κ. We therefore expect it to apply for the physical value of κ as well, although we currently do not have a physical explanation for its origin.

It is also interesting to estimate the condensate size. The condensate terminates where $|\mathrm{B}| \approx m_{\rm W}^2$ at $r_{\rm c} \approx 1.13\sqrt{|n|}$, which corresponds to the dimensionful value

$$\mathbf{r}_{\rm c} \approx 2.20 \text{ cm}. \tag{10.40}$$

One may wonder how massive fields can extend over macroscopic distances. The key point is that they form a Bose-Einstein condensate. A familiar example is the condensate in a superconductor, which also can be macroscopically large despite involving massive fields. When the electroweak condensate terminates, the corona does not vanish abruptly but instead decays as $\sim Q_{\rm M}/r^4$, due to the presence of a magnetic quadrupole moment $Q_{\rm M}$ carried by the magnetic field.

One might think that the magnetic charge with $|n| = 1.6 \times 10^{32}$ is extremely large. However, as explained in Appendix D, a charge of this magnitude placed at the center of the Sun would create a magnetic field of $\approx 10^3$ Gauss at the Sun's surface. This is 1000 times larger than the average proper magnetic field of the Sun, but 2–4 times smaller than the field in sunspots.

D. Summary

Summarizing, the extremal hairy solutions show two phases depending on value of their charge $Q \approx 0.85\sqrt{\kappa}n$. If the charge is small then the hypermagnetic field B is strong enough to restore the full electroweak symmetry at the horizon where $\mathrm{W}^a_{\mu\nu}$ and Φ vanish. The horizon geometry is then perfectly spherical, but the magnetic fields $\mathcal{B}$ and $\mathcal{B}_Z$ keep a nontrivial dependence on the polar angle ϑ and form a corona of vortex loops attached to the horizon. These vortices do not change the magnetic flux $4\pi P$ through the horizon but render it inhomogeneous, highly increasing the field strength in the narrow equatorial region. Although all of charge P is contained inside the black hole in the 't Hooft description, the total flux can be interpreted as a superposition of two contributions: the flux produced by an effective charge g'^2P distributed along a ring at the horizon in the equatorial plane, and the remaining flux g^2P distributed more or less homogeneously over the entire horizon.

When the charge increases, the horizon value of B decreases. If the charge exceeds the critical value $Q_\star \approx 0.62 Q_{\rm m}$ where $Q_{\rm m} \approx 1.17/\sqrt{\kappa}$, then B becomes insufficient to create a region of symmetric phase around the horizon. As a result, the Higgs field starts deviating from zero at the horizon. The horizon geometry is then no longer spherical. However, the B field is still strong enough to create a condensate around the horizon. The condensate disappears, and the black hole loses its hair when the charge approaches the maximal value $Q_{\rm max} \approx 1.29 Q_{\rm m}$.

The mass of all extremal hairy solutions is smaller than the charge, $M/|Q| \leq 1$, which can be related to the Zeeman interaction between the W bosons in the condensate and the black hole magnetic field.

Various parameters of the extremal solutions against the charge are shown in Fig. 22. One can see that the quadrupole moments and 't Hooft currents attain their maximal values in phase I. They vanish for the minimal value of the charge $|n| = 2$ when the configuration is spherically symmetric, and for the maximal charge when the hair disappears. The horizon oblateness and the Nambu currents attain maximal values in phase II, while the fraction of the hair charge $\lambda = P_{\rm h}/P$ is constant in phase I and decreases down to zero in phase II. As seen in Fig. 22, one has $r_h/|Q| \approx M/|Q| \leq 1$.

The domain of existence for these hairy solutions is shown in the right panel of Fig. 22, which presents the ratio $M/|Q|$ against the magnetic charge $|Q| = \sqrt{\kappa/2}|n|/(2e)$. The hairy solutions occupy the shaded region between two curves: below the upper curve corresponding to the bifurcation with the RN branch, and above the lower curve corresponding to the extremal hairy solutions. Spherically symmetric solutions with $|n| = 2$ correspond to the left edge of the region; they were previously known [43], whereas all solutions with $|n| > 2$ are new. Descending from the upper curve to the lower one at fixed Q increases the amount of charge stored in the condensate and decreases the ratio $M/|Q|$. As shown in the figure, the inequality $M/|Q| \leq 1$ holds not only for extremal solutions but also for near-extremal ones. For the extremal solutions in Fig. 22, one finds $0.91 \leq M/|Q| \leq 1$, which slightly differs from the estimate in Eq. (10.38) because the figure is obtained not for the physical value of the gravitational coupling $\kappa \sim 10^{-33}$, but for $\kappa = 10^{-2}$.

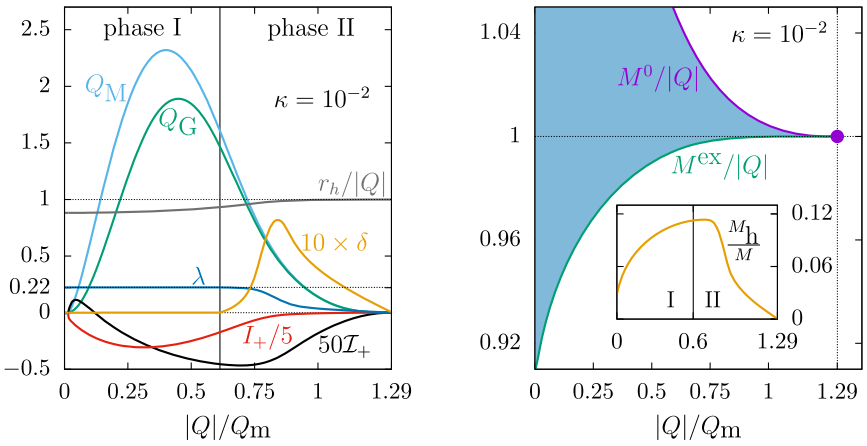


FIG. 22. The parameters of extremal solutions (left) and the existence diagram for hairy solutions (right) for $\kappa = 10^{-2}$. The upper violet curve on the right corresponds to solutions bifurcating with the RN while the lower green curve corresponds to extremal solutions. The blue shaded area between these two curves is the domain of existence of nonextremal hairy solutions. The scale for the charge is set by $Q_{\rm m} \approx 1.17/\sqrt{\kappa}$ defined in (3.24).

XI. CONCLUDING REMARKS

We have constructed solutions describing static and axially symmetric black holes that support a magnetic field strong enough to alter the structure of the electroweak vacuum. This leads to the formation of an electroweak condensate outside the black hole horizon. The condensate contains charged W bosons, which form a fluidlike state whose flow generates persistent currents along the horizon. These currents produce a corona of fountainlike vortex loops surrounding the horizon. Together, the condensate and the corona constitute the black hole hair.

No new physics is required for the existence of these hairy black holes. They are solutions of the standard electroweak theory minimally coupled to standard Einstein gravity, without any additional modifications, such as the nonminimal coupling of the Higgs field [86]. The physical mechanism responsible for hair formation does not arise in the conventional Einstein–Maxwell theory, but it is well known in electroweak theory: electroweak condensation, which has been extensively studied in flat space [47–50]. We simply consider this mechanism in the presence of gravity.

Therefore, our solutions can be regarded as a natural extension of electrovacuum black holes, since electroweak theory contains electromagnetism as a special limit. However, because this extension is non-Abelian, the standard no-hair arguments of electrovacuum theory do not apply. This is precisely what makes the existence of black hole hair possible.

According to Maldacena [46], the presence of the corona should significantly enhance the evaporation rate. As a result, nonextremal black holes are expected to rapidly relax toward the extremal state, which correspond to the lower edge of the existence region in Fig. 22 where $M \leq |Q|$. In this extremal state, the black holes cannot shed their hair to evolve into RN black holes, for which $M \geq |Q|$. In principle, they could decay by emitting pairs of hairy black holes with $n = \pm 2$, which minimize the ratio $M/|Q|$, but such a process would require quantum tunneling and is therefore expected to be strongly suppressed.

However, axially symmetric black holes can reduce their energy by developing a fully spread corona of vortices, which may retain at most only discrete symmetries. In the axially symmetric case, the corona consists of two oppositely directed multivortices. Each multivortex is composed of many elementary vortices that repel each other, making the configuration inherently unstable (except for $|n| = 4$). This instability is evident at the perturbative level, as shown in Sec. VI, where the axially symmetric configuration corresponds to a saddle point of the energy. In contrast, the absolute energy minimum corresponds to a configuration of elementary vortices that maximize their mutual separation, as illustrated in Fig. 6 (left panel). Nonperturbative generalizations of this configuration are expected to describe stable hairy black holes surrounded by an electroweak corona. However, the corresponding solutions are currently unknown, except for the spherically symmetric case with $n = \pm 2$, which contains no vortices, and the axially symmetric case with $n = \pm 4$, where the vortices are already elementary.

The transition from the axially symmetric state to a fully spread corona should not only reduce the energy, but also increase the entropy. One may expect that, for very large $|n|$, the condensate and the associated vortices in the corona form a gaslike or liquidlike phase [50]. The ground state of such a system is likely to be highly degenerate, with a high density of low-lying excitations above it. As a result, there should be a nontrivial entropy associated with the black hole hair.

As we have seen above, the black hole mass and charge split into two parts, associated respectively with the black hole itself and with the surrounding hair. It is

therefore natural to assume that the entropy also splits as $S = S_{\rm H} + S_{\rm h}$, where the first term is determined by the horizon area. As shown in Fig. 22, for extremal hairy black holes one finds $r_h < |Q|$, whereas for extremal RN black holes $r_h = |Q|$, so the horizon entropy satisfies $S_{\rm H} < S_{\rm RN}$.

On the other hand, as shown in Fig. 22, the ratio $r_h/|Q|$ is close to unity. It is therefore possible that including the hair entropy may reverse the inequality to $S_{\rm H} + S_{\rm h} > S_{\rm RN}$. This would imply that extremal hairy black holes with a fully spread corona are not only energetically preferred over RN black holes, but are also favored entropically, which would enhance their formation rate. However, for this to be true, the hair entropy $S_{\rm h}$ should be sufficiently large. It is expected to be maximal for maximally hairy black holes, where $r_h \sim Q_\star \sim 1/\sqrt{\kappa} \sim \sqrt{|n|}$, implying that $S_{\rm H} \sim S_{\rm RN} \sim r_h^2/\kappa \sim |n|/\kappa \sim n^2$. Therefore, $S_{\rm h}$ should also scale as n^2. Using, for instance, the ideal gas approximation for the hair entropy gives $S_{\rm h} \sim |n| \ln |n|$, which is not large enough. On the other hand, the vortices in the corona are not point particles but extended objects (fountains) that can become mutually entangled in a complex way, as we observed in the perturbative description of Sec. VI. This should increase their entropy. Since we cannot currently give a reliable estimate for $S_{\rm h}$, we leave this issue for future analysis.

Our solutions provide the first example of hairy black holes described by well-tested physical theories—the Standard Model and general relativity. Therefore, these solutions may be physically relevant (the $n = 2$ solutions of [43] are too close to the Planck scale to be considered realistic). Such black holes could plausibly originate from primordial black holes, which may acquire charge from the early electroweak plasma.

Suppose that the fluctuating hypermagnetic field in the ambient plasma becomes, at some moment, predominantly orthogonal to the black hole horizon. This would induce a net flux through the horizon, and hence generate a charge. Since the total magnetic charge is conserved, the flux generated on one black hole must be compensated by an opposite flux on another black hole (or several others). The resulting oppositely charged black holes would attract one another, but they might not necessarily annihilate, as cosmic expansion can drive them apart. Moreover, oppositely charged black holes may potentially form bound systems stabilized by scalar repulsion, as illustrated by the examples considered in [87,88].

It is also possible that, during the electroweak phase transition, a network of electroweak Nambu strings formed in the early Universe, as suggested in [89,90]. Nambu strings terminate at Nambu monopoles; therefore, magnetic monopoles may have been dynamically created at early times. When these monopoles are absorbed by primordial black holes, the latter acquire a magnetic charge.

Mechanisms for magnetic charge generation remain to be verified, but if confirmed, it would have significant implications. Magnetic monopoles are typically associated with Grand Unified Theories, which involve physics beyond the Standard Model—the existence of which remains an open question. However, if primordial black holes can indeed acquire magnetic charge through a process similar to the one described above, this would suggest that no new physics beyond the Standard Model is required to account for monopoles. In this scenario, the magnetic charge does not require a conventional carrier particle but is instead associated with the magnetic flux threading the black hole event horizon. From this perspective, extremal hairy electroweak black holes naturally emerge as compelling candidates for magnetic monopoles—objects that may, in principle, exist in nature without invoking physics beyond the Standard Model.

These black holes can exhibit a variety of physical effects. For instance, they are expected to catalyze proton decay [46]. They could potentially be detected if captured by a neutron star, leading to a sudden change in the star's rotation period [54]. Their phenomenology is quite rich and has been explored in Refs. [51–55].

Finally, it is worth noting that there are numerous directions in which our results can be extended and generalized. Most obviously, one should explicitly construct nonaxially symmetric solutions with $|n| > 4$ and demonstrate that they indeed minimize the energy. It would also be natural to explore their stationary generalizations. Crucially, one should clarify the physical mechanism by which black holes can acquire magnetic charge. In addition, it is important to account for the role of fermions, verify the enhancement of Hawking evaporation, examine the Rubakov-Callan effect, further develop the phenomenology, etc.

ACKNOWLEDGMENTS

We thank Eugen Radu, Maxim Chernodub, Julien Garaud, Christos Charmousis, and Valerie Domcke for valuable discussions. M. S. V. is grateful to the Theory Division of CERN for its hospitality during the final stage of this work.

DATA AVAILABILITY

The data that support the findings of this article are not publicly available upon publication because it is not technically feasible and/or the cost of preparing, depositing, and hosting the data would be prohibitive within the terms of this research project. The data are available from the authors upon reasonable request.

APPENDIX A: ENERGY-MOMENTUM TENSOR

In this appendix, we explicitly present the components of the electroweak energy-momentum tensor in the axially symmetric case. Substituting (7.2) and (7.22) into (2.20) yields the following diagonal components of the energy-momentum tensor:

$$
\begin{aligned}
-T^0{}_0\sqrt{-\mathrm{g}} &= a_1 + a_2 + a_3 + a_4 + a_5,\\
-T^{\mathrm{r}}{}_{\mathrm{r}}\sqrt{-\mathrm{g}} &= -a_1 + a_2 - a_3 + a_4 + a_5,\\
-T^{\vartheta}{}_{\vartheta}\sqrt{-\mathrm{g}} &= a_1 - a_2 - a_3 + a_4 + a_5,\\
-T^{\varphi}{}_{\varphi}\sqrt{-\mathrm{g}} &= -a_1 - a_2 + a_3 + a_4 - a_5,
\end{aligned}
\tag{A1}
$$

where $\sqrt{-\mathrm{g}} = e^{2\mathrm{K}+\mathrm{S}-2\mathrm{U}}\mathrm{r}^2\sin\vartheta$, and

$$
\begin{aligned}
a_1 &= \mathrm{N}e^{2\mathrm{U}-\mathrm{S}}\left[\frac{1}{2g'^2}(\partial_{\mathrm{r}}Y)^2 + \frac{1}{2g^2}((\mathcal{D}_{\mathrm{r}}F_3)^2 + (\mathcal{D}_{\mathrm{r}}F_4)^2)\right]\frac{\nu^2}{\sin\vartheta},\\
a_2 &= e^{2\mathrm{U}-\mathrm{S}}\left[\frac{1}{2g'^2}(\partial_{\vartheta}Y)^2 + \frac{1}{2g^2}((\mathcal{D}_{\vartheta}F_3)^2 + (\mathcal{D}_{\vartheta}F_4)^2)\right]\frac{\nu^2}{\mathrm{r}^2\sin\vartheta},\\
a_3 &= \mathrm{N}e^{\mathrm{S}}\left[\frac{1}{2g^2}e^{2\mathrm{U}-2\mathrm{K}}(\partial_{\vartheta}F_1 - \partial_{\mathrm{r}}F_2)^2 + \mathrm{r}^2(\mathcal{D}_{\mathrm{r}}\phi_1)^2 + \mathrm{r}^2(\mathcal{D}_{\mathrm{r}}\phi_2)^2\right]\sin\vartheta,\\
a_4 &= e^{\mathrm{S}}\left[(\mathcal{D}_{\vartheta}\phi_1)^2 + (\mathcal{D}_{\vartheta}\phi_2)^2 + \frac{\beta\mathrm{r}^2}{8}e^{2\mathrm{K}-2\mathrm{U}}(\phi_1^2+\phi_2^2-1)^2\right]\sin\vartheta,\\
a_5 &= e^{2\mathrm{K}-\mathrm{S}}[((F_3+Y)\phi_1 - F_4\phi_2)^2 + ((F_3-Y)\phi_2 + F_4\phi_1)^2]\frac{\nu^2}{4\sin\vartheta}.
\end{aligned}
\tag{A2}
$$

Here, the following abbreviations have been introduced:

$$
\begin{aligned}
&\mathcal{D}_{\mathrm{r}}F_3 = \partial_{\mathrm{r}}F_3 + F_1F_4, \quad \mathcal{D}_{\vartheta}F_3 = \partial_{\vartheta}F_3 + F_2F_4, \quad \mathcal{D}_{\mathrm{r}}F_4 = \partial_{\mathrm{r}}F_4 - F_1F_3, \quad \mathcal{D}_{\vartheta}F_4 = \partial_{\vartheta}F_4 - F_2F_3,\\
&\mathcal{D}_{\mathrm{r}}\phi_1 = \partial_{\mathrm{r}}\phi_1 - \frac{F_1}{2}\phi_2, \quad \mathcal{D}_{\vartheta}\phi_1 = \partial_{\vartheta}\phi_1 - \frac{F_2}{2}\phi_2, \quad \mathcal{D}_{\mathrm{r}}\phi_2 = \partial_{\mathrm{r}}\phi_2 + \frac{F_1}{2}\phi_1, \quad \mathcal{D}_{\vartheta}\phi_2 = \partial_{\vartheta}\phi_2 + \frac{F_2}{2}\phi_1.
\end{aligned}
$$

The only off diagonal components are $T_{\mathrm{r}\vartheta} = T_{\vartheta\mathrm{r}}$ with

$$
\begin{aligned}
T^{\mathrm{r}}_{\vartheta}\sqrt{-\mathrm{g}} = \mathrm{N}e^{2\mathrm{U}-\mathrm{S}}&\left[\frac{1}{g'^2}\partial_{\mathrm{r}}Y\partial_{\vartheta}Y + \frac{1}{g^2}(\mathcal{D}_{\mathrm{r}}F_3\mathcal{D}_{\vartheta}F_3 + \mathcal{D}_{\mathrm{r}}F_4\mathcal{D}_{\vartheta}F_4)\right]\frac{\nu^2}{\sin\vartheta}\\
&+ 2\mathrm{r}^2\mathrm{N}e^{\mathrm{S}}(\mathcal{D}_{\mathrm{r}}\phi_1\mathcal{D}_{\vartheta}\phi_1 + \mathcal{D}_{\mathrm{r}}\phi_2\mathcal{D}_{\vartheta}\phi_2)\sin\vartheta.
\end{aligned}
\tag{A3}
$$

The energy-momentum tensor is gauge invariant. Its diagonal components are invariant under the reflection $\vartheta \to \pi - \vartheta$, while the off diagonal components then change sign.

APPENDIX B: AXIALLY SYMMETRIC FORM OF THE $n = \pm 2$ SOLUTIONS

Before considering axially symmetric solutions with $|n| > 2$, it is instructive to first reproduce the spherically symmetric solutions with $|n| = 2$ within the axially symmetric formalism. A spherically symmetric solution is described by Eqs. (3.1) and (3.2), with functions $N(r), \sigma(r), f(r), \phi(r)$ depending on the Schwarzschild radial coordinate r.

The same solution, expressed within the axially symmetric formalism, is described by the line element (7.2) and electroweak fields (7.22) and (7.27) parametrized by functions $\mathrm{N}, \mathrm{U}, \mathrm{K}, \mathrm{S}, H_k, y, \phi_1, \phi_2$. These functions depend on the radial coordinate r, distinct from r.

Notice that $N(r)$ is obtained by solving the equations, whereas $\mathrm{N}(\mathrm{r})$ is the auxiliary function whose choice determines the radial gauge. For example, one can choose $\mathrm{N}(\mathrm{r}) = 1$.

The relation between the coordinates r and r is determined by

$$
\frac{d\mathrm{r}}{\mathrm{r}\sqrt{\mathrm{N}(\mathrm{r})}} = \frac{dr}{r\sqrt{N(r)}},
\tag{B1}
$$

integrating which yields $\mathrm{r} = \mathrm{r}(r)$. One has then

$$
\begin{aligned}
&e^{2\mathrm{U}} = \frac{N(r)}{\mathrm{N}(\mathrm{r})}\sigma^2(r), \quad e^{\mathrm{K}-\mathrm{U}} = e^{\mathrm{S}-\mathrm{U}} = \frac{r}{\mathrm{r}},\\
&H_2 = H_4 = f(r), \quad H_1 = H_3 = y = \phi_1 = 0, \quad \phi_2 = \phi(r).
\end{aligned}
\tag{B2}
$$

1. Nonextremal solutions

For nonextremal solutions the metric coefficient g_{00} shows a simple zero at the horizon, which can be ensured by choosing the auxiliary function N(r) to be

$$\mathrm{N} = 1 - \frac{\mathrm{r_H}}{\mathrm{r}}.$$

For the nonextremal RN solution (3.6), Eqs. (B1) and (B2) then yield

$$\mathrm{r} = r - r_-, \quad \mathrm{r_H} = r_+ - r_-, \quad e^{\mathrm{U}} = \frac{\mathrm{r}}{\mathrm{r}+r_-},$$
$$\mathrm{K} = \mathrm{S} = H_1 = H_2 = H_3 = H_4 = y = \phi_1 = 0, \quad \phi_2 = 1, \tag{B3}$$

where $r_\pm = M \pm \sqrt{M^2 - Q^2}$ are the two RN horizons. One has

$$r_+ r_- = Q^2 \equiv \frac{\kappa}{2e^2} = r_-^2 + \mathrm{r_H} r_- \Rightarrow r_- = \frac{1}{2}\left(\sqrt{\mathrm{r_H^2} + 4Q^2} - \mathrm{r_H}\right). \tag{B4}$$

In the extremal limit, when $M \to Q$, one has $\mathrm{r_H} \to 0$, while the horizon value $\mathrm{U_H} = \ln(\mathrm{r_H}/r_+)$ diverges.

For the nonextremal hairy solutions one can represent $N(r)$ in (3.1) as

$$N(r) = \frac{1}{\alpha^2(r)}\left(1 - \frac{r_h}{r}\right), \tag{B5}$$

where $\alpha(r_h) \equiv \alpha_h$ and $\alpha(\infty) = 1$. Integrating then Eq. (B1) yields the relation between r and r, expressed by

$$X(\mathrm{r}, \mathrm{r_H}) = (X(r, r_h))^{\alpha(r)} \times \mathcal{F}(r) \quad \text{with}$$
$$\mathcal{F}(r) = \exp\left(\int_r^\infty \alpha'(r) \ln\left(X(r, r_h)\right) dr\right), \tag{B6}$$

where the following definition has been used:

$$X(x, x_1) \equiv \frac{\sqrt{x} + \sqrt{x - x_1}}{2}. \tag{B7}$$

This implies that at infinity, where $r, \mathrm{r} \to \infty$, one has $\mathrm{r}/r \to 1$ and $\mathrm{U}, \mathrm{S}, \mathrm{K} \to 0$. At the horizon, where $\mathrm{r} = \mathrm{r_H}$ and $r = r_h$, one has

$$\sqrt{\mathrm{r_H}} = 2\left(\frac{\sqrt{r_h}}{2}\right)^{\alpha_h} \times \mathcal{F}(r_h); \tag{B8}$$

hence $e^{\mathrm{S_H} - \mathrm{U_H}} = r_h/\mathrm{r_H} \neq 1$. With some algebra, one finds

$$\lim_{r \to r_h} \frac{dN(r)}{dr} = \frac{1}{\alpha_h^2 r_h}, \quad \lim_{r \to r_h} \frac{d\mathrm{N}(\mathrm{r}(r))}{dr} = \frac{\alpha_h^2}{r_h}, \Rightarrow e^{\mathrm{U_H}} = \frac{\sigma_h}{\alpha_h^2}. \tag{B9}$$

Applying the surface gravity formula (7.19) separately within the spherically symmetric and axially symmetric formalisms yields

$$\mathrm{k_H} = \frac{\sigma_h}{2\alpha_h^2 r_h} = \frac{1}{2r_h} e^{\mathrm{U_H}} = \frac{1}{2\mathrm{r_H}} e^{2\mathrm{U_H} - \mathrm{K_H}}. \tag{B10}$$

In the extremal limit, $r_h \to r_{\mathrm{ex}} > 0$ when the horizon becomes degenerate and $\mathrm{k_H} \to 0$, the value σ_h approaches a nonzero limit, so $\alpha_h \to \infty$. It follows that

$$r_h \to r_{\mathrm{ex}}, \qquad \mathrm{r_H} \to 0,$$
$$e^{\mathrm{U_H}} \to 0, \qquad e^{\mathrm{K_H} - \mathrm{U_H}} = e^{\mathrm{S_H} - \mathrm{U_H}} = \frac{r_h}{\mathrm{r_H}} \to \infty. \tag{B11}$$

Having computed $\mathrm{U}, \mathrm{S}, \ldots$ from (B2), the same values are obtained by solving the axially symmetric equations numerically. Figure 23 shows the profiles of

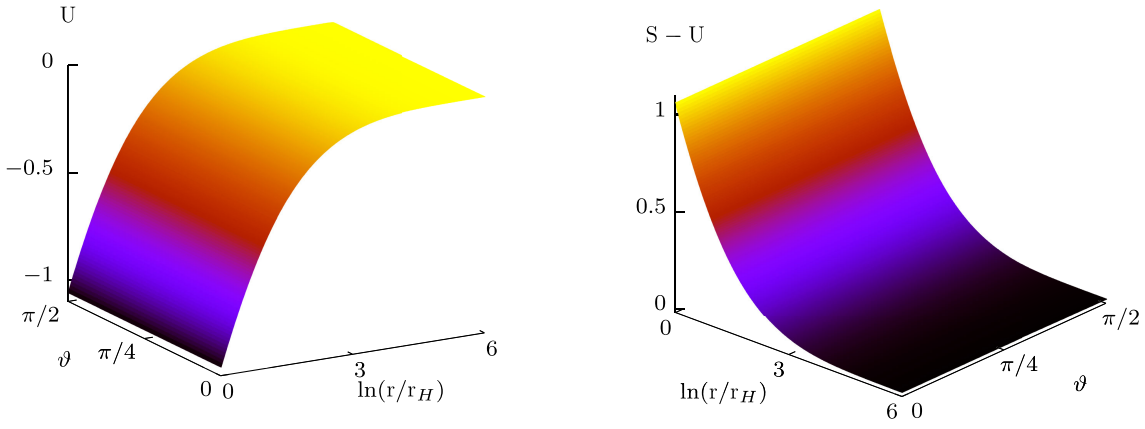


FIG. 23. The metric amplitude U and the difference S–U for the nonextremal spherically symmetric hairy black hole with $n = 2$, $\kappa = 10^{-3}$, and $\mathrm{r_H} = 0.02$ as functions of $\ln(\mathrm{r}/\mathrm{r_H})$ and ϑ.

U and S–U for $\kappa = 10^{-3}$ and $\mathrm{r_H} = 0.02$. One finds that $r_h = \mathrm{r_H} e^{\mathrm{S_H}-\mathrm{U_H}} = 0.058 > r_{\mathrm{ex}} = 0.047$, while $\mathrm{r_H} < r_{\mathrm{ex}}$. As $\mathrm{r_H}$ decreases further and approaches zero, $\mathrm{U_H}$ shifts more and more to negative values, while $\mathrm{S_H} - \mathrm{U_H}$ grows, as suggested by (B11).

2. Extremal solutions

Since $\mathrm{U_H}$ becomes unbounded when approaching the extremal limit, this case should be considered separately. In this limit, the horizon becomes degenerate, and the function $N(r)$ takes the structure shown in (5.19). Equations (B1) and (B2) then imply that the amplitudes U, K, S will be finite at the horizon and approach zero at infinity, provided that N(r) has the same structure as $N(r)$:

$$\mathrm{N(r)} = \mathrm{k^2(r)}\left(1 - \frac{\mathrm{r_H}}{\mathrm{r}}\right)^2, \qquad N(r) = k^2(r)\left(1 - \frac{r_{\mathrm{ex}}}{r}\right)^2, \tag{B12}$$

where r_{ex} is defined in (3.23) with $\mathrm{k(r_H)} = k(r_{\mathrm{ex}}) \equiv k$, while $\mathrm{k}(\infty) = k(\infty) = 1$.

It is convenient to set

$$\mathrm{r_H} = r_{\mathrm{ex}}, \tag{B13}$$

so that the radial coordinate r coincides with the Schwarzschild coordinate r at the horizon. Integrating Eq. (B1) then yields

$$\frac{\ln(r - \mathrm{r_H})}{k(r)} - \frac{\ln(\mathrm{r} - \mathrm{r_H})}{\mathrm{k(r)}} = \int_r^\infty \ln(r - \mathrm{r_H})\frac{k'(r)}{k^2(r)}dr - \int_{\mathrm{r}}^\infty \ln(\mathrm{r} - \mathrm{r_H})\frac{\mathrm{k'(r)}}{\mathrm{k^2(r)}}d\mathrm{r}. \tag{B14}$$

The right-hand side of this relation approaches zero when $r, \mathrm{r} \to \infty$, so that $\mathrm{r}/r \to 1$. According to (B2), this implies that $\mathrm{U}, \mathrm{K}, \mathrm{S} \to 0$. When $r, \mathrm{r} \to \mathrm{r_H}$, the right-hand side of (B14) approaches a finite value, which we denote by C. Hence, close to the horizon, we have

$$\frac{r - \mathrm{r_H}}{\mathrm{r} - \mathrm{r_H}} = \frac{\sqrt{N}}{\sqrt{\mathrm{N}}} = e^{kC}. \tag{B15}$$

Using Eq. (B2), this implies

$$e^{\mathrm{U_H}} = e^{\mathrm{S_H}} = e^{\mathrm{K_H}} = \sigma_h e^{kC}, \tag{B16}$$

so that the metric amplitudes are now finite at the horizon.

Applying the above formulas to the extremal RN solution yields a very simple result:

$$\mathrm{N} = \left(1 - \frac{\mathrm{r_H}}{\mathrm{r}}\right)^2, \quad \mathrm{U} = \mathrm{K} = \mathrm{S} = H_1 = H_2 = H_3 = H_4 = y = \phi_1 = 0, \quad \phi_2 = 1. \tag{B17}$$

For the extremal hairy black hole, the function $k(r)$ takes the form (3.25) at the horizon. Hence, by introducing an additional cutoff factor, we set

$$\mathrm{k^2(r)} = 1 - \frac{\Lambda}{3}[\mathrm{r^2} + 2\mathrm{r_H r} + 3\mathrm{r_H^2}] \times \frac{1 + \mathrm{r_H^4}}{1 + \mathrm{r^4}}, \tag{B18}$$

so that $\mathrm{k^2(r_H)} = k^2(r_{\mathrm{ex}})$ and $\mathrm{k^2}(\infty) = 1$. Integrating the axially symmetric equations numerically then yields profiles of U and S–U, shown in Fig. 24. These profiles are quite different from those for the nonextremal solution in Fig. 23, but they agree with the result in (B16). In particular, $\mathrm{S} - \mathrm{U} = \ln(r/\mathrm{r})$ now vanishes both at the horizon and at infinity.

3. Fixing the radial gauge: Summary

The upshot is as follows. The spherically symmetric hairy solutions can be labeled by the Schwarzschild radius

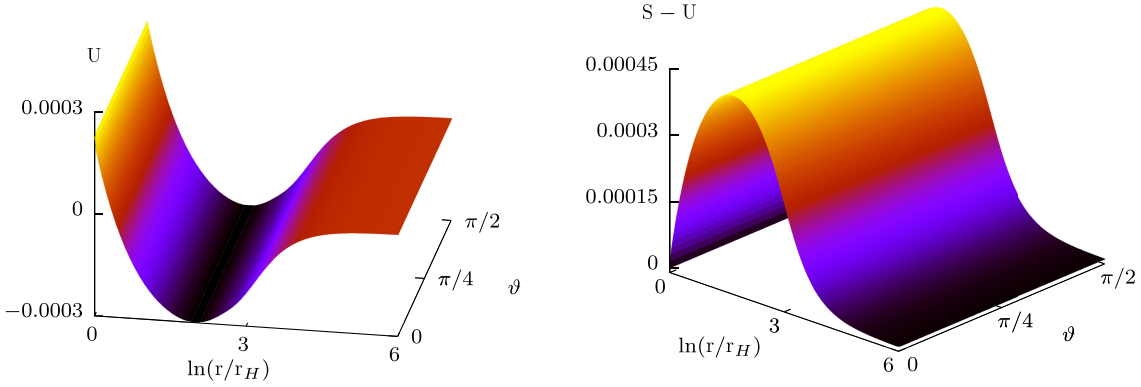


FIG. 24. The metric amplitude U and the difference S–U for the extremal spherically symmetric hairy black hole with $n = 2$ and $\kappa = 10^{-3}$, in which case $\mathrm{r_H} = r_{\mathrm{ex}} = 0.047$.

of their event horizon, $r_h \in [r_{ex}, r_h^0]$. The same solutions within the axially symmetric description are labeled by $\mathrm{r_H}$, which we call event horizon size, even though it does not have a direct physical meaning. The parameter $\mathrm{r_H}$ and the auxiliary function N(r) in (7.2) take the following values:

$$\begin{aligned}&\text{Nonextremal case}: 0<\mathrm{r_H}\le \mathrm{r_H^0}=r_+^0-r_-^0, \quad \mathrm{N(r)}=1-\frac{\mathrm{r_H}}{\mathrm{r}};\\ &\text{Extremal case}: \mathrm{r_H}=r_{ex}, \quad \mathrm{N(r)}=\mathrm{k^2(r)}\left(1-\frac{\mathrm{r_H}}{\mathrm{r}}\right)^2,\end{aligned} \tag{B19}$$

with k(r) given by (B18) and r_{ex} defined in (3.23). Here, $r_+^0 \equiv r_h^0$ and r_-^0 are the two horizons of the RN solution, to which the hairy black holes reduce at the bifurcation point $r_h = r_h^0$ (note that for the RN solution, $\mathrm{r_H} = r_+ - r_-$). Since $r_+ r_- = Q^2$ with Q from (3.6), one has

$$\mathrm{r_H^0} = r_+^0 - r_-^0 = r_h^0 - Q^2/r_h^0. \tag{B20}$$

We use the same gauge conditions, (B19) and (B20), also for $|n| > 2$.

4. Choice of $\mathrm{r_H}$ and diffeomorphisms

The value of $\mathrm{r_H}$ can be changed by a diffeomorphism in the extremal case, while for the nonextremal case this is not possible. Suppose that $\mathrm{r} \to \mathrm{r}(\tilde{\mathrm{r}})$ and consider Eq. (7.3),

$$\frac{d\mathrm{r}}{\mathrm{r}\sqrt{\mathrm{N(r)}}} = \frac{d\tilde{\mathrm{r}}}{\tilde{\mathrm{r}}\sqrt{\tilde{\mathrm{N}}(\tilde{\mathrm{r}})}}. \tag{B21}$$

Integrating this equation yields a relation between r and $\tilde{\mathrm{r}}$. In the nonextremal case, one chooses $\mathrm{N} = 1 - \mathrm{r_H}/\mathrm{r}$ and $\tilde{\mathrm{N}} = 1 - \tilde{\mathrm{r}}_\mathrm{H}/\tilde{\mathrm{r}}$. Performing the integration then shows that the only possibility is $\mathrm{r} = \tilde{\mathrm{r}}$ and $\mathrm{r_H} = \tilde{\mathrm{r}}_\mathrm{H}$. Therefore, the value of $\mathrm{r_H}$ cannot by changed by a diffeomorphism.

In the extremal case, N is chosen as in Eq. (B12), and similarly for $\tilde{\mathrm{N}}$, with the replacement $\mathrm{r} \to \tilde{\mathrm{r}}$, $\mathrm{r_H} \to \tilde{\mathrm{r}}_\mathrm{H}$. In this case the integration of (B21) yields a relation similar to that in (B14):

$$\begin{aligned}&\frac{\ln(\mathrm{r}-\mathrm{r_H})}{\mathrm{k(r)}} + \int_{\mathrm{r_H}}^{\mathrm{r}} \ln(\mathrm{r}-\mathrm{r_H})\frac{\mathrm{k}'(\mathrm{r})}{\mathrm{k}^2(\mathrm{r})}d\mathrm{r}\\ &= \frac{\ln(\tilde{\mathrm{r}}-\tilde{\mathrm{r}}_\mathrm{H})}{\tilde{\mathrm{k}}(\tilde{\mathrm{r}})} + \int_{\tilde{\mathrm{r}}_\mathrm{H}}^{\tilde{\mathrm{r}}} \ln(\tilde{\mathrm{r}}-\tilde{\mathrm{r}}_\mathrm{H})\frac{\tilde{\mathrm{k}}'(\tilde{\mathrm{r}})}{\tilde{\mathrm{k}}^2(\tilde{\mathrm{r}})}d\tilde{\mathrm{r}}.\end{aligned} \tag{B22}$$

This establishes a nontrivial correspondence between r and $\tilde{\mathrm{r}}$ for any given $\mathrm{r_H}$ and $\tilde{\mathrm{r}}_\mathrm{H}$. In the vicinity of the horizon, it simplifies to

$$\tilde{\mathrm{r}} - \tilde{\mathrm{r}}_\mathrm{H} = (\mathrm{r}-\mathrm{r_H})^{\tilde{\mathrm{k}}/\mathrm{k}}(1+\ldots), \tag{B23}$$

where $\mathrm{k} \equiv \mathrm{k}(\mathrm{r_H})$, $\tilde{\mathrm{k}} \equiv \tilde{\mathrm{k}}(\tilde{\mathrm{r}}_\mathrm{H})$, and the dots denote subleading terms.

Assuming that $\mathrm{r_H} = r_{ex}$, which is the radius of the RNdS solution defined in Eq. (3.24), the metric amplitudes U, K, S remain everywhere regular. However, since $\mathrm{k} \neq \tilde{\mathrm{k}}$, it follows from the relation $e^{\mathrm{U}}\sqrt{\mathrm{N}} = e^{\tilde{\mathrm{U}}}\sqrt{\tilde{\mathrm{N}}}$ [see Eq. (7.3)] that the amplitude $\tilde{\mathrm{U}}$ becomes unbounded at the horizon. This implies that, while the value of $\mathrm{r_H}$ can indeed be changed by a diffeomorphism in the extremal case, the resulting gauge choice leads to a singularity at the horizon.

At the same time, the singularity is very mild and located in a narrow region near the horizon. We have verified that choosing in our numerical code $\mathrm{r_H} = r_{ex}$, in which case everything is regular, or selecting a different value such as $\mathrm{r_H} = 1$, in which case there is a singularity, returns the same values of the physical parameters such as the total mass, horizon area, etc.

Therefore, we adopt the following strategy. As described in Sec. X, extremal hairy solutions exhibit two distinct phases depending on their charge. For extremal solutions in phase I, where the horizon remains spherical, as for the RNdS solution, we always choose $\mathrm{r_H} = r_{ex}$ to ensure regularity at the horizon.

In contrast, for extremal solutions in phase II, the horizon is still degenerate but no longer spherical. In this regime, there is no compelling reason to preserve similarity with the RNdS case. Furthermore, hairy solutions in phase II exist for $|Q| > Q_\mathrm{m}$, in which case the value of r_{ex} defined by Eq. (3.24) becomes complex. Therefore, we abandon the condition $\mathrm{r_H} = r_{ex}$ and instead set $\mathrm{r_H} = 0.2$ for all solutions in phase II. Numerical solutions obtained in this gauge exhibit no irregularities, and the virial relation is satisfied. We therefore conclude that this gauge choice is acceptable. Moreover, we observe a smooth transition between phase I and phase II.

APPENDIX C: ANTISCREENING PROPERTY OF THE CONDENSATE

It is instructive to examine simple models that illustrate the antiscreening property of the electroweak condensate. We originally developed these models to enhance our own understanding of the phenomenon. However, they can also be considered independently, as they are of interest in their own right, regardless of their connection to the main discussion.

The antiscreening property of the electroweak condensate property is the opposite of the well-known screening within the conventional Abelian model of superconductivity defined by Eq. (F1) in Appendix F. This model admits vortices consisting of a magnetic field and a complex scalar (see Appendix F). Their magnetic field is maximal at the vortex center, where scalar describing the superconducting condensate vanishes. However, the magnetic field decays to zero away from the center, where the condensate

approaches a constant value. Therefore, the field is screened by the condensate: it is zero where the condensate is maximal.

As we shall now see, the structure of vortices appearing via the electroweak condensation is just the opposite: their magnetic field is maximal where the condensate is maximal, so that the field is enhanced by the condensate [47,48].

In the linear approximation, the electroweak condensate is described by a complex vector w_μ subject to Eq. (4.3),

$$\mathcal{D}^\mu w_{\mu\nu} + ieF_{\nu\sigma}w^\sigma = m_{\rm W}^2 w_\nu, \tag{C1}$$

with $w_{\mu\nu} = \mathcal{D}_\mu w_\nu - \mathcal{D}_\nu w_\mu$ and $\mathcal{D}_\mu = \nabla_\mu + ieA_\mu$, where $F_{\mu\nu} = \partial_\mu A_\nu - \partial_\nu A_\mu$ is the background electromagnetic field. In some special cases, this equation can be solved by

$$w_{\mu\nu} = 0, \qquad ieF_{\nu\sigma}w^\sigma = m_{\rm W}^2 w_\nu. \tag{C2}$$

The condensate generates the current J_ν and produces a second-order correction $f_{\mu\nu}$ to the background electromagnetic field $F_{\mu\nu}$. One has [see Eq. (6.5), (6.10), and Sec. VI B]

$$4\pi J_\nu = \frac{ie}{2}\nabla^\sigma(w_\sigma\bar{w}_\nu - w_\nu\bar{w}_\sigma), \qquad \nabla^\mu f_{\nu\mu} = 4\pi J_\nu. \tag{C3}$$

1. Magnetic field along the z axis

Let us consider a constant magnetic field inside a cylinder of radius R in flat space,

$$ds^2 = -dt^2 + d\rho^2 + \rho^2 d\varphi^2 + dz^2, \qquad A_\varphi = \frac{B}{2}\rho^2,$$
$$\mathcal{B}^z = \frac{1}{\rho}\epsilon^{z\rho\varphi}F_{\rho\varphi} \equiv B > 0, \tag{C4}$$

where $\rho \in [0, R]$. The Eq. (C2) are solved by

$$B = \frac{m_{\rm W}^2}{e}, \qquad w_0 = w_z = 0,$$
$$w_\rho = \frac{i}{\rho}w_\varphi = \exp(-i\varphi)\exp\left(-\frac{m_{\rm W}^2}{4}\rho^2\right); \tag{C5}$$

hence, the magnetic flux in the cylinder is equal to $\pi m_{\rm W}^2 R^2/e$, and the condensate density is

$$\mathrm{w}(\rho) \equiv w^\mu\bar{w}_\mu = 2|w_\rho|^2 = 2\exp\left(-\frac{m_{\rm W}^2}{2}\rho^2\right). \tag{C6}$$

This gives rise to the current with the only nonvanishing component in the azimuthal direction,

$$4\pi J_\varphi = -e\rho(|w_\rho|^2)'_\rho = em_{\rm W}^2\rho^2|w_\rho|^2, \tag{C7}$$

whose sign is opposite to that of the Larmor precession. Therefore, the field $\delta\mathcal{B}$ created by the current rather enhances the background field instead of screening it.

The Maxwell equation (C3) reduces to

$$\frac{1}{\rho}(\rho f^{\varphi\rho})'_\rho = 4\pi J^\varphi = -\frac{e}{\rho}(|w_\rho|^2)'_\rho$$
$$\Rightarrow \delta\mathcal{B}^z = \frac{1}{\rho}f_{\rho\varphi} = e|w_\rho|^2 + \text{const}, \tag{C8}$$

where the constant is fixed by the requirement that the field $\delta\mathcal{B}_z$ should not change the magnetic flux; hence

$$\int_0^R \rho\delta\mathcal{B}^z d\rho = 0 \Rightarrow \delta\mathcal{B}^z = e\left(\frac{1}{2}\mathrm{w}(\rho) - \frac{2-\mathrm{w}(R)}{m_{\rm W}^2R^2}\right). \tag{C9}$$

This field is maximal at $\rho = 0$ where the condensate density $\mathrm{w}(\rho)$ is maximal and where $\delta\mathcal{B}^z > 0$; therefore the background field is enhanced by the condensate (antiscreening). At the cylinder surface, for $\rho = R$, the condensate is minimal, and one has $\delta\mathcal{B}^z < 0$.

2. Magnetic field on a sphere

Let us consider a radial magnetic field in a spacetime with the direct product geometry,

$$ds^2 = -dt^2 + dr^2 + R^2(d\vartheta^2 + \sin^2\vartheta d\varphi^2),$$
$$A_\varphi = -P\cos\vartheta, \qquad \mathcal{B}^r = \frac{F_{\vartheta\varphi}}{R^2\sin\vartheta} = \frac{P}{R^2}, \tag{C10}$$

where $r \in (-\infty, \infty)$ while $R = \text{const}$. The magnetic flux through the two-sphere is $4\pi P$, and we assume for notational simplicity that $P > 0$.

The Eq. (C2) are solved by

$$R^2 = \frac{eP}{m_{\rm W}^2}, \qquad w_0 = w_r = 0, \qquad w_\vartheta = \frac{i}{\sin\vartheta}w_\varphi = (\sin\vartheta)^j,$$
$$j = eP - 1. \tag{C11}$$

The condensate density is $\mathrm{w}(\vartheta) = w^\mu\bar{w}_\mu = (2/R^2)|w_\vartheta|^2$.

The current has only one component in the azimuthal direction,

$$4\pi J_\varphi = -\frac{e}{R^2}\sin\vartheta(|w_\vartheta|^2)'_\vartheta = -\frac{2ej}{R^2}\cos\vartheta|w_\vartheta|^2. \tag{C12}$$

The sign in (C12) agrees with that in (6.21), but in the upper hemisphere, for $0 \le \vartheta \le \pi/2$, it is opposite to that in (C7) because $|w_\vartheta|^2$ increases with ϑ, whereas $|w_\rho|^2$ in (C7) decreases with ρ. This produces the second-order correction for the magnetic field,

$$\delta\mathcal{B}^r = \frac{f_{\vartheta\varphi}}{R^2\sin\vartheta} = \frac{e}{R^2}|w_\vartheta|^2 + \text{const}, \tag{C13}$$

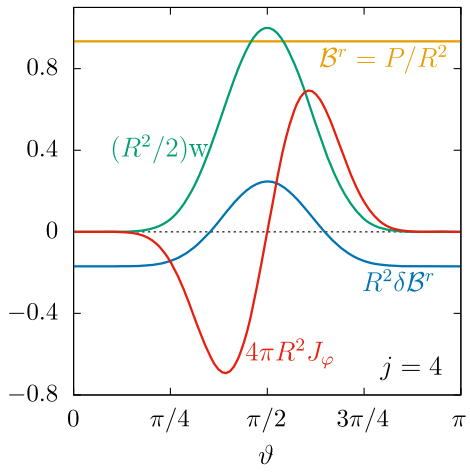


FIG. 25. The magnetic field $\delta\mathcal{B}^r$ in (C14), created by the condensate (C11) with $j = 4$, the corresponding azimuthal current $4\pi J_\varphi$ in (C12), and the condensate density $(R^2/2)\mathrm{w}$ are shown against ϑ. Also shown is the background magnetic $P/R^2 = m_\mathrm{W}^2/e$, which corresponds to the threshold of the electroweak condensation.

where the integration constant is fixed by the requirement that the total magnetic flux should not change, $\oint \delta\mathcal{B}_r d^2\Omega = 0$ (with $d^2\Omega = \sin\vartheta d\vartheta d\varphi$); hence

$$\frac{R^2}{e}\delta\mathcal{B}^r = (\sin\vartheta)^{2j} - \frac{\sqrt{\pi}\Gamma(j+1)}{2\Gamma(j+3/2)}. \tag{C14}$$

Therefore, the total field is

$$\frac{P}{R^2} + \delta\mathcal{B}^r = \frac{m_\mathrm{W}^2}{e} + \frac{e}{R^2}\left((\sin\vartheta)^{2j} - \frac{\sqrt{\pi}\Gamma(j+1)}{2\Gamma(j+3/2)}\right). \tag{C15}$$

For $j = 0$, this reduces to the background field $P/R^2 = m_\mathrm{W}^2/e$. For $j > 0$, the total field is maximal and positive at the equator $\vartheta = \pi/2$, where the condensate is maximal, and it is minimal and negative at the poles $\vartheta = 0, \pi$, where the condensate vanishes (see Fig. 25). Therefore, the background magnetic field is again enhanced by the condensate, and the total field is maximal where the condensate is maximal.

The current flow lines are parallel to $\vartheta = \mathrm{const}$ on the sphere, encircling two vortices centered at the poles $\vartheta = 0, \pi$. The condensate vanishes at the vortex centers, where the total magnetic field $P/R^2 + \delta\mathcal{B}^r$ is minimal, while the condensate is maximal at the equator, where the total magnetic field is maximal. Therefore, these vortices resemble "hollow tubes." This agrees with the analysis in Sec. VI.

The solution (C11)–(C13) is still valid if we set $R = Q = \sqrt{\kappa/2}P$ and replace the geometry in (C10) with the $\mathrm{AdS}_2 \times S^2$ geometry (3.18) of Bertotti-Robinson. The latter describes the near-horizon limit of the extremal RN geometry. Therefore, Eqs. (C11)–(C13) describe the condensate on the extremal RN black hole, hence the bifurcation of the hairy black holes with the extremal RN black holes. This bifurcation corresponds to the rightmost point on the existence diagram in Fig. 22 (right panel), which relates to the maximal value of the charge $Q_\mathrm{max} = 1.29 Q_\mathrm{m} = 2g'\sqrt{\beta}Q_\mathrm{m} = \sqrt{8/\kappa}g'/g$. The same value is obtained by setting $R = Q$ in (C11); indeed,

$$Q^2 = \frac{\kappa}{2}P^2 = \frac{eP}{m_\mathrm{W}^2} \Rightarrow P = \frac{2e}{\kappa m_\mathrm{W}^2} \Rightarrow Q = \sqrt{\frac{\kappa}{2}}P = \sqrt{\frac{8}{\kappa}}\frac{g'}{g}. \tag{C16}$$

APPENDIX D: ESTIMATES OF THE MAGNETIC FIELD STRENGTH

It is instructive to evaluate the dimensionful magnetic field expressed in Teslas (T),

$$\left[\frac{\mathcal{B}}{c}\right] = \frac{1\ \mathrm{kg}}{1\ \mathrm{Coulomb} \times 1\ \mathrm{sec}} = 1\ \mathrm{T} = 10^4\ \mathrm{Gauss}; \tag{D1}$$

($[e\mathcal{B}]$ has the dimension of force). Consider the magnetic field corresponding to the onset of the W condensation, $\mathcal{B} = m_\mathrm{W}^2/e$. Its dimensionful version is

$$\frac{\boldsymbol{\mathcal{B}}}{\boldsymbol{c}} = \frac{1}{\boldsymbol{c}}\frac{(\boldsymbol{m}_W\boldsymbol{c}^2)^2}{\boldsymbol{\hbar c e}} = 1.097 \times 10^{20}\frac{1\ \mathrm{kg}}{1\ \mathrm{Coulomb} \times 1\ \mathrm{sec}} \approx 1.1 \times 10^{20}\ \mathrm{T}, \tag{D2}$$

where we used the numerical values $\boldsymbol{e} = 1.6 \times 10^{-19}$ Coulombs, $\boldsymbol{m}_W\boldsymbol{c}^2 = 80.4\,\mathrm{GeV}$, $1\,\mathrm{GeV} = 1.78 \times 10^{-27}\,\mathrm{kg} \times \boldsymbol{c}^2$, $\boldsymbol{c} = 3 \times 10^8\,\mathrm{m/sec}$ and $\boldsymbol{\hbar} = 1.05 \times 10^{-34}\ \mathrm{kg\,m^2/sec}$.

Consider now the magnetic field of the Dirac monopole, $\mathcal{B} = n/(2er^2)$. Its dimensionful version is $\boldsymbol{\mathcal{B}} = (\boldsymbol{\Phi}_0/\boldsymbol{l}_0)\mathcal{B}$ whereas $r = \boldsymbol{r}/\boldsymbol{l}_0$ while $\boldsymbol{\Phi}_0\boldsymbol{l}_0 = 1/\boldsymbol{g}_0 = \boldsymbol{ee}/(4\pi\alpha) = \boldsymbol{e\hbar c}/\boldsymbol{e}$ [see Eqs. (2.6) and (2.10)]; hence

$$\frac{\boldsymbol{\mathcal{B}}}{\boldsymbol{c}} = n \times \frac{\boldsymbol{\hbar}}{2\boldsymbol{e}} \times \frac{1}{\boldsymbol{r}^2} = \frac{n}{\boldsymbol{r}^2} \times 3.28 \times 10^{-16}\ \mathrm{T} \times \mathrm{m}^2. \tag{D3}$$

Setting here $\boldsymbol{r} = 1.13 \times \sqrt{|n|}\boldsymbol{l}_0$ according to (4.8) with $\boldsymbol{l}_0 = 1.53 \times 10^{-18}\mathrm{m}$ yields again the same value as in (D2). Setting $\boldsymbol{r}$ to be the Sun's radius, $\boldsymbol{r} = \boldsymbol{R}_\odot \approx 6.96 \times 10^8$ m, and choosing $n = 1.6 \times 10^{32}$, which corresponds to the charge of the maximally hairy black hole, yields

$$\frac{\boldsymbol{\mathcal{B}}}{\boldsymbol{c}} = n \times \frac{\boldsymbol{\hbar}}{2\boldsymbol{e}} \times \frac{1}{\boldsymbol{R}_\odot^2} = n \times 6.77 \times 10^{-34}\,\mathrm{T} \approx 0.1\,\mathrm{T} \approx 10^3\ \mathrm{Gauss}. \tag{D4}$$

Therefore, a magnetic charge with $n = 1.6 \times 10^{32}$ placed at the center of the Sun would create at the surface a magnetic field of $\approx 10^3$ Gauss. For comparison, the average magnetic field at the Sun's surface is ~ 1 Gauss, but that in the sunspots can reach $2 - 4 \times 10^3$ Gauss.

APPENDIX E: HORIZON LIMIT OF EXTREMAL BLACK HOLES

The extremal hairy solutions in phase I reduce, in the vicinity of the horizon, to the extremal RNdS solution, (3.1)–(3.2), (3.19), and (3.23)–(3.25), up to small corrections that vanish at the horizon. To determine these corrections, it is convenient to transform the solution to coordinates similar to those used in (3.17) for the extremal RN case.

The geometry of the extremal hairy solutions is described by the line element (7.2), with $\mathrm{N}(\mathrm{r})$ given by (8.2). Let us perform the coordinate transformation (7.3), assuming that in the new gauge, we have $\tilde{\mathrm{N}} = 1/\tilde{\mathrm{r}}^2$, and denote the new radial coordinate as $\tilde{\mathrm{r}} = \eta$. This amounts to setting

$$d\eta = \frac{d\mathrm{r}}{\mathrm{r}\sqrt{\mathrm{N}}} = \frac{d\mathrm{r}}{\mathrm{k}(\mathrm{r})(\mathrm{r}-\mathrm{r_H})}$$
$$\Rightarrow \eta - \eta_0 = \frac{1}{\mathrm{k}(\mathrm{r})}\ln\frac{\mathrm{r}-\mathrm{r_H}}{\mathrm{r_H}} + \int_{\mathrm{r_H}}^{\mathrm{r}} \frac{\mathrm{k}'}{\mathrm{k}^2(\mathrm{r})}\ln\frac{\mathrm{r}-\mathrm{r_H}}{\mathrm{r_H}}\,d\mathrm{r}. \tag{E1}$$

As $\mathrm{r} \to \mathrm{r_H}$, we have $\eta \to -\infty$.

Re-expressing the metric amplitudes U, K, S in (7.2) in terms of three other functions, $\delta\mathrm{U}, \delta\mathrm{K}, \delta\mathrm{S}$, as

$$e^{2\mathrm{U}} = \mathrm{r_H^2}\eta^2 e^{2\lambda\eta + 2\delta\mathrm{U}}, \qquad \eta^2 e^{2\mathrm{K}-2\mathrm{U}} = \mathrm{r_H^2} e^{2\delta\mathrm{K}},$$
$$\eta^2 e^{2\mathrm{S}-2\mathrm{U}} = \mathrm{r_H^2} e^{2\delta\mathrm{S}}, \tag{E2}$$

with a constant λ, the line element takes the form

$$ds^2 = \mathrm{r_H^2}\{-e^{2\lambda\eta}e^{2\delta\mathrm{U}}dt^2 + e^{2\delta\mathrm{K}}(d\eta^2 + d\vartheta^2) + e^{2\delta\mathrm{S}}\sin^2\vartheta d\varphi^2\}. \tag{E3}$$

We also re-express the electroweak amplitudes in (7.29) and (7.31) as

$$H_1 = \delta H_1, \quad H_2 = 1 + \delta H_2, \quad H_3 = \delta H_3, \quad H_4 = 1 + \delta H_4,$$
$$y = \delta y, \quad \phi_1 = \delta\phi_1, \quad \phi_1 = \delta\phi_2. \tag{E4}$$

In these formulas, the deviations $\delta\mathrm{U}, \ldots, \delta\phi_2$ are not necessarily small, but they approach zero at the horizon, where $\eta \to -\infty$. Setting them to zero, $\delta\mathrm{U} = \delta\mathrm{S} = \ldots = \delta\phi_2 = 0$, all field equations are satisfied provided that the constants λ and $\mathrm{r_H}$ obey the relations

$$\mathrm{r_H} = r_{\mathrm{ex}}, \qquad \lambda^2 = 1 - \frac{\kappa\beta}{4}r_{\mathrm{ex}}^2 = \sqrt{1 - \frac{\beta\kappa^2 n^2}{16 g'^2}}. \tag{E5}$$

These are precisely the same relations as for the extremal RNdS solution in (3.24). The argument of the square root is positive for $|Q| < Q_{\mathrm{m}}$, which applies to all extremal hairy solutions in phase I, where $|Q| \le 0.6 Q_{\mathrm{m}}$. This yields

$$ds^2 = r_{\mathrm{ex}}^2\{-e^{2\lambda\eta}dt^2 + d\eta^2 + d\vartheta^2 + \sin^2\vartheta d\varphi^2\},$$
$$B = -\frac{n}{2}\cos\vartheta d\varphi, \qquad \mathrm{W} = \Phi = 0, \tag{E6}$$

which is an exact solution for any $\eta \in (-\infty, \infty)$. This is the same as the horizon limit of the extremal RNdS solution in (3.26).

In the vicinity of the horizon, the deviations $\delta\mathrm{U}, \ldots, \delta\phi_2$ are expected to be small, rather than zero. Therefore, one can expand the field equations around the limiting solution (E6), assuming η to be large and negative. This yields, in the first perturbative order, linear equations for the deviations. These equations split into three independent groups.

1. The first group of perturbations

This group contains the three metric amplitudes as well as δy, whose dependence on η and ϑ can be separated as follows:

$$\delta\mathrm{U} = S_{\mathrm{U}}(\vartheta)e^{\lambda\eta}, \quad \delta\mathrm{K} = S_{\mathrm{K}}(\vartheta)e^{\lambda\eta}, \quad \delta\mathrm{S} = S_{\mathrm{S}}(\vartheta)e^{\lambda\eta},$$
$$\delta y = S_y(\vartheta)e^{\lambda\eta}. \tag{E7}$$

The functions $S_{\mathrm{U}}(\vartheta), S_{\mathrm{K}}(\vartheta), S_{\mathrm{S}}(\vartheta), S_y(\vartheta)$ satisfy equations, whose simplest solution is ϑ independent,

$$S_{\mathrm{K}} = S_{\mathrm{S}} = \mathrm{const}, \quad S_{\mathrm{U}} = -\frac{\lambda^2+2}{3\lambda^2}S_{\mathrm{S}}, \quad S_y = 0. \tag{E8}$$

The condition $S_{\mathrm{K}} = S_{\mathrm{S}}$ implies that the geometry remains spherically symmetric in the first perturbative order. One can set $S_{\mathrm{S}} = 1$ by adjusting the integration constant η_0 in (E1) and then absorbing the constant $e^{\lambda\eta_0}$ by redefining the time coordinate. As a result, the Schwarzschild radius of the two-sphere, $r = \sqrt{\mathrm{g}_{\vartheta\vartheta}}$, is no longer constant:

$$r = r_{\mathrm{ex}}e^{\delta\mathrm{S}}, \quad \text{where } \delta\mathrm{S} = e^{\lambda\eta} = \ln\frac{r}{r_{\mathrm{ex}}} \approx \frac{r}{r_{\mathrm{ex}}} - 1. \tag{E9}$$

The same results can be obtained by directly applying (E1) to the line element of the extremal RNdS solution (3.25).

2. The second group of perturbations

This group includes the two Higgs amplitudes, which can be expressed as

$$\delta\phi_1 = S_1(\vartheta)e^{\sigma\eta}, \qquad \delta\phi_2 = S_2(\vartheta)e^{\sigma\eta}, \tag{E10}$$

where σ is a constant. The equations governing S_1 and S_2 are given by

$$\left(l(l+1)+\frac{d^2}{d\vartheta^2}+\cot\vartheta\frac{d}{d\vartheta}-\frac{\nu^2}{\sin^2\vartheta}+\frac{3\nu^2-1}{4}\right)S_1-\left(\frac{d}{d\vartheta}+\frac{1-\nu^2}{2}\cot\vartheta\right)S_2=0,$$
$$\left(l(l+1)+\frac{d^2}{d\vartheta^2}+\cot\vartheta\frac{d}{d\vartheta}-\frac{\nu^2+1}{4}\right)S_2+\left(\frac{d}{d\vartheta}+\frac{1+\nu^2}{2}\cot\vartheta\right)S_1=0, \tag{E11}$$

where

$$\nu=-\frac{n}{2},\qquad l(l+1)=\sigma^2+\lambda\sigma+\frac{\beta r_{\rm ex}^2}{4}. \tag{E12}$$

This defines the eigenvalue problem to determine l, whose solution is

$$l=\frac{\sqrt{1+2|\nu|}-1}{2},\quad S_1(\vartheta)=-\frac{2}{|\nu|+1}\frac{d}{d\vartheta}S_2(\vartheta), \tag{E13}$$

where

$$\left(\frac{d^2}{d\vartheta^2}-|\nu|\cot\vartheta\frac{d}{d\vartheta}+\frac{1-\nu^2}{4}\right)S_2=0$$
$$\Rightarrow S_2=\left(\sin\frac{\vartheta}{2}\right)^{|\nu|+1}+\left(\cos\frac{\vartheta}{2}\right)^{|\nu|+1}. \tag{E14}$$

As a result, the exponent σ in (E10) is given by

$$\sigma=\frac{-\lambda+\sqrt{\lambda^2+|n|-\beta r_{\rm ex}^2}}{2}, \tag{E15}$$

and

$$\phi_1\propto\phi_2\propto e^{\sigma\eta}=\left(\ln\frac{r}{r_{\rm ex}}\right)^{\sigma/\lambda}\approx\left(\frac{r-r_{\rm ex}}{r_{\rm ex}}\right)^{\sigma/\lambda}. \tag{E16}$$

When the magnetic charge $|n|$ increases, σ grows as $\sqrt{|n|}$, while λ decreases. Therefore, the Higgs field approaches zero faster and faster in the vicinity of the horizon, and the size of the false vacuum region around the horizon increases.

If $|n|\ll 1/\sqrt{\kappa}$, then the horizon size $r_{\rm ex}\ll 1$, and the spacetime geometry at the electroweak scale, where $r\sim 1$, is essentially flat. In that case, the size of the vacuum region can be estimated to be $\sim\sqrt{|n|}$, as expressed by Eq. (5.24) in [59].

The relation (E16) implies that the components of the unit vector $n^a=(\Phi^\dagger\tau^a\Phi)/(\Phi^\dagger\Phi)$ used in (2.26) to define the electromagnetic field do not depend on the radial coordinate:

$$n^1=\frac{2S_1S_2}{(S_1)^2+(S_2)^2},\quad n^2=0,\quad n^3=\frac{(S_1)^2-(S_2)^2}{(S_1)^2+(S_2)^2}, \tag{E17}$$

where we used Φ in the gauge (7.22). These relations are exact at the horizon, while in the vicinity of the horizon, they may receive corrections only in higher perturbative orders.

This allows us to determine the horizon value of the electromagnetic field. Since the perturbations $\delta H_1,\delta H_2,\delta H_3,\delta H_4$ approach zero at the horizon, it follows from (7.22) and (7.27) that the SU(2) gauge field strength vanishes at the horizon, $\mathrm{W}^a_{\mu\nu}=0$. The Nambu field $\mathcal{F}_{\mu\nu}$, defined in (2.26), then reduces to the U(1) hypercharge field, up to a constant factor.

Therefore, the only nonzero components of the Nambu field at the horizon are $\mathcal{F}_{\vartheta\varphi}=-\mathcal{F}_{\varphi\vartheta}$, where

$$\mathcal{F}_{\vartheta\varphi}=\frac{g}{g'}B_{\vartheta\varphi}=\frac{g}{g'}\frac{n}{2}\sin\vartheta=g^2\frac{n}{2e}\sin\vartheta=g^2P\sin\vartheta. \tag{E18}$$

This corresponds to the purely radial magnetic field of total flux $4\pi g^2P$, created by the magnetic charge g^2P inside the black hole. The remaining part of the charge g'^2P is contained in the black hole hair.

The 't Hooft field, $F_{\mu\nu}=\mathcal{F}_{\mu\nu}-e\psi_{\mu\nu}$, defined in (2.37), includes the condensate tensor $\psi_{\mu\nu}$, which is constructed from the unit vector n^a according to (2.35). Using n^a in (E17) and the SU(2) field W^a_μ in the gauge (7.22), we find that the only components of the condensate which do not vanish at the horizon are $\psi_{\vartheta\varphi}=-\psi_{\varphi\vartheta}$, where

$$-e\psi_{\vartheta\varphi}=g'^2\frac{n}{2e}\times\frac{|n|\left(\sin\frac{\vartheta}{2}\cos\frac{\vartheta}{2}\right)^{|n|-1}}{\left[\left(\cos\frac{\vartheta}{2}\right)^{|n|}+\left(\sin\frac{\vartheta}{2}\right)^{|n|}\right]^2}. \tag{E19}$$

It is instructive to compare this with the formula $\psi_{\vartheta\varphi}\sim(\sin\vartheta)^{|n|-1}$, which follows from (6.14) and (6.15) in the axially symmetric case [when $c_{\rm k}=\delta_{0\rm k}$ in (6.14)]. This formula was obtained using perturbation theory at the bifurcation with the RN solution. In contrast, the relation in (E19) is nonperturbative and corresponds to the fully nonlinear solution restricted to the event horizon. According to (6.14) and (6.15), the value of $|\psi_{\vartheta\varphi}|$ (or more precisely, $|\psi_{\vartheta\varphi}|/\sin\vartheta$) can be interpreted as a measure of the condensate strength. Remarkably, both the perturbative and nonperturbative expressions for the condensate exhibit the same qualitative behavior: they reach their maximum at the equator and vanish at the poles.

The flux of $\psi_{\mu\nu}$ is given by

$$-e\oint \psi_{\vartheta\varphi}d\vartheta d\varphi = 4\pi g'^2 P. \tag{E20}$$

As a result, the horizon value of the 't Hooft field is the sum of (E18) and (E19),

$$F_{\vartheta\varphi} = \frac{g}{g'}B_{\vartheta\varphi} - e\psi_{\vartheta\varphi} = g^2\frac{n}{2e}\sin\vartheta + g'^2\frac{n}{2e}\times\frac{|n|\left(\sin\frac{\vartheta}{2}\cos\frac{\vartheta}{2}\right)^{|n|-1}}{\left[\left(\cos\frac{\vartheta}{2}\right)^{|n|}+\left(\sin\frac{\vartheta}{2}\right)^{|n|}\right]^2}, \tag{E21}$$

whose flux is $4\pi P$. Since the two form $F_{\mu\nu}$ is closed, its flux is independent of the integration surface. As a result, the flux through a two-sphere at spatial infinity is the same as that through the horizon, implying that the entire magnetic charge is contained within the black hole. In contrast, for the Nambu field (E18), the flux through the horizon is $4\pi g^2 P$, while the flux at infinity remains $4\pi P$. The difference is $4\pi g'^2 P$, corresponding to the magnetic charge $g'^2 P$ distributed outside the black hole.

The Z field, defined by (2.37), has nonzero components

$$Z_{\vartheta\varphi} = -Z_{\varphi\vartheta} = B_{\vartheta\varphi} + g^2\psi_{\vartheta\varphi}. \tag{E22}$$

Its horizon flux vanishes, as expected, since the two form $Z_{\mu\nu}$ is also closed, and its flux at infinity is zero because this field is massive.

Let us now consider the current densities. Taking the divergence of the Nambu field (E18) gives zero, meaning that the Nambu current vanishes at the horizon. The magnetic charge density in (2.51) is proportional to the radial derivative of $\psi_{\vartheta\varphi}$, which is also zero at the horizon. Therefore, both the Nambu current density $\mathcal{J}^\mu$ and the magnetic charge density $\tilde{\mathcal{J}}^0$ vanish at the horizon, although they deviate from zero at some distance away, as indicated by our numerics.

On the other hand, taking the divergence of the 't Hooft field (E21) gives a nonzero value of the azimuthal current density at the horizon:

$$4\pi r_{\rm ex}^2 J_\varphi = -\sin\vartheta\left(\frac{F_{\vartheta\varphi}}{\sin\vartheta}\right)'_\vartheta = -\frac{g'n|n|}{g2^{|n|}}\sin\vartheta\left(\frac{(\sin\vartheta)^{|n|-2}}{\left[\left(\cos\frac{\vartheta}{2}\right)^{|n|}+\left(\sin\frac{\vartheta}{2}\right)^{|n|}\right]^2}\right)'_\vartheta. \tag{E23}$$

According to our numerics (see Fig. 19, right panel) the current density is maximal at the horizon and starts to decrease as we move away from it. Notice that the formulas (E18)–(E23) do not contain κ.

3. The third group of perturbations

This group contains four SU(2) amplitudes that we re-express as

$$\delta H_1 = e^{q\eta}h_1(\vartheta),\quad \delta H_2 = e^{q\eta}h_2(\vartheta),\quad \delta H_3 = e^{q\eta}h_3(\vartheta),\quad \delta H_4 = e^{q\eta}h_4(\vartheta), \tag{E24}$$

where q is a constant. The corresponding equations for the perturbations are

$$\begin{aligned}
&\left(\frac{d^2}{d\vartheta^2}+\cot\vartheta\frac{d}{d\vartheta}-\frac{\nu^2}{\sin^2\vartheta}+q^2\right)h_1 + q\cot\vartheta h_2 + q\nu^2 h_3 - q\nu^2\cot\vartheta h_4 = 0,\\
&\left(\frac{d^2}{d\vartheta^2}-\frac{\nu^2}{\sin^2\vartheta}+q(q+\lambda)\right)h_2 + \lambda\frac{d}{d\vartheta}h_1 - \nu^2\left(\frac{d}{d\vartheta}+2\cot\vartheta\right)h_3 + \nu^2\left(\cot\vartheta\frac{d}{d\vartheta}+\cot^2\vartheta-1\right)h_4 = 0,\\
&\left(\frac{d^2}{d\vartheta^2}+\cot\vartheta\frac{d}{d\vartheta}-\frac{1}{\sin^2\vartheta}+q(q+\lambda)-1\right)h_3 - \lambda h_1 - \cot\vartheta h_2 + \left(2\frac{d}{d\vartheta}+\cot\vartheta\right)h_4 = 0,\\
&\left(\frac{d^2}{d\vartheta^2}+\cot\vartheta\frac{d}{d\vartheta}-\frac{1}{\sin^2\vartheta}+q(q+\lambda)-1\right)h_4 + \lambda\cot\vartheta h_1 + \cot^2\vartheta h_2 - \left(2\frac{d}{d\vartheta}+\cot\vartheta\right)h_3 = 0.
\end{aligned} \tag{E25}$$

By using the transformations

$$h_4(\vartheta) = \cos\vartheta\tilde{h}_3(\vartheta) + \sin\vartheta\tilde{h}_4(\vartheta),\qquad h_3(\vartheta) = -\sin\vartheta\tilde{h}_3(\vartheta) + \cos\vartheta\tilde{h}_4(\vartheta), \tag{E26}$$

the system of equations (E25) splits into three coupled equations involving $h_1, h_2, \tilde{h}_3$, plus one independent equation for $\tilde{h}_4$:

$$\left(\frac{d^2}{d\vartheta^2}+\cot\vartheta\frac{d}{d\vartheta}-\frac{1}{\sin^2\vartheta}+q(q+\lambda)\right)\tilde{h}_4=0. \quad \text{(E27)}$$

The solution to this equation is given by

$$\tilde{h}_4=C_4P_l^1(\cos\vartheta),\quad (q+\lambda)=l(l+1),\ \ l=1,2,\ldots, \quad \text{(E28)}$$

where $P_l^1(\cos\vartheta)$ are the Legendre polynomials and C_4 is an integration constant.

By setting $h_1=h_2=\tilde{h}_3=0$, and using Eq. (E26), we obtain

$$h_4=C_4\sin\vartheta P_l^1(\cos\vartheta),\quad h_3=C_4\cos\vartheta P_l^1(\cos\vartheta), \quad \text{(E29)}$$

and the value of q is

$$q=\frac{-\lambda+\sqrt{\lambda^2+4l(l+1)}}{2}, \quad \text{(E30)}$$

where C_4 is an integration constant.

The analysis of the remaining equations for $h_1,h_2,\tilde{h}_3$ involves applying the gauge fixing condition (7.33), which now simplifies to

$$qh_1(\vartheta)=h_2'(\vartheta). \quad \text{(E31)}$$

This allows us to eliminate h_1 since its equation becomes a differential consequence of the two other equations. The remaining equations reduce to

$$\left(\frac{d^2}{d\vartheta^2}+\cot\vartheta\frac{d}{d\vartheta}-\frac{1}{\sin^2\vartheta}+q(q+\lambda)\right)\tilde{h}_3+\frac{1}{\sin\theta}\left(\frac{\lambda}{q}\frac{d}{d\vartheta}+\cot\vartheta\right)h_2=0,$$
$$\left((q+\lambda)\frac{d^2}{d\vartheta^2}+q^2(q+\lambda)-\frac{q\nu^2}{\sin^2\vartheta}\right)h_2+\frac{q\nu^2}{\sin\vartheta}\left(\frac{d}{d\vartheta}+\cot\vartheta\right)\tilde{h}_3=0. \quad \text{(E32)}$$

Unfortunately, we were unable to find an exact solution of these equations, although it is clear that the solution should be expressible in terms of Legendre polynomials. We leave this problem for future work.

APPENDIX F: VORTICES

Vortices are frequently mentioned in the main text, and for completeness, we provide in this appendix a brief overview of the vortex solutions that may be relevant to our analysis. The results presented in Appendixes F 1 and F 2 are known and can be found in the literature, while Appendix F 3 contains observations that, to the best of our knowledge, are new.

1. Vortices in the Abelian Higgs model

Vortices were originally described by Abrikosov [91] within the phenomenological theory of superconductivity developed by Ginzburg and Landau [92]. Some time later, exactly the same solutions were rediscovered by Nielsen and Olesen in the context of relativistic field theory [93]. These vortices arise in a model that includes an Abelian vector field $\mathcal{C}_\mu$ and a complex scalar ϕ, with the Lagrangian

$$\mathcal{L}=-\frac{1}{4}\mathcal{C}_{\mu\nu}\mathcal{C}^{\mu\nu}-\overline{\mathcal{D}_\mu\phi}\mathcal{D}^\mu\phi-\frac{\beta}{8}(|\phi|^2-1)^2. \quad \text{(F1)}$$

Here $\mathcal{C}_{\mu\nu}=\partial_\mu\mathcal{C}_\nu-\partial_\nu\mathcal{C}_\mu$ and $\mathcal{D}_\mu\phi=(\nabla_\mu-iq\mathcal{C}_\mu)\phi$ with q being the electric charge. The theory is invariant under U(1) gauge transformations,

$$\mathcal{C}_\mu\to\mathcal{C}_\mu+\frac{1}{q}\partial_\mu\alpha,\qquad \phi\to e^{i\alpha}\phi. \quad \text{(F2)}$$

The equations of the theory,

$$\nabla^\mu\mathcal{C}_{\mu\nu}=iq(\bar{\phi}\mathcal{D}_\nu\phi-\phi\overline{\mathcal{D}_\nu\phi}),\qquad \mathcal{D}_\mu\mathcal{D}^\mu\phi=\frac{\beta}{4}(|\phi|^2-1)\phi, \quad \text{(F3)}$$

admit solutions describing a localized magnetic flux along the z direction. Passing to cylindrical coordinates, where the metric is $ds^2=-dt^2+d\rho^2+\rho^2d\varphi^2+dz^2$, and setting

$$\mathcal{C}_\mu dx^\mu=-\mathrm{v}(\rho)d\varphi,\qquad \phi=f(\rho), \quad \text{(F4)}$$

Equation (F3) reduce to

$$\rho\left(\frac{\mathrm{v}'}{\rho}\right)'=2q^2f^2\mathrm{v},\qquad \frac{1}{\rho}(\rho f')'=q^2\frac{\mathrm{v}^2}{\rho^2}f+\frac{\beta}{4}(f^2-1)f. \quad \text{(F5)}$$

These equations admit globally regular solutions with the boundary conditions

$$\mathrm{v}(0)\leftarrow\mathrm{v}(\rho)\to 0,\qquad 0\leftarrow f(\rho)\to 1\quad\text{as}\quad 0\leftarrow\rho\to\infty. \quad \text{(F6)}$$

The value of v(0) can be arbitrary, but for generic values, the vector field in (F4) is singular at the symmetry axis,

since the azimuthal component $\mathcal{C}_\varphi$ does not vanish as $\rho \to 0$. However, if $\mathrm{v}(0) = k/q$ with $k \in \mathbb{Z}$, then performing the gauge transformation (F2) with $\alpha = k\varphi$ brings the fields to the form

$$\mathcal{C}_\mu dx^\mu = \left(\frac{k}{q} - \mathrm{v}(\rho)\right) d\varphi, \quad \phi = f(\rho) e^{ik\varphi} \text{ with } k \in \mathbb{Z}. \tag{F7}$$

The fields now vanish at $\rho = 0$, so the singularity is gauged away. A similar "desingularization" procedure will be used below for other vortex solutions.

The magnetic flux is determined by the asymptotic value of $\mathcal{C}_\varphi$ in (F7),

$$\Psi_{\mathcal{C}} = \oint_{\partial \mathbb{R}^2} \mathcal{C}_k dx^k = \frac{2\pi k}{q}. \tag{F8}$$

The vortices have a finite energy per unit length,

$$E[q,k] = 2\pi \int_0^\infty \left(\frac{\mathrm{v}'^2}{2\rho^2} + f'^2 + q^2 \frac{\mathrm{v}^2 f^2}{\rho^2} + \frac{\beta}{8}(f^2-1)^2\right) \rho d\rho. \tag{F9}$$

2. Electroweak vortices

Returning to the parametrization (7.22) of the electroweak fields and setting

$$F_1 = F_2 = 0, \qquad \nu F_3 = -v_3(\rho), \qquad \nu F_4 = v_1(\rho), \qquad \nu Y = -v(\rho), \qquad \phi_1 = f_1(\rho), \qquad \phi_2 = f_2(\rho), \tag{F10}$$

the electroweak equations (2.17) reduce to

$$\begin{aligned}
\rho\left(\frac{v'}{\rho}\right)' &= \frac{g'^2}{2}\{(v+v_3)f_1^2 + 2v_1 f_1 f_2 + (v-v_3)f_2^2\},\\
\rho\left(\frac{v_1'}{\rho}\right)' &= \frac{g^2}{2}\{v_1(f_1^2+f_2^2) + 2v f_1 f_2\},\\
\rho\left(\frac{v_3'}{\rho}\right)' &= \frac{g^2}{2}\{(v_3+v)f_1^2 + (v_3-v)f_2^2\},\\
\frac{1}{\rho}(\rho f_1')' &= \left\{\frac{1}{4\rho^2}[(v+v_3)^2 + v_1^2] + \frac{\beta}{4}(f_1^2+f_2^2-1)\right\} f_1 + \frac{v v_1}{2\rho^2} f_2\\
\frac{1}{\rho}(\rho f_2')' &= \left\{\frac{1}{4\rho^2}[(v-v_3)^2 + v_1^2] + \frac{\beta}{4}(f_1^2+f_2^2-1)\right\} f_2 + \frac{v v_1}{2\rho^2} f_1,
\end{aligned} \tag{F11}$$

plus a first-order constraint, that is compatible with the other equations:

$$\frac{1}{\rho^2}(v_1 v_3' - v_3 v_1') + g^2(f_2 f_1' - f_1 f_2') = 0. \tag{F12}$$

It is sufficient to impose this constraint only at $\rho = 0$. These equations (actually a more general system including also a nonzero F_2) were originally obtained in Ref. [94], where one can find the analysis of the constraint (F12).

a. Z strings

Setting in (F11)

$$\begin{aligned}
&v = g'^2 \mathrm{v}(\rho), \qquad v_1 = 0, \qquad v_3 = -g^2 \mathrm{v}(\rho),\\
&f_1 = 0, \qquad f_2 = f(\rho),
\end{aligned} \tag{F13}$$

the equations reduce to (F5) with $q = 1/2$. Their solution determines the electroweak fields

$$\mathrm{W} = g^2 \mathrm{T}_3 \mathrm{v}(\rho) d\varphi, \quad B = -g'^2 \mathrm{v}(\rho) d\varphi, \quad \Phi = \begin{pmatrix} 0 \\ f(\rho) \end{pmatrix}. \tag{F14}$$

This fields can be desingularized by choosing $\mathrm{v}(0) = 2k$ and performing the gauge transformation (2.15) and (2.16) with $\mathfrak{V} = \exp\{i(g'^2 - g^2\tau_3)k\varphi\}$. This converts the fields to

$$\begin{aligned}
&\mathrm{W} = g^2 \mathrm{T}_3(\mathrm{v}(\rho) - 2k) d\varphi, \qquad B = g'^2(2k - \mathrm{v}(\rho)) d\varphi,\\
&\Phi = \begin{pmatrix} 0 \\ f(\rho) e^{ik\varphi} \end{pmatrix},
\end{aligned} \tag{F15}$$

in which form they vanish at $\rho = 0$.

Using (2.35) yields $\psi_{\mu\nu} = 0$, implying that the definitions of Nambu and 't Hooft give the same result for the physical fields, $\mathcal{F}_{\mu\nu} = F_{\mu\nu} = 0$, with the only nonzero component of $\mathcal{Z}_{\mu\nu} = Z_{\mu\nu}$ being $Z_{\rho\varphi} = -Z_{\varphi\rho} = -\mathrm{v}'(\rho)$. This determines the fluxes

$$\Psi_F = 0, \qquad \Psi_Z = 4\pi k. \tag{F16}$$

The solution was discovered in [95]. Since it contains only the massive Z field and no usual magnetic field, it is called the Z string.

b. W strings

Setting in (F11)

$$v = v_3 = f_1 = 0, \qquad v_1 = g\mathrm{v}(\rho), \qquad f_2 = f(\rho), \tag{F17}$$

the equations again reduce to (F5), but this time with $q = g/2$. Their solution determines the electroweak fields,

$$B = 0, \quad \mathrm{W} = -\mathrm{T}_1 g\mathrm{v}(\rho)d\varphi, \quad \Phi = \begin{pmatrix} 0 \\ f(\rho) \end{pmatrix}. \tag{F18}$$

The singularity at the axis can be removed by setting $\mathrm{v}(0) = 2k/g$ and performing the gauge transformation (2.15) and (2.16) generated by $\mathfrak{V} = \exp\{i\tau_1 k\varphi\}$, which yields

$$\mathrm{W} = \mathrm{T}_1 \mathrm{W}^1_\mu dx^\mu = \mathrm{T}_1(2k - g\mathrm{v}(\rho))d\varphi, \quad \Phi = f(\rho)\begin{pmatrix} i\sin(k\varphi) \\ \cos(k\varphi) \end{pmatrix}, \tag{F19}$$

in which form the fields vanish at $\rho = 0$. Getting back to the gauge (F18) and using (2.35) shows that $\mathcal{W}_\mu = 0$; therefore, both the magnetic and Z fields vanish:

$$\Psi_F = \Psi_Z = 0 \tag{F20}$$

(this corrects the values quoted in [94]). The solution can be characterized by a nonzero W flux,

$$2\pi \int_0^\infty \mathrm{W}_{\rho\varphi} d\rho = 4\pi k \mathrm{T}_1, \tag{F21}$$

which is, however, not gauge invariant. This solution was obtained in [96].

c. Dressed Z strings

The Z strings and W strings are *Abelian* and correspond to solutions of the Abelian Higgs model (F1) embedded into the electroweak theory. The Eq. (F11) also admit more general solutions, which can be viewed as Z strings containing a condensate at their core. Such "dressed" Z strings were discussed qualitatively long ago [97–99], and later they were explicitly obtained in Ref. [94] (see Sec. IX.3 of that article).

These solutions are characterized by the boundary conditions at $0 \leftarrow \rho \rightarrow \infty$ (our notation is related to that of [94] by the replacement $v_3 \to -v_3$, $f_1 \leftrightarrow f_2$):

$$\begin{aligned} &2k - m \leftarrow v \rightarrow c, \qquad 0 \leftarrow v_1 \rightarrow -c\sin\gamma, \qquad -m \leftarrow v_3 \rightarrow c\cos\gamma, \\ &q\rho^{|k-m|} \leftarrow f_1 \rightarrow \sin\frac{\gamma}{2}, \qquad a\rho^k \leftarrow f_2 \rightarrow \cos\frac{\gamma}{2}. \end{aligned} \tag{F22}$$

Here k is an integer that we assume to be positive for simplicity; one has $m = 1, 2, \ldots 2k$, while c, γ, a, q are real.

The parameter γ can be called a vacuum angle. If $\gamma = 0$, then $f_1 = 0$, and the solution corresponds to the Z string configuration (F13), but with shifted values of v, v_3:

$$v = g'^2\mathrm{v}(\rho) + c, \qquad v_1 = 0, \qquad v_3 = -g^2\mathrm{v}(\rho) + c, \qquad f_1 = 0, \qquad f_2 = f(\rho). \tag{F23}$$

Here $\mathrm{v}(\rho), f(\rho)$ are the same as for the Z string, so that $\mathrm{v}(0) = 2k$, while $c = 2kg^2 - m$. This is the Z string (F14), gauge transformed by (2.15) and (2.16) with $\mathfrak{V} = \exp\{-ic(1+\tau_3)\varphi/2\}$. Therefore, for the Z string the second integer m is generated by the gauge transformation.

The dressed Z strings correspond to more general solutions with $v_1 \neq 0$ and $f_1 \neq 0$. They are labeled by pairs (k, m), and they are physically different for different m. For some choices of (k, m) these solutions exist only for nonphysical values of the theory parameters θ_W, β [94]. Choosing the physical values $\sin^2\theta_\mathrm{W} = 0.223$ and $\beta = 1.88$, we were able to reproduce such solutions for $k = 4, 5, 6, \ldots$ with $m = 2k - 1$. However, they probably exist also for other values of (k, m). Their profiles for $k = 4$, $m = 7$ are shown in Fig. 26.

These solutions can be desingularized with the gauge transformation (2.15) and (2.16) generated by $\mathfrak{V} = \exp(ik\varphi)\exp\{-i(1+\tau_3)m\varphi/2\}$. This brings the fields to the form

$$\mathrm{W} = \{-v_1\tilde{\mathrm{T}}_1 - \mathrm{T}_3(v_3 + m)\}d\varphi, \qquad B = (2k - m - v)d\varphi, \qquad \Phi = \begin{pmatrix} f_1 e^{i(k-m)\varphi} \\ f_2 e^{ik\varphi} \end{pmatrix}, \tag{F24}$$

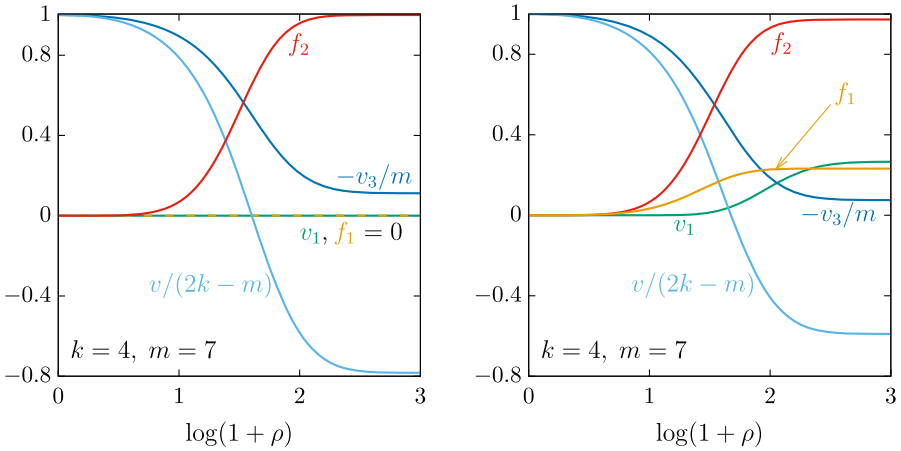


FIG. 26. The Z string (left) and the dressed Z string (right) with $k = 4$, $m = 7$ for the physical values $\sin^2\theta_{\rm w} = 0.223$, $\beta = 1.88$. One has $\Psi_F = 0$ and $\Psi_Z = 4\pi k$ for the Z string, whereas for the dressed solution $\Psi_F \approx 0.9 \times 4\pi m \times g'^2/e$ and $\Psi_Z = 4\pi(k-m)$.

with $\tilde{\rm T}_1 = {\rm T}_1\cos(m\varphi) + {\rm T}_2\sin(m\varphi)$. In view of the boundary conditions (F22), these fields vanish at $\rho = 0$.

The dressed solutions carry nonzero magnetic and Z fluxes. To compute them, we consider the unit vector n^a defined in (2.27). It reduces to $n^a = -\delta^a_3$ for Z strings, while for the dressed solutions one has for $0 \leftarrow \rho \to \infty$

$$\delta^a_3 \leftarrow n^a = (n^1, n^2, n^3) = \left(\frac{2f_1f_2}{f_1^2+f_2^2}, 0, \frac{f_1^2-f_2^2}{f_1^2+f_2^2}\right) \to (\sin\gamma, 0, -\cos\gamma); \tag{F25}$$

hence, n^a rotates by an angle $\pi - \gamma$ close to the origin, where f_1 approaches zero slower than f_2. Using Eq. (2.35) yields

$$\begin{aligned} n^a {\rm W}^a_{\rho\varphi} &= -n^1(v_1)' - n^3(v_3)', \\ g^2\psi_{\rho\varphi} &= (n^1(n^3)' - n^3(n^1)')(v_1 n^3 - v_3 n^1), \\ \mathcal{W}_\varphi &= -n^1 v_1 - n^3 v^3; \end{aligned} \tag{F26}$$

hence,

$$\mathcal{W}_{\rho\varphi} \equiv n^a W^a_{\rho\varphi} + g^2\psi_{\rho\varphi} = (\mathcal{W}_\varphi)', \tag{F27}$$

which confirms the identity in (2.34). This allows us to compute the fluxes. Using the boundary conditions (F22), the flux of the U(1) hyperfield is

$$\Psi_B = 2\pi\int_0^\infty B_{\rho\varphi}d\rho = -2\pi\int_0^\infty v'(\rho)d\rho = 2\pi(2k-m-c). \tag{F28}$$

Defining

$$\begin{aligned} \Psi_{\mathcal{W}} &= 2\pi\int_0^\infty \mathcal{W}_{\rho\varphi}d\rho = -2\pi\int_0^\infty (n^1 v_1 + n^3 v_3)'d\rho = 2\pi(c-m), \\ \Psi_W &= 2\pi\int_0^\infty n^a {\rm W}^a_{\rho\varphi}d\rho = -2\pi\int_0^\infty (n^1 v_1' + n^3 v_3')d\rho, \end{aligned} \tag{F29}$$

the 't Hooft fluxes are totally determined by the boundary conditions for the fields:

$$\begin{aligned} \Psi_F &= \frac{g}{g'}\Psi_B - \frac{g'}{g}\Psi_{\mathcal{W}} = \frac{2\pi}{e}(m - c + 2(k-m)g^2), \\ \Psi_Z &= \Psi_B + \Psi_{\mathcal{W}} = 4\pi(k-m). \end{aligned} \tag{F30}$$

The Nambu fluxes are

$$\Psi_{\mathcal{F}} = \frac{g}{g'}\Psi_B - \frac{g'}{g}\Psi_W, \qquad \Psi_{\mathcal{Z}} = \Psi_B + \Psi_W. \tag{F31}$$

3. Chiral strings versus Nambu strings

The results mentioned above are not new and can be found in [94], but now we can add something else. Let us consider chiral solutions—the dressed strings in the limit where they approach Z strings. This means that γ and v_1, f_1 are small, while v, v_3, f_2 are close to the Z string values, so that one has almost everywhere $n^3 \approx -1$ and $n^1 \approx 0$. As γ decreases, the configurations approach Z strings pointwise. However, at $\rho = 0$ one always has $n^3 = +1$; hence, the vector n^a always flips its sign close to the origin. Therefore, the topology is not the same as for the Z strings. In the limit where $\gamma \to 0$, one has

$$c \to 2kg^2 - m,$$
$$\Psi_W \to 2\pi \int_0^\infty v_3' d\rho = 2\pi(c+m) = 4\pi k g^2. \quad \text{(F32)}$$

Therefore, the condensate in the vortex core does not vanish in the limit

$$2\pi g^2 \int_0^\infty \psi_{\rho\varphi} d\rho = \Psi_{\mathcal{W}} - \Psi_W = -4\pi m, \quad \text{(F33)}$$

and the 't Hooft fluxes (F30) reduce to

$$\Psi_F = 4\pi \frac{g'^2}{e} \times m, \qquad \Psi_Z = 4\pi(k-m), \quad \text{(F34)}$$

while the Nambu fluxes (F31) become

$$\Psi_{\mathcal{F}} = 0, \qquad \Psi_{\mathcal{Z}} = 4\pi k. \quad \text{(F35)}$$

Notice that the magnetic flux Ψ_F is proportional to $4\pi g'^2/e$, which matches the flux produced by the Nambu monopole [61]. This monopole is attached to a string and corresponds to the point where the string terminates, allowing the fields that were confined within the string to spread outward in all directions (see Ref. [90,100,101]).

Assuming that a chiral string terminates at some point, the magnetic field previously confined within the string will escape to the exterior, carrying with it the same total flux Ψ_F. This follows from the fact that the 't Hooft fluxes Ψ_F and Ψ_Z are conserved, and therefore must be identical both inside and outside the string. Consequently, the endpoint of a chiral string should manifest as a Nambu monopole.

On the other hand, the Nambu fluxes $\Psi_{\mathcal{F}}$ and $\Psi_{\mathcal{Z}}$ are not conserved, and the fluxes inside the string differ from those produced by the monopole outside the string. Remarkably, the Nambu fluxes in (F35) match exactly (for $k = 1$) those obtained in Nambu's original analysis [61] for a string terminating on a monopole.

This suggests that the Nambu string—the electroweak string attached to the Nambu monopole—can be interpreted as a chiral string, since the Nambu fluxes coincide in both cases and the chiral string carries the same magnetic flux Ψ_F as the Nambu monopole. To the best of our knowledge, the Nambu string has never been explicitly described in the literature, and it is typically assumed to be identical to the Z string [100], as the Nambu fluxes also match in that case. However, because the Nambu string must carry the same magnetic flux Ψ_F as the monopole, it cannot be a Z string, although it may closely resemble one in the sense described above.

Nevertheless, one should note that, unlike Z strings, chiral solutions exist only for special parameter values corresponding to the chiral curves shown in Fig. 4 in [94]. For the physical values of $\theta_{\rm W}, \beta$, chiral solutions do not exist. However, there are dressed solutions that also carry a magnetic flux, although its value is not exactly a multiple of $4\pi g'^2/e$. For example, choosing the physical parameters $\sin^2\theta_{\rm W} = 0.223$, $\beta = 1.88$, the solution with $k = 4$, $m = 7$ shown in Fig. 26 has $\gamma = 0.177$ and the flux $\Psi_F \approx 0.9 \times 4\pi m \times g'^2/e$. By contrast, a solution with the same (k, m) and with $\gamma = 0.01$, which is quite close to the chiral limit, is found only for $\sin^2\theta_{\rm W} = 0.199$. This illustrates that chiral solutions are not generic.

It is therefore logically possible that Nambu monopoles arising in realistic scenarios, such as those produced via the Kibble mechanism [89,90], are connected to dressed strings, in which case their magnetic flux is not exactly equal to $4\pi g'^2/e$, but only approximately so. At the same time, the magnetic flux associated with chiral strings—being an exact multiple of $4\pi g'^2/e$—appears to emerge generically in various contexts with physical parameter values. For instance, such fluxes are present in the horizon vortices described by (10.17), as well as in the vortex connecting a monopole-antimonopole pair with charges $\pm g'^2/e$ in the flat-space sphaleron configuration [59]. These examples involve vortices of finite length that are not necessarily straight. This suggests that while chiral strings are exceptional and nongeneric in the form of straight, infinite configurations, finite segments of such strings may well exist under realistic physical conditions.

In summary, the electroweak string described by Nambu, often identified with the Z string, appears to be more accurately interpreted as a chiral string—a configuration that closely resembles a Z string but includes a condensate in its core. Nevertheless, a more detailed analysis of this identification remains necessary.

[1] R. Ruffini and J. Wheeler, Introducing the black hole, Phys. Today **24**, No. 1, 30 (1971).
[2] W. Israel, Event horizons in static vacuum space-times, Phys. Rev. **164**, 1776 (1967).
[3] D. C. Robinson, Uniqueness of the Kerr black hole, Phys. Rev. Lett. **34**, 905 (1975).
[4] P. O. Mazur, Proof of uniqueness of the Kerr-Newman black hole solution, J. Phys. A **15**, 3173 (1982).
[5] M. Heusler, *Black Hole Uniqueness Theorems* (Cambridge University Press, Cambridge, England, 1996).
[6] J. E. Chase, Event horizons in static scalar-vacuum space-times, Commun. Math. Phys. **19**, 276 (1970).
[7] J. D. Bekenstein, Nonexistence of baryon number for static black holes, Phys. Rev. D **5**, 1239 (1972).
[8] J. D. Bekenstein, Transcendence of the law of baryon-number conservation in black hole physics, Phys. Rev. Lett. **28**, 452 (1972).
[9] J. D. Bekenstein, Novel "no-scalar-hair" theorem for black holes, Phys. Rev. D **51**, R6608 (1995).
[10] A. E. Mayo and J. D. Bekenstein, No hair for spherical black holes: Charged and nonminimally coupled scalar field with self-interaction, Phys. Rev. D **54**, 5059 (1996).
[11] J. D. Bekenstein, Black hole hair: 25—years after, in *Proceedings of the 2nd International Sakharov Conference on Physics* (1996), pp. 216–219, arXiv:gr-qc/9605059.
[12] A. Saa, New no scalar hair theorem for black holes, J. Math. Phys. (N.Y.) **37**, 2346 (1996).
[13] C. A. R. Herdeiro and E. Radu, Asymptotically flat black holes with scalar hair: A review, Int. J. Mod. Phys. D **24**, 1542014 (2015).
[14] M. S. Volkov and D. V. Galtsov, NonAbelian Einstein Yang-Mills black holes, Pis'ma Zh. Eksp. Teor. Fiz. **50**, 312 (1989) [JETP Lett. **50**, 346 (1989), http://jetpletters.ru/ps/1130/article_17118.shtml].
[15] M. S. Volkov, Hairy black holes in the XX-th and XXI-st centuries, arXiv:1601.08230.
[16] H. P. Kuenzle and A. K. M. Masood-ul Alam, Spherically symmetric static SU(2) Einstein Yang-Mills fields, J. Math. Phys. (N.Y.) **31**, 928 (1990).
[17] P. Bizon, Colored black holes, Phys. Rev. Lett. **64**, 2844 (1990).
[18] S. Droz, M. Heusler, and N. Straumann, New black hole solutions with hair, Phys. Lett. B **268**, 371 (1991).
[19] P. Bizon and T. Chmaj, Gravitating skyrmions, Phys. Lett. B **297**, 55 (1992).
[20] P. Breitenlohner, P. Forgács, and D. Maison, Gravitating monopole solutions, Nucl. Phys. **B383**, 357 (1992).
[21] B. R. Greene, S. D. Mathur, and C. M. O'Neill, Eluding the no hair conjecture: Black holes in spontaneously broken gauge theories, Phys. Rev. D **47**, 2242 (1993).
[22] G. Lavrelashvili and D. Maison, Regular and black hole solutions of Einstein-Yang-Mills dilaton theory, Nucl. Phys. **B410**, 407 (1993).
[23] S. Mignemi and N. R. Stewart, Charged black holes in effective string theory, Phys. Rev. D **47**, 5259 (1993).
[24] P. Kanti, N. E. Mavromatos, J. Rizos, K. Tamvakis, and E. Winstanley, Dilatonic black holes in higher curvature string gravity, Phys. Rev. D **54**, 5049 (1996).
[25] T. Torii, H. Yajima, and K.-i. Maeda, Dilatonic black holes with Gauss-Bonnet term, Phys. Rev. D **55**, 739 (1997).
[26] B. Kleihaus and J. Kunz, Static black-hole solutions with axial symmetry, Phys. Rev. Lett. **79**, 1595 (1997).
[27] B. Kleihaus and J. Kunz, Rotating hairy black holes, Phys. Rev. Lett. **86**, 3704 (2001).
[28] M. S. Volkov and D. V. Gal'tsov, Gravitating nonAbelian solitons and black holes with Yang-Mills fields, Phys. Rep. **319**, 1 (1999).
[29] U. Nucamendi and M. Salgado, Scalar hairy black holes and solitons in asymptotically flat space-times, Phys. Rev. D **68**, 044026 (2003).
[30] K. G. Zloshchastiev, On co-existence of black holes and scalar field, Phys. Rev. Lett. **94**, 121101 (2005).
[31] A. Anabalon, D. Astefanesei, and R. Mann, Exact asymptotically flat charged hairy black holes with a dilaton potential, J. High Energy Phys. 10 (2013) 184.
[32] M. Rinaldi, Black holes with non-minimal derivative coupling, Phys. Rev. D **86**, 084048 (2012).
[33] T. P. Sotiriou and S.-Y. Zhou, Black hole hair in generalized scalar-tensor gravity: An explicit example, Phys. Rev. D **90**, 124063 (2014).
[34] E. Babichev and C. Charmousis, Dressing a black hole with a time-dependent Galileon, J. High Energy Phys. 08 (2014) 106.
[35] T. Kobayashi and N. Tanahashi, Exact black hole solutions in shift symmetric scalar–tensor theories, Prog. Theor. Exp. Phys. **2014**, 073E02 (2014).
[36] C. A. R. Herdeiro and E. Radu, Kerr black holes with scalar hair, Phys. Rev. Lett. **112**, 221101 (2014).
[37] C. Herdeiro, E. Radu, and H. Rúnarsson, Kerr black holes with Proca hair, Classical Quantum Gravity **33**, 154001 (2016).
[38] W. E. East and F. Pretorius, Superradiant instability and backreaction of massive vector fields around Kerr black holes, Phys. Rev. Lett. **119**, 041101 (2017).
[39] D. D. Doneva, F. M. Ramazanoğlu, H. O. Silva, T. P. Sotiriou, and S. S. Yazadjiev, Spontaneous scalarization, Rev. Mod. Phys. **96**, 015004 (2024).
[40] R. Brito, V. Cardoso, and P. Pani, Black holes with massive graviton hair, Phys. Rev. D **88**, 064006 (2013).
[41] R. Gervalle and M. S. Volkov, Asymptotically flat hairy black holes in massive bigravity, Phys. Rev. D **102**, 124040 (2020).
[42] E. Alonso-Monsalve and D. I. Kaiser, Primordial black holes with QCD color charge, Phys. Rev. Lett. **132**, 231402 (2024).
[43] Y. Bai and M. Korwar, Hairy magnetic and dyonic black holes in the standard model, J. High Energy Phys. 04 (2021) 119.
[44] K.-M. Lee and E. J. Weinberg, Nontopological magnetic monopoles and new magnetically charged black holes, Phys. Rev. Lett. **73**, 1203 (1994).
[45] S. A. Ridgway and E. J. Weinberg, Static black hole solutions without rotational symmetry, Phys. Rev. D **52**, 3440 (1995).
[46] J. Maldacena, Comments on magnetic black holes, J. High Energy Phys. 04 (2021) 079.
[47] J. Ambjorn and P. Olesen, On electroweak magnetism, Nucl. Phys. **B315**, 606 (1989).

[48] J. Ambjorn and P. Olesen, Electroweak magnetism: Theory and application, Int. J. Mod. Phys. A **05**, 4525 (1990).
[49] M. N. Chernodub, J. Van Doorsselaere, and H. Verschelde, Magnetic-field-induced superconductivity and superfluidity of W and Z bosons: In tandem transport and kaleidoscopic vortex states, Phys. Rev. D **88**, 065006 (2013).
[50] M. N. Chernodub, V. A. Goy, and A. V. Molochkov, Phase structure of electroweak vacuum in a strong magnetic field: The lattice results, Phys. Rev. Lett. **130**, 111802 (2023).
[51] Y. Bai, J. Berger, M. Korwar, and N. Orlofsky, Phenomenology of magnetic black holes with electroweak-symmetric coronas, J. High Energy Phys. 10 (2020) 210.
[52] Y. Bai, S. Lu, and N. Orlofsky, Searching for magnetic monopoles with the Earth's magnetic field, Phys. Rev. Lett. **127**, 101801 (2021).
[53] D. Ghosh, A. Thalapillil, and F. Ullah, Astrophysical hints for magnetic black holes, Phys. Rev. D **103**, 023006 (2021).
[54] J. Estes, M. Kavic, S. L. Liebling, M. Lippert, and J. H. Simonetti, Stability and observability of magnetic primordial black hole-neutron star collisions, J. Cosmol. Astropart. Phys. 06 (2023) 017.
[55] M. D. Diamond and D. E. Kaplan, Constraints on relic magnetic black holes, J. High Energy Phys. 03 (2022) 157.
[56] Y. M. Cho, S.-W. Kim, and S. H. Oh, Electroweak primordial magnetic blackhole: Cosmic production and physical implication, arXiv:2408.05531.
[57] R. Gervalle and M. S. Volkov, Black holes with electroweak hair, Phys. Rev. Lett. **133**, 171402 (2024).
[58] R. Gervalle and M. S. Volkov, Electroweak monopoles and their stability, Nucl. Phys. **B984**, 115937 (2022).
[59] R. Gervalle and M. S. Volkov, Electroweak multi-monopoles, Nucl. Phys. **B987**, 116112 (2023).
[60] E. Tiesinga, P. J. Mohr, D. B. Newell, and B. N. Taylor, CODATA recommended values of the fundamental physical constants: 2018*, Rev. Mod. Phys. **93**, 025010 (2021).
[61] Y. Nambu, String-like configurations in the Weinberg-Salam theory, Nucl. Phys. **B130**, 505 (1977).
[62] G. 't Hooft, Magnetic monopoles in unified gauge theories, Nucl. Phys. **B79**, 276 (1974).
[63] P. A. M. Dirac, Quantised singularities in the electromagnetic field, Proc. R. Soc. A **133**, 60 (1931).
[64] B. Bertotti, Uniform electromagnetic field in the theory of general relativity, Phys. Rev. **116**, 1331 (1959).
[65] I. Robinson, A solution of the Maxwell-Einstein equations, Bull. Acad. Pol. Sci., Ser. Sci., Math., Astron. Phys. **7**, 351 (1959).
[66] S. Hod, Electroweak clouds supported by magnetically charged black holes: Analytic treatment along the existence line, Phys. Rev. D **110**, 104045 (2024).
[67] W. Press, S. Teukolsky, W. Vetterling, and B. Flannery, *Numerical Recipes 3rd Edition: The Art of Scientific Computing*, 3rd ed. (Cambridge University Press, New York, USA, 2007).
[68] J. Ambjorn and P. Olesen, A condensate solution of the electroweak theory which interpolates between the broken and the symmetric phase, Nucl. Phys. **B330**, 193 (1990).
[69] N. Arkani-Hamed, L. Motl, A. Nicolis, and C. Vafa, The string landscape, black holes and gravity as the weakest force, J. High Energy Phys. 06 (2007) 060.
[70] Y. M. Cho and D. Maison, Monopoles in Weinberg-Salam model, Phys. Lett. B **391**, 360 (1997).
[71] *Relativity: The General theory*, edited by J. L. Synge (North-Holland Publishing Company, Amsterdam, 1960).
[72] A. Komar, Covariant conservation laws in general relativity, Phys. Rev. **113**, 934 (1959).
[73] C. Rebbi and P. Rossi, Multi—monopole solutions in the Prasad-Sommerfield limit, Phys. Rev. D **22**, 2010 (1980).
[74] F. Hecht, New development in FreeFem++, J. Numer. Math. **20**, 251 (2012).
[75] S. Deser, Absence of static solutions in source-free Yang-Mills theory, Phys. Lett. **64B**, 463 (1976).
[76] G. H. Derrick, Comments on nonlinear wave equations as models for elementary particles, J. Math. Phys. (N.Y.) **5**, 1252 (1964).
[77] C. A. R. Herdeiro, J. a. M. S. Oliveira, A. M. Pombo, and E. Radu, Deconstructing scaling virial identities in general relativity: Spherical symmetry and beyond, Phys. Rev. D **106**, 024054 (2022).
[78] R. P. Geroch, Multipole moments. II. Curved space, J. Math. Phys. (N.Y.) **11**, 2580 (1970).
[79] R. Hansen, Multipole moments of stationary spacetimes, J. Math. Phys. (N.Y.) **15**, 46 (1974).
[80] G. Fodor, C. Hoenselaers, and Z. Perjes, Multipole moments of axisymmetric systems in relativity, J. Math. Phys. (N.Y.) **30**, 2252 (1989).
[81] G. Fodor, E. d. S. C. Filho, and B. Hartmann, Calculation of multipole moments of axistationary electrovacuum spacetimes, Phys. Rev. D **104**, 064012 (2021).
[82] F. J. Ernst, New formulation of the axially symmetric gravitational potential, Phys. Rev. **167**, 1175 (1968).
[83] F. J. Ernst, New formulation of the axially symmetric gravitational field problem. II, Phys. Rev. **168**, 1415 (1968).
[84] P. Olesen, Vacuum structure of the electroweak theory in high magnetic fields, Phys. Lett. B **268**, 389 (1991).
[85] J. Van Doorsselaere, Properties of symmetry restoration in the electroweak vacuum in very high magnetic fields, Phys. Rev. D **88**, 025013 (2013).
[86] F. L. Bezrukov and M. Shaposhnikov, The standard model Higgs boson as the inflaton, Phys. Lett. B **659**, 703 (2008).
[87] B. Kleihaus and J. Kunz, Monopole—anti-monopole solutions of Einstein-Yang-Mills-Higgs theory, Phys. Rev. Lett. **85**, 2430 (2000).
[88] C. A. R. Herdeiro and E. Radu, Two Schwarzschild-like black holes balanced by their scalar hair, Phys. Rev. D **107**, 064044 (2023).
[89] J. Urrestilla, A. Achucarro, J. Borrill, and A. R. Liddle, The evolution and persistence of dumbbells in electroweak theory, J. High Energy Phys. 08 (2002) 033.
[90] T. Patel and T. Vachaspati, Kibble mechanism for electroweak magnetic monopoles and magnetic fields, J. High Energy Phys. 01 (2022) 059.
[91] A. A. Abrikosov, On the magnetic properties of superconductors of the second group, Sov. Phys. JETP **5**, 1174 (1957), http://www.w2agz.com/Library/Classic%20Papers%20in%20Superconductivity/Abrikosov,%20Type%20II%20Superconductivity,%20Sov-Phys%20JETP%205,%201174%20(1957).pdf.

[92] V. L. Ginzburg and L. D. Landau, On the theory of superconductivity, Zh. Eksp. Teor. Fiz. **20**, 1064 (1950).
[93] H. B. Nielsen and P. Olesen, Vortex line models for dual strings, Nucl. Phys. **B61**, 45 (1973).
[94] J. Garaud and M. S. Volkov, Superconducting non-Abelian vortices in Weinberg-Salam theory—electroweak thunderbolts, Nucl. Phys. **B826**, 174 (2010).
[95] T. Vachaspati, Vortex solutions in the Weinberg-Salam model, Phys. Rev. Lett. **68**, 1977 (1992).
[96] T. Vachaspati and M. Barriola, A new class of defects, Phys. Rev. Lett. **69**, 1867 (1992).
[97] W. B. Perkins, W condensation in electroweak strings, Phys. Rev. D **47**, R5224 (1993).
[98] P. Olesen, A W dressed electroweak string, arXiv:hep-ph/9310275.
[99] A. Achucarro, R. Gregory, J. A. Harvey, and K. Kuijken, Cinderella strings, Phys. Rev. Lett. **72**, 3646 (1994).
[100] T. Patel and T. Vachaspati, Structure of electroweak dumbbells, Phys. Rev. D **107**, 093010 (2023).
[101] V. Domcke, Y. Ema, and T. Patel, Spontaneous magnetogenesis at the electroweak phase transition, arXiv:2505.10637.